Thermoelectric performance of layered cobaltate epitaxial films deposited by pulsed laser evaporation

Arindom Chatterjee

UNIVERSITAT AUTÓNOMA DE BARCELONA

POSTGRADUATE SCHOOL

PHYSICS DEPARTMENT

Ph. D. THESIS

Thermoelectric performance of layered cobaltate epitaxial films deposited by pulsed laser evaporation

Thesis submitted by

Arindom Chatterjee

to apply for the degree of Doctor of Philosophy at the Universitat Autonóma de Barcelona in the MATERIALS SCIENCE PROGRAMME

Thesis advisors:

Prof. José Santiso López, CSIC

&

Prof. Clivia M Sotomayor Torres, ICREA

Thesis tutor:

Prof. Gemma Garcia (Department of Physics, UAB)

Catalan Institute of Nanoscience and Nanotechnology (ICN2)

Bellaterra-08193, Barcelona, Spain

May, 2018

To my family

&

In memory of my uncle

Late Sunil Kumar Chatterjee

Acknowledgements

First and foremost, I would like to thank my thesis directors Prof. Jose Santiso and Prof. Clivia M Sotomayor. None of the work would have been taken place without their freely given support, guidance and, confidence in me. I would also like to acknowledge the Spanish Government and ICN2 for the Severo Ochoa (SO) grant which covered my salary, part of the UAB tuition fees, expenses to attend conferences and also to pursue research to other laboratories. I thank my tutor Prof. Gemma Garcia from UAB.

A very special thanks goes to my colleague Dr. José Manuel Caicedo Roque for being a good friend from the first day of my work at ICN2 and for an introducing me to the PLD technique. I felt at home working with him throughout my stay. I also thank my colleagues Anna, Núria, Laura, James and Roberto, for their support and friendship and also my colleagues in the P2N group; Emigdio, Marianna, Sweta, Daniel, Guillermo, Miguel, Martin, Jeremie.

I cannot thank Prof. Francisco Rivadulla enough for his help and guidance to write this thesis during my research stay at CiQUS, University of Santiago de Compostela, Spain. Fran is perhaps one of the best teachers I have ever met in my life and thanks again to Santi for introducing me to Fran. I also thank my colleagues at CiQUS: Victor, Lucia, David, Carlos, Manuel, Elbordallo and, Elias for their support and fruitful discussions.

I sincerely thank Dr. Belén Ballesteros Pérez, Francisco Javier Belarre and Marcos Rosado Iglesias for their help during transmission electron microscopy measurements.

I would also like to thank Pablo and Dr. Jessica Padilla for their help with the X-ray diffraction measurement. Jessica was always willing to help with the XRD measurements for my samples within her busy schedule and she also taught me Rietveld refinements. I would also like to thank Dr. Geolloyme for performing XPS measurements of my samples and Prof. Gustau Catalan for his support.

Thanks too to all of my friends at ICN2: Igor, Alba, Alóis, Zewdu, Rocio, Bhawna, Miguel and Carlos for being with me in my bad and good moments. Igor is a very good friend of mine and we have spent a lot of time roaming around Barcelona and having nice food in many restaurants.

I thank Prof. Kanishka Biswas, JNCASR, India, for introducing solid state chemistry to me and for his constant support since we met in 2013. I also thank my lab mates at JNCASR: Satya da, Manoj, Chitaiah, Ananya, Subhajit and Suresh.

I believe that it would have been impossible to complete my work without the help of colleagues from administration department and IT department of ICN2. I sincerely thank all of them for their kind support. I also thank our English teacher, Andrew Hudson, at ICN2 for correcting my thesis.

I sincerely thank Prof. Alberto Pomar and Dr. Bernat Bazoo at ICMAB, Spain, for their help with the Hall measurements.

I thank my childhood friends: Sanjib, Prasenjit (Posen), Prasenjit Das, Biswajit (Prolladh), Ananta, Balak and Brojo; High School friends: Biplob (Lob), Bikram (Kush), Ananta Birbansha, Ashis, Manab, Mafijul, Asmot, Krishnendu (Chand), Tuhin, Rajib, Pritam and, Animesh (Rana); College friends: Sumanta, Prasenjit, Sukdeb, Sourov (Kara), Sanjoy, Saheb Sushovan, Hasan, Tuhin and Subhamay; University friends: Sandipan, Chinmay, Subrata (Ghau), Subhankar, Provash, Sukanta, Subhrojyoti, Nilanja da, Atanu da, Koushik, Souvik, Pinku and, Siraj; JNCASR friends: Aloke da, Sandip da, Swaity di, Abhijit da and, Swathi. Special thanks go to Sandipan (and Sourov) for inspiring me to pursue a PhD and also for being with me since we met in 2010. I also thank Nemai Banerjee (mama) and his wife (mamima) for their kind help during the higher secondary examination in Suri in 2007.

I sincerely thank all of my teachers from childhood to University: All past and present teachers of Nabipur Primary School, Srimanta da, Ramkrishka Mandal, Tapas Kumar Das, all past and present teachers of Bhalkundi High School (special thanks to Chanachal Chakrabarty, Satyen Biswas, Binoy Kumar Mandal, Purnendu Mandal and Rabindranath Sen) and Krishnath College. I express my gratitude to my teachers Dr. Debaprasad Panda (Jiagang Sripath Singh College) and Dr. Kamakshya Guha (Krishnath College, Berhampore) for their support throughout my life.

Finally I would like to thank my family. No matter whatever happens they are always with me. The hard work and sacrifices of my parents (Kamana Chatterjee & Kshetranath Chatterjee), my sister (Tanusree Chakraborty), my aunt (Basana Chatterjee), my uncle (Late Sunil Kumar Chatterjee) and my cousin brother (dada, Gobinda Chatterjee) and sister (didi, Champa Bhattacharya) who encouraged me to pursue my higher education at a very difficult time. My uncle would have been so happy for this day if he were alive. All my hard work is only for you. I will always regret not having devoted enough time to them. Thanks for everything you have given me throughout my life.

Arindom Chatterjee

Bellaterra, 30 de abril de 2018

El Dr. José Santiso López, científico titular del CSIC, y la Prof. Clivia Sotomayor Torres, investigador ICREA, ambos en el **Institut Català de Nanociència i Nanotecnología (ICN2)**, en calidad de directores de tesis y la Dra. Gemma Garcia Alonso, profesora titular de la **Universidad Autónoma de Barcelona**, en calidad de tutora de la tesis,

CERTIFICAN:

Que **Arindom Chatterjee**, licenciado en Física, ha realizado bajo su dirección el trabajo que lleva por título: "***Thermoelectric Performance of layered cobaltate epitaxial films deposited by pulsed laser evaporation***". Dicho trabajo ha sido desarrollado dentro del programa de doctorado de Ciencia de Materiales y constituye su memoria de tesis doctoral, para optar al título de Doctor por la Universidad Autónoma de Barcelona.

Dr. José Santiso López

Prof. Clivia Sotomayor Torres

Dra. Gemma Garcia Alonso

Declaration

I hereby declare that the work in this thesis entitled "**Thermoelectric performance of layered cobaltates epitaxial films deposited by pulsed laser evaporation**", is the result of research carried out by me at the '**Catalan Institute of Nanoscience and Nanotechnology (ICN2)**' under the supervision of Prof. Jose Santiso (thesis director), Prof. Clivia M Sotomayor Torres (thesis director) and, Prof Gemma Garcia (tutor).

In keeping with the general practices of reporting scientific observation, due acknowledgments have been made whenever the work described is based on the findings of other investigators. Any omission which might have occurred by oversight or error of judgment is regretted.

Arindom Chatterjee

02nd May, 2018

Abstract

Thermoelectric Seebeck effect is a very important phenomenon of a charge conductor as it provides fundamental information such as the electronic band structure near Fermi energy. Thermoelectric devices are very important from a technological point of view because of its ability to convert electricity from a temperature gradient. However, the low efficiency; of the thermoelectric materials, limits their use for practical applications. Therefore, it is important to design thermoelectric materials that are good electrical conductor, poor thermal conductor and at the same time have large S. Thus, design of efficient thermoelectric materials is a scientific and also an engineering challenge.

Among the different thermoelectric materials explored in the literature, layered compounds have shown very important characteristics most of them related to their anisotropic properties. In that sense, the growth of epitaxial (or highly oriented) thin films allows exploring the physical properties in a particular crystallographic direction and, therefore is ideal for exploring the possible anisotropy. At the same time, it allows to engineer the electronic, thermoelectric as well as the thermal transport properties by playing with epitaxial strain, defect chemistry and interface between multilayers.

This thesis reports the investigation of thermoelectric properties of epitaxial and highly oriented layered cobaltates films includes a detailed description of the different possible methods to tune the oxygen stoichiometry of thin films. The thesis is divided into several chapters. A brief introduction of the thermoelectric phenomena is provided in chapter 1. Then, the description is focused on the TE properties of layered cobaltates. A short literature review is presented where attention was paid to the status of scientific problems and experimental results. Chapter 2 shows the techniques used to perform the experiments. Thermoelectric properties of layered cobaltates films are presented from chapter 3 to 5 in order to address specific questions in each chapter. Chapter 6 shows the control over oxygen stoichiometry of cobaltate thin film by means of solid state electrochemical approach. Finally, a summary of the conclusions and perspectives are discussed in chapter 7.

The exploration of the thermoelectric properties of layered cobaltates thin films led to the conclusion that, contrary to the current belief, spin-orbit degeneracy does not contribute to the high-temperature limit of the Seebeck coefficient, and only the statistical distribution of electrons in the available states is relevant for determining such limit. Consequently, a modification of the Heike's formula, containing the information of polaron size, is proposed.

Symbols used

δ =Oxygen content
φ = Electrochemical potential
R = Ideal gas constant
F = Faraday constant
p^{O_2} = Oxygen partial pressure
$p_{O_2}^{eff}$ = Effective oxygen partial pressure
$V_{\ddot{O}}$ = Oxygen vacancies
O^x = Oxygen in lattice
I = Current
t = Time
Q_e = Number of transported charge
$V_{unit\ cell}$ = Volume of unit cell
$V_{thin\ film}$ = Volume of thin film
Q_x =*X*-component of the reciprocal space vector
Q_y =Y-component of the reciprocal space vector
ρ = Resistivity
S = Seebeck coefficient or thermopower
κ_B = Boltzmann constant
e = Elementary charge of electron
x = Number of electrons per unit cell
β = Spin-orbit degeneracy
g = Degeneracy
K = Equilibrium constant
n = Charge carrier density
Q = Size of polarons
T = Temperature
μ = Mobility of electron
κ = Thermal conductivity
κ_L = Lattice thermal conductivity
κ_e = Electronic thermal conductivity
L = Lorentz number
l = Mean free path of phonons
η = Carnot efficiency
z = Thermoelectric figure of merit
E_F = Fermi energy
C_v = Specific heat capacity
μ_e = Chemical potential
S_c = Configurational entropy
λ = Wavelength
R_H = Hall coefficient

Acronyms used

ARPES= Angle resolved photoelectron spectroscopy
BSCO = $Bi_2Sr_2Co_2O_y$ = $[Bi_2Sr_2O_{4-\delta}]^{RS}[CoO_2]_q$
BE = Binding energy
CGO = $Ce_{0.2}Gd_{0.8}O_2$
CCO = $Ca_3Co_4O_9$ = $[Ca_2CoO_{3-\delta}]^{RS}[CoO_2]_q$
DOS = Density of states
DMFT = Dynamic mean-fiend theory
e.m.f. = Electromotive force
GBCO = $GdBaCo_2O_{5.5}$
HBCO = $HoBaCo_2O_{5.5}$
HS = High spin
IS = Intermediate spin
LAO = $LaAlO_3$
LSAT = $(LaAlO_3)_{0.3}(Sr_2TaAlO_6)_{0.7}$
LS = Low spin
MIT = Metal-insulator transition
NMR = Nuclear magnetic resonance
NCO = Na_xCoO_2
Oct = Octahedra
PLD = Pulsed laser deposition
P_y = Pyramid
RSM = Reciprocal space map
STEM = Scanning TEM
STO = $SrTiO_3$
SAED = Selected area electron diffraction
TEM = Transmission electron microscopy
VB-XPS = Valence band-XPS
VRH = Variable range hopping
XRD = X-ray diffraction
XRR = X-ray reflectivity
XPS = X-ray photoelectron spectroscopy
YSZ = Y_2O_3 substituted Zr_2O_3

TABLE OF CONTENT

TABLE OF CONTENT

TABLE OF CONTENT

Chapter 1: Basics of thermoelectricity and oxide thermoelectrics

The purpose of this chapter is to provide a general description of the thermoelectric effects and related devices. This chapter describes how efficiency is related to materials properties (such as the transport coefficients and figure of merit, zT). Then, the discussion is focused on the thermoelectric properties of layered cobaltates. Contrary to the approaches related to band structure engineering, thermopower of the layered misfit (and other) cobaltates can be optimized by the entropy flow given by Heike's limit. The case off Na_xCoO_2 and misfit cobaltates is discussed in detail.

1.1 Introduction

One of the biggest challenges faced by human being in this century is to solve the energy crisis. The emerging global need for energy production, storage, and utilization has intensified interest in more efficient, cost-effective, long lasting and pollution-free means of power conversion. Driven by the demand for clean and sustainable energy sources, thermoelectricity has become an important part of the research portfolio that is seeking to identify efficient materials for power generation and thermoelectric cooling applications. The major disadvantage of existing thermal power plants and combustion processes is that almost ~65 % of the utilized energy is being lost as waste heat. Thermoelectric materials are solid-state energy converters without any moving parts which can directly and reversibly convert heat into electrical energy.[1], [2] It is generally considered that if a thermoelectric device can convert ~30-40% of total waste heat into electricity, then it will have a considerable impact on overall energy conversion and management. More recently, research on the utilization of the infrared part of the solar radiation in solar thermoelectrics gaining attention.[3] Novel applications of thermoelectrics include bio thermal batteries and power provision for deep space probes via radioisotope thermoelectric generators.[4]

1.2 Thermoelectricity

In 1822, it was demonstrated that when two dissimilar metallic wires (say copper and iron) were joined at the end and two junctions were kept at different temperatures, an electromotive force (e.m.f.) was produced.[5] This phenomenon is known as the Seebeck effect (Figure 1.1). The magnitude and direction of thermoelectric e.m.f. depends on the nature of the materials forming the thermocouple and temperature difference between two junctions.[6] Usually, the thermo e.m.f is very small. For a Sb-Bi thermocouple, it is 100μV/K. The Seebeck effect is reversible i.e., if hot and cold junctions are interchanged, the direction of the thermo e.m.f. is reversed. In contrast, in thermoelectric materials, when a small amount of current is applied through a junction between two dissimilar metals, one junction gets cold and the other becomes hot. This effect is called the Peltier effect, which is the inverse effect of Seebeck effect.

Thermoelectric properties of different pairs of metals were studied and arranged them in a certain sequence called thermoelectric series or Seebeck series, as follows:

Bi, Ni, Co, Pd, Pt, Cu, Mn, Hg, Pb, Sn, Au, Ag, Zn, Cd, Fe, Sb, Te

Important features of the series are the direction of current at the hot junction from the metal occurring earlier in the series to one occurring later in the series. The magnitude of the thermo e.m.f. is large appearing further apart in the series.

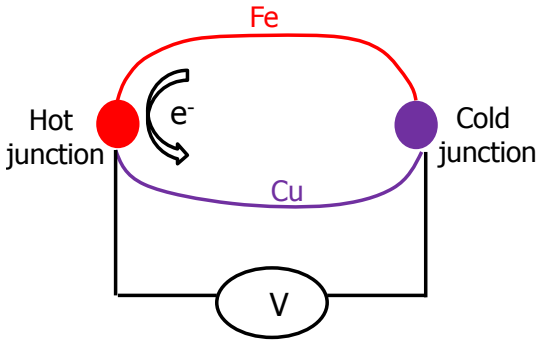

Figure 1.1 Schematic illustration of the Seebeck effect at the junctions of two dissimilar metals copper and iron.

1.3 Origin of thermo e.m.f.

If two dissimilar metals are in contact, free electrons diffuse from one metal having a lower work function to the other having a higher work function. Thus, one metal becomes positively charged while the other becomes negatively charged. This continues until the difference in potential across the boundary surface becomes high enough to establish equilibrium. This potential difference is known as contact e.m.f. Therefore, the thermoelectric series is, in fact, the order according to the corresponding work function of the different metals. The direction and magnitude of the contact e.m.f. depends on the metal used and on the temperature of the junction. For example, when copper is brought into contact with iron, free electrons diffuse from iron to copper, thus making iron positive with respect to copper (Figure 1.1). Hence, the direction of the contact e.m.f at the Fe-Cu junction will be from Cu to Fe. If the junction of the two metals forming the thermocouple kept at the same temperature, two contact e.m.f. is equal and opposite in polarity. Hence, they cancel each other out and no e.m.f. is developed in the thermocouple. It is noteworthy that the contact e.m.f. depends only on the work function of metals.

1.4 Effect of temperature on thermo e.m.f.

The effect of the temperature difference between two junctions is shown in Figure 1.2. Keeping the temperature of the cold junction at 0°C, the temperature of the hot junction gradually increases. The graph of thermo e.m.f. in relation to temperature of the hot junction has a parabolic shape.[6] The main features of the graph are the following:

- When two junctions are at the same temperature, the thermo e.m.f. is zero.
- As the temperature of the hot junction is increased, maintaining the cold junction at 0°C, the thermo e.m.f. increases until it reaches the maximum at temperature T_n. This temperature T_n is called neutral temperature and it depends on the nature of the thermocouple materials. For a particular pair of metals, it is constant. For a Cu-Fe thermocouple, T_n is 270°C.
- As the temperature of the hot junction is increased further beyond the neutral temperature, the thermo e.m.f. decreases and ultimately becomes zero at temperature T_i. This temperature for a particular thermocouple is known as the inversion temperature, since; the thermo e.m.f. changes its polarity with the increase of temperature. This is due to the fact that the electron density and diffusion rates of electrons are reversed. The inversion temperature depends on the temperature of the cold junction and the nature of the metals forming thermocouple.

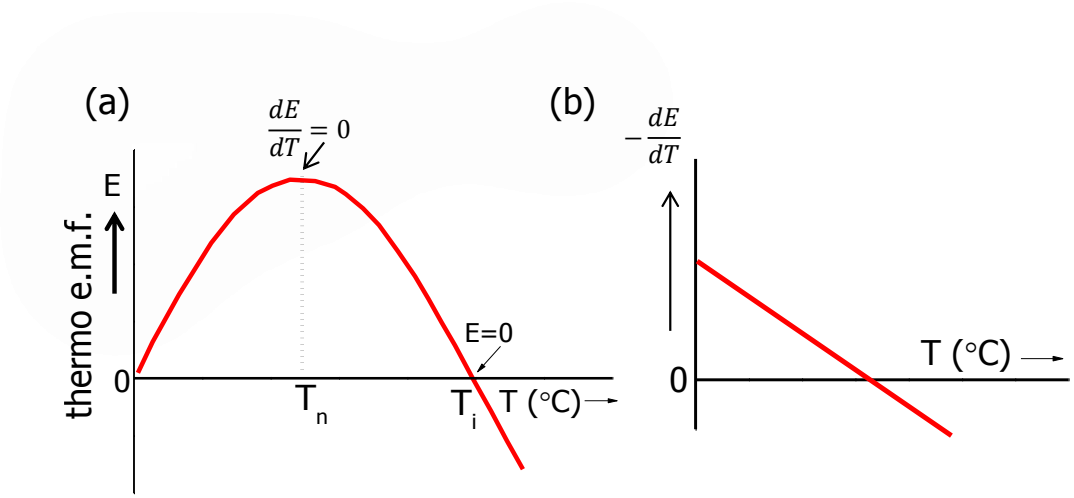

Figure 1.2 Schematic illustration of the effect of temperature on the thermoelectric e.m.f. in a thermocouple junction.

1.5 Thermopower or Seebeck coefficient (S)

The relation between thermo e.m.f. and temperature is shown in the following equation

$$E = \alpha T + \frac{1}{2}\lambda T^2 \qquad (1.1)$$

where, α and λ are constants. The rate of change of thermo e.m.f. with temperature is called the Seebeck coefficient or thermopower denoted as S. So, mathematically it can be defined as

$$S = \frac{dE}{dT} = \frac{d}{dT}\left[\alpha T + \frac{1}{2}\lambda T^2\right] = \alpha + \lambda T$$

Thus, the S varies linearly with temperature. At neutral temperature, thermo e.m.f. is maximum, therefore, $\frac{dE}{dT} = 0 = \alpha + \lambda T$. At this temperature one obtains $T_n = -\alpha/\lambda$. At the inversion temperature, $T = T_i$, one obtains $T_i = -2\alpha/\lambda$. The inversion and the neutral temperatures depend on the type of thermocouple used. A thermocouple is basically a thermoelectric thermometer and its operation is based on the principles of the Seebeck effect. Therefore, the selection of the two metals to form a thermocouple depends on the range of temperature measurements.

1.6 Thermoelectric devices: Seebeck effect and Peltier effect

Taking advantage of the thermoelectric effect, one can build an efficient device combining *p*- and *n*-type conductors.[7], [8] Figure 1.3 represents the schematics of a simple thermoelectric device. It consists of an *n*- type leg and a *p*- type leg connected electrically in a series and thermally in parallel. When a temperature gradient is maintained, as shown in Figure 1.3a, holes flow from the hot to the cold end in *p*-type legs and electrons flow from hot to the cold end in *n*-type legs and thus a useful voltage is produced by means of the Seebeck effect. The operation of this device by injecting a small amount of current (Figure 1.3b) at the bottom of the *n*-type leg will result in a current flow in the upward direction through the *n*-type leg because electrons are negatively charged (electrons flow down the leg) and those electrons carry the heat away from the cold sink and it dumps at the bottom (hot sink). Thus, the top sink gets colder and the bottom sink gets hotter. The generation of cooling by applying current through the device is known as the Peltier effect. It is easier to think in terms of holes in the *p*-type leg.

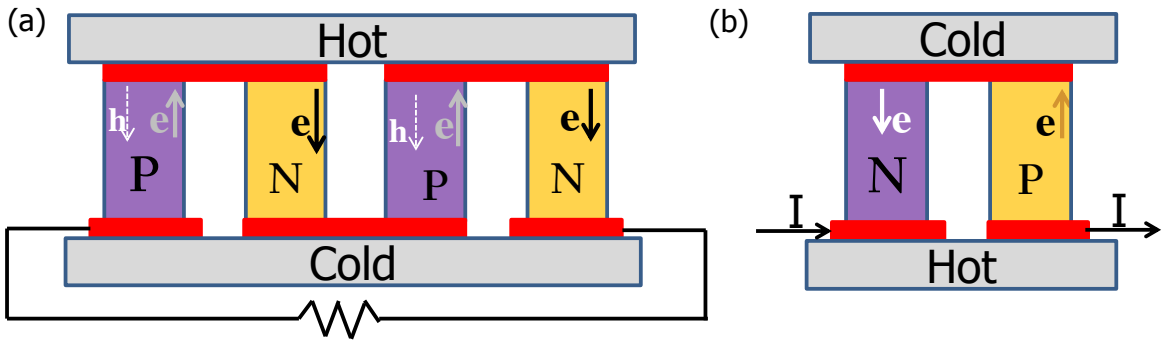

Figure 1.3 Schematic illustration of a thermoelectric device: (a) Thermoelectric device for power generation by means of Seebeck effect and, (b) Thermoelectric spot cooling by means of Peltier effect. Metal contacts are represented by red blocks.

However, there is an alternative way to look at these phenomena. When the thermoelectric transport parameters are derived, only the electrons that flow below or above the Fermi energy are taken into consideration. Thus, the operation of the device can also be

understood in terms of only electron flow. Considering that the current (I) that flows out from the cold to the hot part in the *p*-type leg, as shown schematically in the middle of Figure 1.4. The electrons flow in the reverse direction from hot to the cold sink through the *p*-leg [from the contact metal to *p*-type leg]. The electrons that flow through the different contacts; are described schematically from panel (a) to panel (d) in Figure 1.4. The metal contacts are shown by the square shaped shaded area in Figure 1.4. Current flows at the Fermi energy or very close to the Fermi energy in a metal. When it enters the *p*-type leg from the metal contact (Panel a_Figure1.4), an electron has to loose thermal energy to move from Fermi energy of the metal to an empty state or holes in the *p*-type leg. Therefore, Peltier heating occurs at the bottom of the *p*-type leg. In the *p*–metal contact at the cold sink (panel_b in Figure 4.12), the electron has to find an empty state near the Fermi energy by absorbing thermal energy in order to move to the metal contact. Thus, Peltier cooling happens at the top contact.

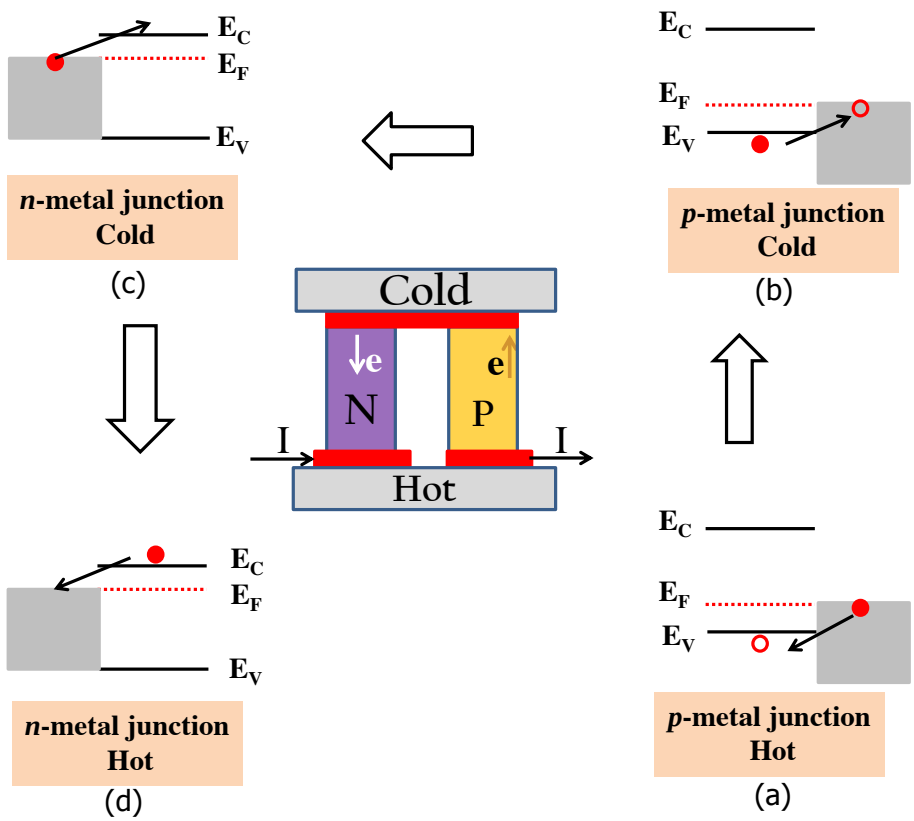

Figure 1.4 Flow of electricity in a *p*-and *n*-pair of a Peltier device considering only the electron flow. Description was given from panel (a) to panel (d).

The electrons flow from the metal to the *n*-type leg (panel_c in Figure 1.4). Consequently, in this case, the electrons in the metal make contact with the conduction band of the *n*-type leg. Electrons have to move (drift) from the Fermi energy of metal to the bottom of the conduction band of *n*-type leg. So again, electrons must absorb some thermal energy to move to the conduction band and thus, additional Peltier cooling happens at the top contact of the device. The electrons then flow down to the bottom of the *n*-type leg and when they come into contact with the metal, the electrons from the conduction level have to move to the Fermi level releasing some thermal energy. Therefore, the overall function of the device can well be understood only in terms of flow of electrons. The coefficient of performance or the efficiency of such Peltier device can be expressed as follows:

$$\eta = \frac{q_c^{max}}{P_{input}} \qquad (1.2)$$

where, q_c^{max} is the heat output at the cold end and P_{input} is the power input. Conversely, we can use this device in an operating mode, which is called thermoelectric power generation mode, where heat can be converted into electricity. In this case, the top plate should be kept hot, while the bottom end is kept cool (Figure 1.4). So, the electrons (or holes) will be diffused from the hot to the cold end. As the electrons in the *n*-type leg flow down from the hot to the cold end, the current flows in the reverse direction. Then the electrons flow from the *n*-type to the metal at the top. Consequently, electrons flow from the metal to the *p*-type leg at the top and from the *p*-type leg to the metal at the bottom. If the circuit is completed and current flows through a load, as in a motor or an electric bulb, then thermoelectric power generation is achieved. The efficiency of the process can be determined by the ratio of the power output (P_{out}) to the heat power input (P_{in}), as follows:

$$\eta = \frac{P_{out}}{P_{in}} \qquad (1.3)$$

The efficiency of such thermoelectric generator is related to the thermoelectric figure of merit as follows[4]

$$\eta_{max} = \frac{\Delta T}{T_{hot}} \cdot \frac{\left(\sqrt{1+zT}\right) - 1}{\left(\sqrt{1+zT}\right) + \frac{T_{cold}}{T_{hot}}} \qquad (1.4)$$

The efficiency of the device is related to the properties of materials, called thermoelectric figure of merit, zT, a dimensionless quantity which is defined as follows:

$$zT = \frac{S^2\sigma}{\kappa_L + \kappa_e}T \qquad (1.5)$$

where, S is the thermopower or Seebeck coefficient, σ is the electrical conductivity, T is the absolute temperature, κ_L is the lattice thermal conductivity and κ_e is the electronic part of the total thermal conductivity. Thus, the efficiency of thermoelectric power generating device will be higher if the figure of merit, zT, is higher. The variation of efficiency with zT is shown in Figure 1.5. Therefore, in order to achieve higher zT, the power factor, σS^2 should be high along with a low κ_{total} ($\kappa_{total} = \kappa_L + \kappa_e$). The main goal of thermoelectric research is to increase the zT of *p*-type and *n*-type materials with sustainable stability.

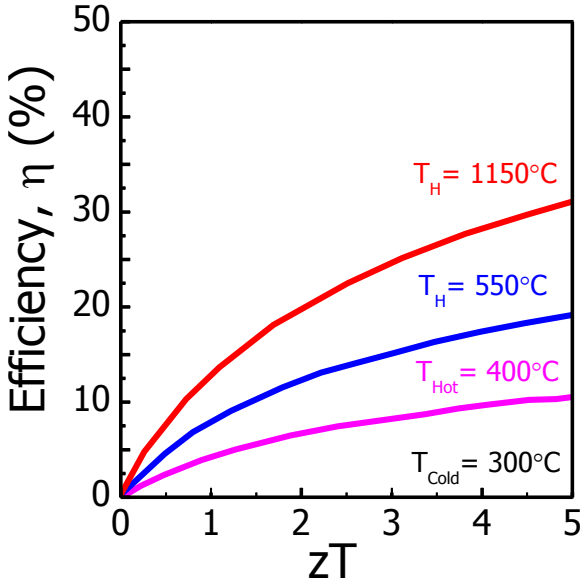

Figure 1.5 Achievement of Carnot efficient with increasing Figure of merit at fixed temperature gradient. Data reproduced from the literature.[10]

1.7 Ideal thermoelectric materials

An ideal thermoelectric material needs to have high electrical conductivity (σ), which is a characteristic of metals; low thermal conductivity (ϰ), which is characteristics of glass or glass like materials; and high Seebeck coefficient (S), which is a characteristic of semiconductors. Thus, the ultimate challenge in this field of thermoelectric research is to integrate all three properties together in a single material. Semiconductor materials are the best choice in the sense that they show a high S and the electronic and thermal transport (electronic part) can be tuned by controlling the carrier concentration.

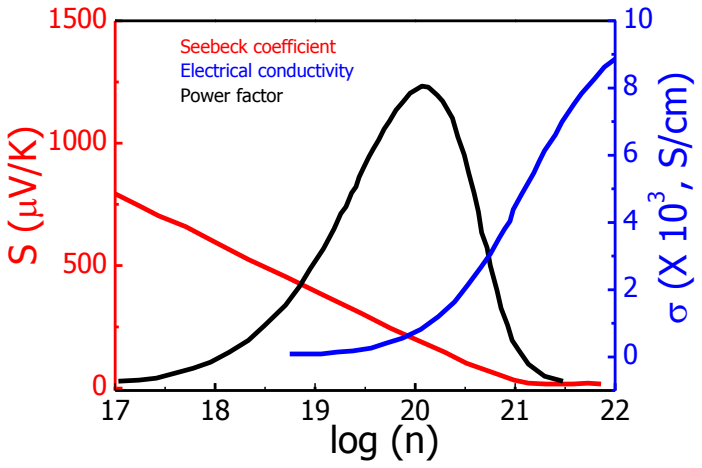

Figure 1.6 Seebeck coefficient, electrical conductivity and power factor as a function of carrier concentration. The optimized carrier concentration should be within 10^{19} to 10^{20} cm^{-3} to achieve maximum power factor for heavily doped semiconductors. Data taken from ref [5]

Figure 1.6 shows the dependence of the thermoelectric transport coefficients on charge carrier concentration. At very low carrier concentrations (for example in un-doped semiconductors), S is high, σ is low and the electronic part of thermal conductivity (κ_e) is low. Consequently, the overall thermoelectric performance is low. On the other hand, at high carrier concentrations (e.g., for metals), σ is very high and consequently, κ_e is also high due to Wiedemann-Franz law (κ_e is proportional to σ) and, S is very small. Therefore, the overall performance is low at high carrier concentration ranges. Thus, electron density should be optimized somewhere in between in order to obtain the best power factor or the figure of merit. To achieve a maximum power factor and overall figure of merit, carrier concentration must be within the range of 10^{18} to 10^{20} cm^{-3}.

The Seebeck coefficient (S) is strongly dependent on the shape of the density of states (DOS) near the Fermi energy (E_F) according to Mott's expression of S for degenerate semiconductors or metals:

$$S = \frac{\pi^2 \kappa_B^2 T}{3e} \left[\frac{d\{ln\sigma(E)\}}{dE}\right]_{E=E_F} \qquad (1.6)$$

In order to increase S, it is important to introduce a large derivative of σ (E) near the Fermi energy (E_F) [σ (E) is proportional to DOS]. Based on this concept, it was proposed to reduce the dimension of materials which can modify the shape of DOS at E_F. Such confinements

produce large Seebeck coefficient. The modification of the shape of DOS can be achieved by reducing dimensions from 3D materials to 2D (electron gas)[9], to 1D (nanowires)[10] and hence 0D (quantum dots) materials. Thus, the concept of nanostructure was introduced in the field of thermoelectric and the theory was tested experimentally.[11]

Linear response of power factor with electrical conductivity is not always advantageous. This is due to the fact that the electronic part of the thermal conductivity increases due to Wiedeman-Franz's law:[1]

$$\kappa_e = L.\sigma.T \qquad (1.7)$$

where, L is the Lorentz number. The only parameter which is not related to the electronic structure of materials is the lattice part of the thermal conductivity, κ_L.

$$\kappa_L = \frac{1}{3} C_v.l.v_S \qquad (1.8)$$

where, C_v is the specific heat at constant volume, l is the mean free path of phonons and v_S is the velocity of sound in that medium. At relatively low temperatures, thermal conductivity is dominated by the specific heat according to Debye's T^3 law whereas, at relatively higher temperatures, C_v approaches its classical value of 3R (R is universal gas constant). Therefore, at higher temperatures, thermal conductivity is a function of the mean free path of phonons. Many authors have reported an enhanced overall thermoelectric figure of merit by lowering the lattice part of the thermal conductivity via engineering the crystal microstructure.

A large number of compounds have shown high thermoelectric figure of merit including skutterudites,[12] clathrates,[12] half-heusler intermetallic compounds,[13] b-Zn4Sb_3,[14] the zintl phase $Yb_{14}MnSb_{11}$,[15] $NaCoO_2$,[16] misfit cobalt oxides,[17] bismuth chalcogenides,[18] Bi_2Te_3,[19] LAST[19] $AgPb_mSbTe_{2+m}$ and, PbTe.[20]

1.8 Oxide thermoelectrics

Commercially used thermoelectric materials are heavily doped narrow band gap chalcogenides mostly based on Bi_2Te_3–Sb_2Te_3 alloys. The doped elements are either Sb (for Bi) or Se (for Te). The reliability of these parent and doped materials is troublesome because of their toxicity, which limits there use and, more importantly, because of their low abundance and high cost, particularly for tellurium. Many traditional thermoelectric materials are limited to operation at low temperatures to avoid sublimation, oxidation or degradation of the constituting

phase. Oxide thermoelectric materials are advantageous in this regard. Oxides are non-toxic, relying on more abundant transition metals, having high temperature stability, corrosion resistance and, an easy and scalable synthesis route.

Oxide materials were thought to be inefficient for thermoelectric application due to their high thermal conductivity (because of their light constituent atoms) and poor electron mobility (due to localized electrons). Recently, the discovery of large thermoelectric power with metallic electrical conductivity in $NaCo_2O_4$ crystal[16] has attracted research, as depicted in Figure 1.7. Interestingly, the carrier concentration is within the range of 10^{20}-10^{22} cm^{-3}, and it still shows a high S, low thermal conductivity which leads to figure of merit, $zT > 1$ at a high temperature.

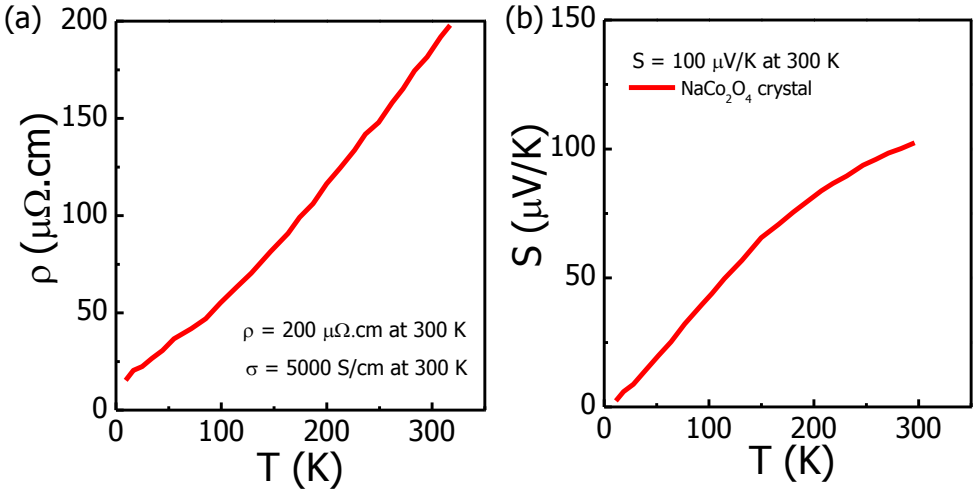

Figure 1.7 Thermoelectric transport properties (Digitized data from Ref 16). Temperature dependent (a) electrical resistivity and, (b) S of $NaCo_2O_4$ crystal.

The use of oxides, which naturally present a layered structure, could be a strategy to decouple electronic and thermal transport as has been observed in different types of cobaltates, such as Na_xCoO_2 and in misfit cobaltates. In this regard, this thesis focuses on two different types of cobaltates both showing layered structures: misfit cobaltates, which have an edge sharing triangular CoO_2 lattice[21] and, double perovskites $GdBaCo_2O_{5+\delta}$ of the $RBaCo_2O_{5.5}$ (R = Lanthanides) family,[22] which have a corner sharing square CoO_2 lattice in their unit cell.

1.9 Triangular CoO_2 lattice

1.9.1 $Na_{0.5}CoO_2$

Na_xCoO_2 has a CdI_2 type layered structure of a CoO_2 layer sandwiched between disordered sodium ions.[23] There are some interesting features that make this class of compounds different from conventional degenerate semiconductors or metals. Firstly, the coexistence of large *S* power and metallic electronic conductivity.[16] Secondly, its zT > 1, where the carrier concentration is one order of magnitude larger than the optimized carrier concentration for classical band gap semiconductors (see Figure 1.6). Thirdly, low thermal conductivity, even if the electron density is high.[24] A comparison of commercially used heavily doped Bi_2Te_3 with the recently discovered Na_xCoO_2 in Table 1.1 provides a clear view of the potential of oxide materials, which can be suitable alternatives for heavily doped metal chalcogenides for potential thermoelectric applications.[16] A comparison of the promising *p*-type cobaltates and other *n*-type other oxide thermoelectric materials is presented in Figure 1.8.

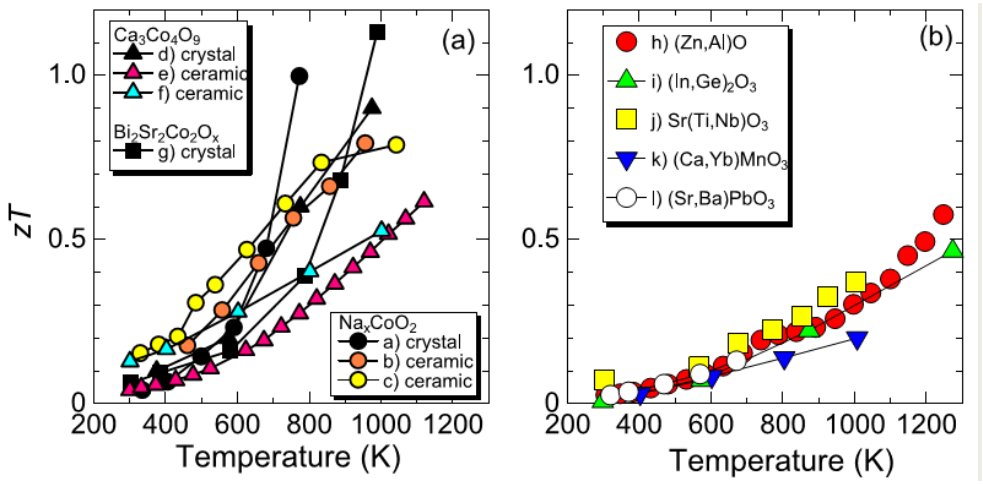

Figure 1.8 Dimensionless figure of merit, zT. (a) *p*-type oxides and, (b) *n*-type oxides. Data taken from literature:[7]

Table 1.1: Comparison of the thermoelectric transport coefficient of Bi_2Te_3 and $Na_{0.5}CoO_2$ (also represented as $NaCo_2O_4$) at 300K (Taken from ref 16).

Sample	ϱ (mΩ.cm))	S (μV/K)	PF (μW/cm.K^2)
Bi_2Te_3	1	200	40
$Na_{0.5}CoO_2$	0.2	100	50

The temperature dependent electrical resistivity of $Na_{0.5}CoO_2$ reveals a metallic character (in-plane) as shown in Figure 1.7. Resistivity increases with increasing temperature from a few Kelvin to 300 K and the S (T) follows a similar trend, as expected from Mott's expression of S for metals. In equation 1.6, S_{Mott}, e, κ_B, T, $\sigma(E)$ and E_F represent Seebeck coefficient from Mott's expression, electronic charge, Boltzmann constant, absolute temperature and energy dependent electronic conductivity, respectively. The interesting point is that the S (~100 μV/K) is 10 times higher at 300 K than the estimated from such a high carrier density and electrical conductivity for metals.[25] Naturally the question arises as to why S is higher in spite of having metallic electrical resistivity at 300 K? According to D. Singh and his co-workers,[26, 27] the S at 300K can be reproduced from metallic resistivity using Boltzmann transport theory (BTT). Consequently, no new physics is needed to interpret the coexistence of metallic resistivity and large S at 300 K. But few other properties, such as magnetic field dependence on the S at few Kelvin temperature were explained in terms of spin-entropy by Wang et al.[25] On the other hand, Singh et al[28] showed later that the magnetic field effect of S can be explained from BTT combined with a spin-polarized density functional theory.

Spectroscopy and electronic band structure

Angle resolved photoelectron spectroscopy (ARPES) experiments revealed the electronic band structure of $NaCo_2O_4$.[29] The electronic transport properties of $NaCo_2O_4$ are controlled by the conducting CoO_2 hexagonal layer. Therefore, the valence band electronic states are dominated by the Co(3d)-O(2p) hybrid molecular orbitals.[30] An interesting fact from the spectroscopy is that the implementation of the knowledge of the electronic structure near Fermi energy to estimate the S by using Boltzmann transport equation for metals.[29] Temperature dependent S was calculated by analyzing the intensity of high resolution ultraviolet spectroscopy (VB-UPS) near E_F.[30] These estimations of temperature dependent S show a fairly good consistency with the measured values.[29] So, from the spectroscopic data it can be concluded that the unique electronic band structure, known as 'pudding mold' type[31] band structure, is actually responsible for the coexistence of large S and metallic resistivity.

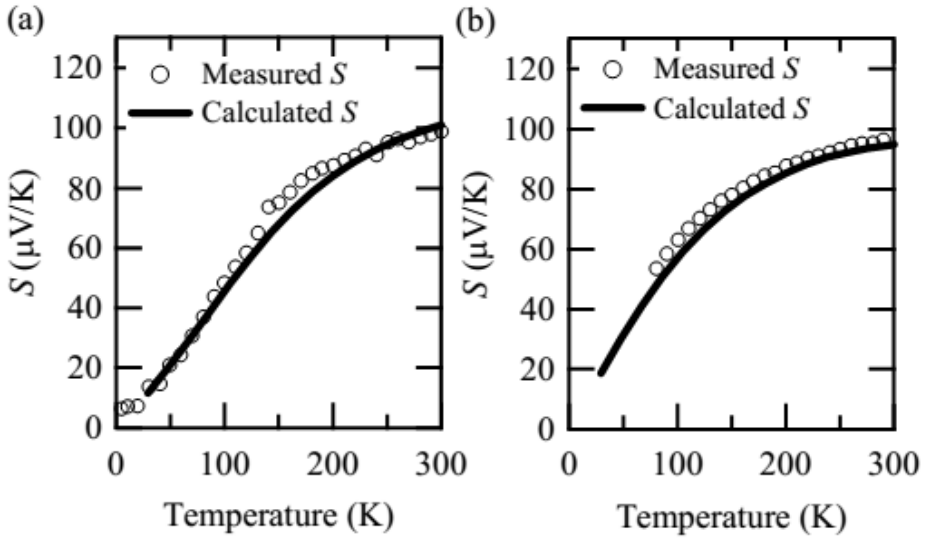

Figure 1.9 Experimentally measured thermopower and calculated from ARPES experimental data: (a) for $Na_{0.8}CoO_2$ and, b) $Na_{0.7}CoO_2$ crystal. Calculated values merge well with the measured data. Data taken from Ref 29 and 30.

1.9.2 Misfit cobaltates

There are challenges concerning the control of sodium concentration in Na_xCoO_2 to achieve the best thermoelectric performance as sodium is prone to form carbonates and it decomposes at 1100 K, [32] which eventually reduces overall performance. Use of calcium (or strontium) instead of sodium has provided more chemical stability.[33] Calcium cobaltates of $Ca_3Co_4O_9$ composition has been shown not only to stabilize the structure but it also to bring a tremendous change in the crystal structure.[21] This new type of structure consists of two different sub-units in the unit cell. One sub unit is rock salt (4-fold symmetry) type and the other is a hexagonal CoO_2 layer (3-fold symmetry), similar to the misfit Pb-Bi based chalcogenides,[34] popularly called misfit cobaltates. The name misfit is meaningful in the sense that the crystallographic b-axes of these two sub-units do not match (one is shorter than the other, q= b1/b2, misfit ratio) while it matches perfectly along the a- and c-axes as well as having different symmetries. More importantly, the newly developed rock salt type layer is electrically insulating in nature and sandwiched between electrically conducting CoO_2 hexagonal layers. For this reason, the misfit cobaltates are also called natural superstructures of electrically conducting and insulating layers. To date, many different families of misfit cobaltates have been discovered, which show excellent thermoelectric performance.[35], [36], [37], [38] Figure 1.10 shows how the structure evolves when the conducting CoO_2 layers were separated by different electrically insulating rock salt type layers (Figure 1.10c will be described later in chapter 3). More

interestingly, when the conducting hexagonal CoO_2 layers are separated by electrically insulating rock salt type layers, in place of disordered sodium ions, electron correlations appear that influence the electronic, thermoelectric transport properties, as depicted in Figure 1.11. For example, the resistivity of $NaCoO_2$ is metallic from room temperature down to a few Kelvin, while, for the misfit cobaltates, it takes an upturn (T ~ 20 K). A difference in the behavior of temperature dependent S has also been observed.[36] The S increases linearly with increasing temperature from a few Kelvin and it starts saturating at ~150 K. This unusual trend of temperature dependence of electrical resistivity and S is not well understood from the concept of diffusion of charge carriers.

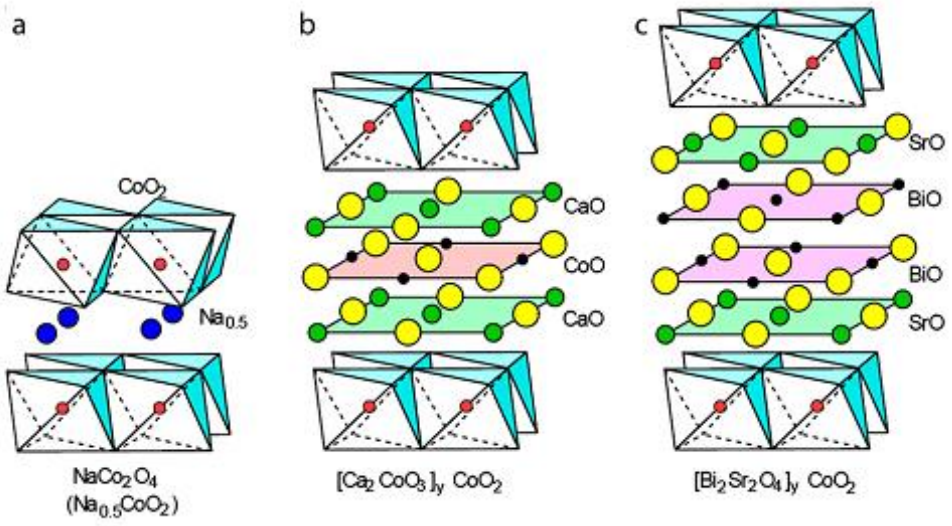

Figure 1.10 Crystal structures of a) $NaCo_2O_4$, b) $Ca_3Co_4O_9$ and c) $Bi_2Sr_2Co_2O_y$, reproduced from the literature. [22] The common features of the three structures are the triangular CoO_2 layer. Thus in plane a-parameter is similar for all crystals.

Research has diverged in two different directions. A large number of groups have devoted their research to understand the mechanism of the transport property in order to develop the optimal conditions for best thermoelectric performance and to search for the origin of high S, which is discussed later. Another approach has been to improve the overall figure of merit by doping, alloying [39], [40], [41] and controlling defect concentrations. [42], [43]

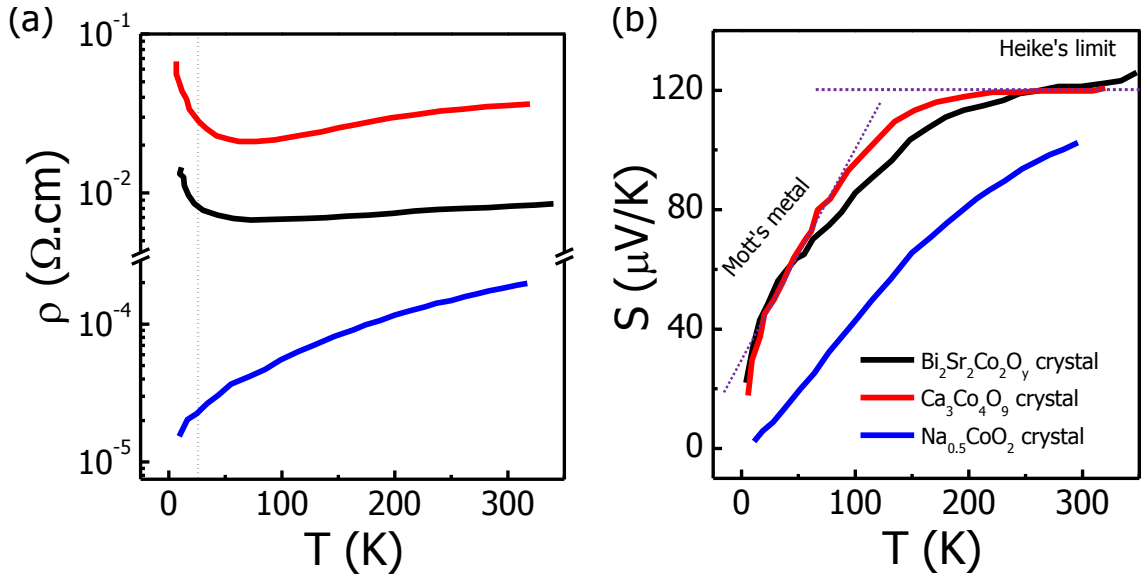

Figure 1.11 Comparison of the thermoelectric properties of $Na_{0.5}CoO_2$ and misfit cobaltates; a) temperature dependent electrical resistivity and b) temperature dependent Seebeck coefficient. This comparison shows how electronic and thermoelectric transport properties evolve when conducting triangular CoO_2 layers are separated by electrically insulating block layers. Data reproduced from the literature. [36], [25],[44]

1.9.3 High temperature limit of thermopower

An interesting question is why the S saturates at or before reaching room temperature. Taking into consideration the fact that the mean free path of electrons are at the unit cell level,[45] the best way of thinking of S is in terms of the distribution of the electrons into the available sites. This distribution determines the configuration entropy of the system, which is independent of temperature. For a system with localized charge carriers or polarons, the saturation temperature is close to room temperature, at least in case of misfit cobaltates. In this sense, S is a direct measurement of configurational entropy.[46] In the case of misfit cobaltates of mixed Co^{+4}/Co^{+3} pairs, the entropy arises from the distribution of Co^{+4} ions in the back ground of Co^{+3} ions.

A mathematical expression for the high temperature limit of S can be derived from the Boltzmann transport equation (although BTT does not account for localized carriers) followed by using the principles of thermodynamics.[46], [47] We start from the expression of S given in, equation 1.10 :

$$S(T) = -\frac{1}{eT}\frac{\int_{-\infty}^{+\infty}\sigma(E)\left[-\frac{df}{dE}\right][E-\mu_e]dE}{\int_{-\infty}^{+\infty}\sigma(E)\left[-\frac{df}{dE}\right]dE} \qquad (1.10)$$

which can be re written as

$$S\,(T) = -\frac{\mu_e}{eT} + \frac{1}{eT}\frac{\int_{-\infty}^{+\infty}\sigma(E)\left[-\frac{df}{dE}\right][E]dE}{\int_{-\infty}^{+\infty}\sigma(E)\left[-\frac{df}{dE}\right]dE} \qquad (1.11)$$

where, the first term is directly related to chemical potential (μ_e) and it can therefore be represented in terms of configurational entropy (S_c) from the principles of thermodynamics as follows:

$$\frac{\mu_e}{T} = -\left[\frac{\partial S_c}{\partial N}\right]_{E,V} \qquad (1.12)$$

where, 'N' is the number of transported charge, E is the energy and V is internal volume. Therefore, equation 1.11 can be represented as

$$S\,(T) = \frac{1}{e}\left[\frac{\partial S_c}{\partial N}\right]_{E,V} + \frac{1}{eT}\frac{\int_{-\infty}^{+\infty}\sigma(E)\left[-\frac{df}{dE}\right][E]dE}{\int_{-\infty}^{+\infty}\sigma(E)\left[-\frac{df}{dE}\right]dE} \qquad (1.13)$$

At very high temperatures, the second term of the equation 1.13 will be negligibly small and therefore, S (T) is only dependent of configurational entropy, which is given by Boltzmann as follows:

$$S_c = -\kappa_B \ln(g) \qquad (1.14)$$

Therefore, at very high temperatures, combining equation 1.12 and 1.14, one obtains the following expression where S is governed by the degree of degeneracy (g) or possible configurations of the system.

$$S\,(T) = -\frac{\kappa_B}{e}\left[\frac{\partial\{\ln(g)\}}{\partial N}\right]_{E,V} \qquad (1.15)$$

Degeneracy, g, of N number of particles distributed over N_V number of available sites (assuming that two particles cannot occupy the same state) can be expressed as,

$$g = \frac{N_V!}{(N_V - n)!\,n!} \qquad (1.16)$$

Taking logarithms of equation 1.16 (using Starling approximation) and substituting in equation 1.15, one obtains:

$$S\,(T) = -\frac{\kappa_B}{e} ln\left(\frac{1-\frac{N}{N_V}}{\frac{N}{N_V}}\right) \qquad or$$

$$S\,(T) = -\frac{\kappa_B}{e}\ln\left(\frac{1-x}{x}\right) \qquad (1.17)$$

where, *x* represents the ratio of number of particles over available crystal sites ($^{N}/_{N_V}$). It can be seen from the derived expression 1.17, that S is temperature independent. This expression is known as Heike's formula. This formula, is applicable when S is temperature independent, is typically observed for systems where $\kappa_B T$ is much higher than band width, *W* ($\kappa_B T \gg W$) or in other words, for systems with localized charge carriers (or polarons). The equation 1.17 holds for electrons. For holes, it can be written as,

$$S\,(T) = -\frac{\kappa_B}{e}\ln\left(\frac{x}{1-x}\right) \qquad (1.18)$$

Furthermore, Bach et al.[48] have shown that if every particle occupies two sites, then the degeneracy can be expressed as, $g = \frac{\frac{N_V}{2}}{\left(\frac{N_V}{2}-N\right)!N!} = \frac{2N}{N_V} = 2x$. Therefore, if the number of sites occupied by every charge is Q, then Heike's formula can be represented as shown in equation 1.19, where Q represents the size of the polarons.

$$S_{T\to\infty} = -\frac{\kappa_B}{e}\ln\left(\frac{1-Q.x}{Q.x}\right) \qquad (1.19)$$

Chaikin and Beni [46] also calculated the degeneracy and corresponding Heike's formula for systems with interacting carriers. For example, the system of fermions with spins, when, $\kappa_B T$ is much higher than on site Coulomb repulsion, U ($i.e.\kappa_B T \gg U$) and, Heike's formula can be modified as shown in equation 1.20. In this case, the spin up and spin down electrons are distributed over N_V sites independently.

$$S_{T\to\infty} = \frac{\kappa_B}{e}\ln\left(\frac{2-x}{x}\right) \qquad (1.20)$$

Therefore, temperature independent S observed for misfit cobaltates around 200 to 300 K are considered to be the high temperature limit following the expression obtained from Heike's formula for holes. The advantage of Heike's formula (1.11 and 1.18) is that S can be optimized simply by controlling, *x* (concentration of holes or electrons per unit cell) to obtain best

thermoelectric performance as shown in Figure 1.12. *x* is the ratio of number of carriers to available crystal sites can be defined as the number of carrier concentration per unit cell if two particles do not occupy the same site. Therefore, if *x* is known at the high temperature limit, for instance from *S*, the *x* can be readily calculated from the Heike's expression by equation 1.17 and 1.18.

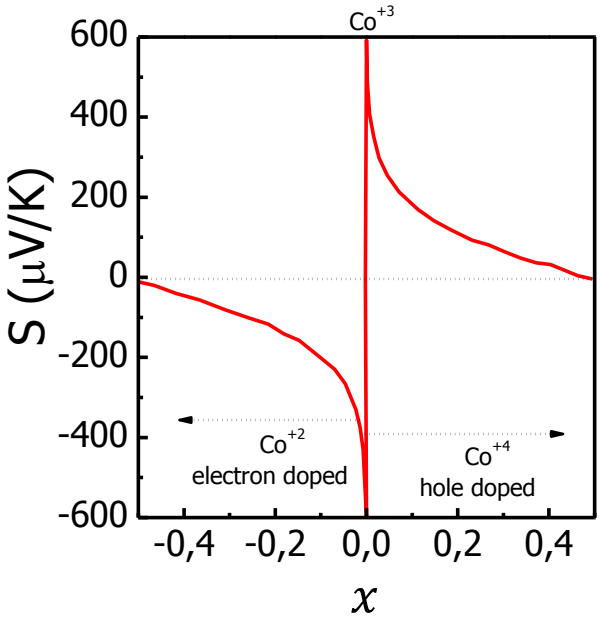

Figure 1.12 Seebeck coefficients as a function of *x* at high temperature from Heike's formula. Data digitized from Ref 31. The graph becomes discontinuous at *x*=0.

1.9.4 Valence of cobalt ion and spin-orbit degeneracy

The Hall effect is still not understood very well yet for misfit cobaltates. For example, the valence of cobalt ions calculated from iodometric titration,[49] magnetic succeptibility,[50] ARPES[51], [30] and NMR spectroscopy[52] does not really match with the valence calculated from the Hall effect, despite the fact that Hall effect is a direct measurement of carrier concentration. Therefore, the calculated thermopower (*S*), from equation 1.18 always overestimates the measured *S* at 300 K. As a result, there is a discrepancy between the Hall effect and other measurement (See Table 1.2) in calculating the valence state of cobalt ions.

Table 1.2 Discrepancy of the valence calculation of cobalt ion in misfit cobaltates.

ARPES [BiBaCoO]	NMR spectroscopy	Magnetic susceptibility [BiCaCoO]	Hall effect
3.3 Ref: 52	3.1-3.3 Ref: 53	3.24 Ref 50, 51	3.05-3.15

Koshibae et al[53], [54] came up with an idea that probably satisfies the discrepancies at 300 K in the Hall effect as well as giving an explanation for the origin of the high *S* (~100 μV/K) at 300 K for misfit cobaltates. The authors introduced an extra term related to entropy, called spin-orbit degeneracy, in order to modify Heike's formula, as presented in equation 1.21 where, β represents the ratio of the spin-orbit degeneracy of Co^{+3} and Co^{+4} ions. The reasoning behind this modification is entropy based on the spin and orbital degrees of freedom associated with the electron that must contribute in addition to entropy calculated from Heike's formula. Initial support for this idea came from the suppression of *S* by a magnetic field at few Kelvin temperatures.[25] Thus, according to the modified Heike's formula, the net entropy contribution at a high temperature limit has two different contributions. The first term is the entropy related to charge carrier distribution (classical Heike's formula) and the second term is the entropy contribution related to the coupled spin-orbit degrees of freedom. As can be seen that the modified Heike's formula (equation 1.21) is not generalized any more for the systems of localized charge carriers; rather it has become specific for the systems of mixed cobalt valence compounds. Other authors have used this formula in case of other mixed valence compounds, such as manganites and, nikelets.[55]

$$S_{T\to\infty} = -\frac{\kappa_B}{e}\ln\left(\beta\frac{x}{1-x}\right) \qquad (1.21)$$

$$S_{T\to\infty} = -\frac{\kappa_B}{e}\ln(\beta) - \frac{\kappa_B}{e}\ln\left(\frac{x}{1-x}\right)$$

$$S_{T\to\infty} = S_{spin-orbit\ degeneracy} + S_{configurational\ entropy}$$

Before discussing how it satisfies both the discrepancies, the additional entropy term called 'spin-orbit degeneracy' is illustrated. The spin-orbit degeneracy (SOD), β, is actually the ratio of the SOD of Co^{+3} and Co^{+4} ions. This term is typically introduced in the systems having mixed valence ions (of transition metal ions) as in this case, for the mixed Co^{+3} and Co^{+4} ions in the misfit cobaltates. The spin-orbit degeneracy is a product of spin degeneracy and orbital degrees of freedom.

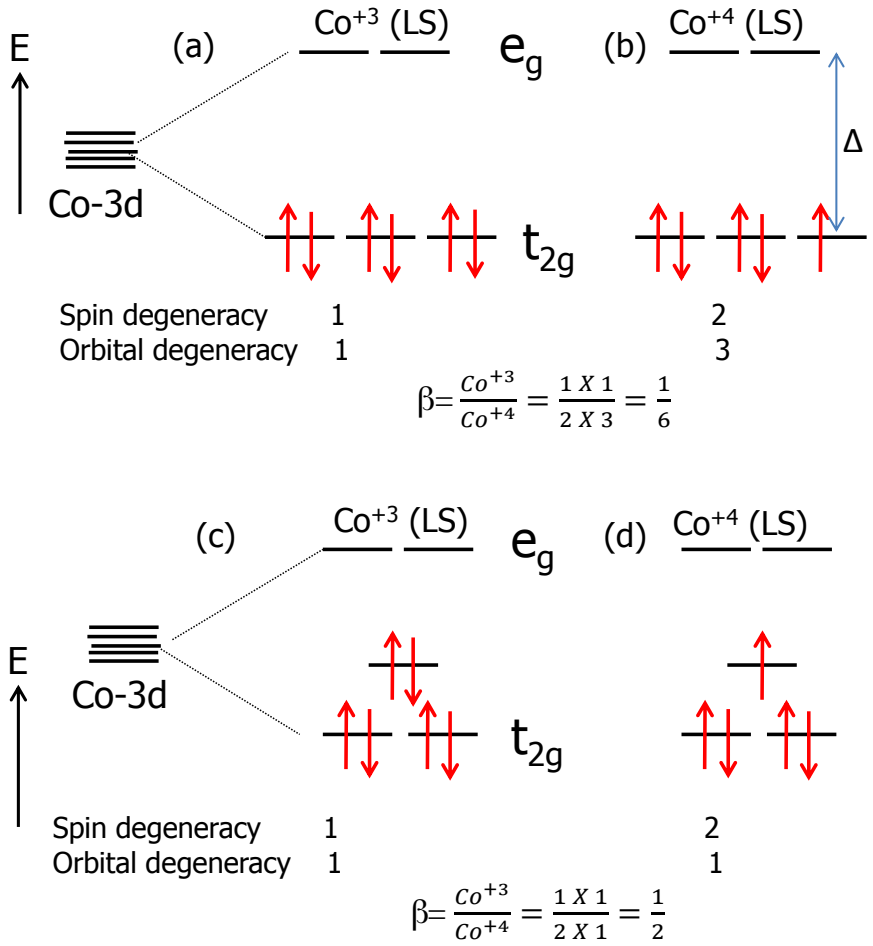

Figure 1.13 Schematics of the crystal field splitting of the cobalt ions in misfit cobaltates; (a) for Co^{+3} (LS) ions and, (b) in right, for Co^{+4} ions in an octahedral coordination; (c) and, (d) splitting of energy levels of Co^{+3} (LS) and, of Co^{+4} ions due to orthorhombic tilting of CoO_2 lattice.

Assuming that a transition metal ion M^{+n} (for example Co^{+3}) is situated at the center position of an octahedral coordination. Figure 1.13 depicts the case of cobalt ions in misfit cobalt oxides. In the absence of an external crystal field, all five 3d energy levels are degenerate. When the ligand, oxygen atoms in our discussion, (with lone pair, ns^2) approaches the M^{+n} ions from x, y and z-crystallographic direction, the energy level of 3d orbitals increases. When the separation

of 2p-orbitals of O and 3d-orbitals of M^{+n} is close enough to overlap each other, the 3d-orbitals split into two different sets of orbitals, called t_{2g} and e_g levels, creating a gap in between them, called crystal field splitting (Δ). The filling of the electrons in the orbitals will take place according to Hund's rule of spin-multiplicity and Pauli's exclusion principle. Depending on the crystal field splitting, the orbital degeneracy can be lifted. The orbital degeneracy is the number of possible ways the energy levels can be arranged. The spin degeneracy is actually spin-multiplicity $(2S_m + 1;\ S_m = \sum_i s)$ where 's' is the spin of an unpaired electron. For misfit cobaltates, the spin-orbit degeneracy can be calculated as depicted in Figure 1.13. Spin-orbit degeneracy was calculated for cobalt ions of different electric and orbital configurations using the following equation as shown in Table 1.3 and in Figure 1.13.

$$g_{spin} = S_m = \left(2\sum_i s\right) + 1$$

$$g = g_{spin} \times g_{orbital}$$

Table 1.3 Calculation of spin-orbit degeneracy for transition metal ions having different spin states, assuming all ions are in octahedral sites (no orthorhombic tilt was considered):Taken from[47]

Ions with 3d electrons	Spin states	Spin degeneracy, 2S+1	Orbital degeneracy	Spin-orbit degeneracy, g
Co^{+3} $(t_{2g}^6 e_g^0)$	LS	1	1	1
Co^{+3} $(t_{2g}^5 e_g^1)$	IS	3	6	18
Co^{+3} $(t_{2g}^4 e_g^2)$	HS	3	5	15
Co^{+4} $(t_{2g}^5 e_g^0)$	LS	2	3	6
Co^{+4} $(t_{2g}^4 e_g^1)$	IS	4	6	24
Co^{+4} $(t_{2g}^3 e_g^2)$	HS	6	1	6

Case I: Calculation of valence state of cobalt oxide by modified Heike's formula

As shown in Figure 1.13, octahedral splitting provides a β value of 1/6 and if the degeneracy is lifted by the rhombohedral splitting,[49] this could result in a β value of $1/2$. The other parameter, *x* can be calculated from measured *S*, as depicted in Table 1.4. Estimated valence in misfit cobaltates from $\beta = 1/6$, is rather higher than estimated from other methods (highlighted in red color). On the other hand, using the $\beta = 1/2$, the estimated valence of cobalt is in very close in agreement with other measurements (highlighted in violet color).

Table 1.4 Valence of cobalt ion with the additional spin-orbit degeneracy term to Heike's formula

Heike's with β= ½ at 300K	Heike's with β= 1/6 at 300K	ARPES [BiBaCoO][51]	NMR spectroscopy[52]	Magnetic susceptibility [BiCaCoO][49], [50]	Hall effect
3.24	3.5 - 3.7 (β= 1/6 instead of 1/2)	3.3 Ref: PRB **76**, 100403, 2007	3.1-3.3 Ref: PRB **76**, 100407, 2007	3.24 Ref: JAP **101**, 083708, 2007	3.05-3.15 Ref: JPCM **21**, 235404, 2009

Case II: Estimation of thermopower for $NaCoO_2$

Koshibae et al[53] estimated *S* for $NaCoO_2$ from a modified formula shown in equation 1.21. As mentioned before, the initial idea came from the suppression of *S* at a few Kelvin by magnetic field and they extended their formulation to calculate a high temperature limit of *S* for $NaCoO_2$. As, the composition of $NaCoO_2$ is stoichiometric meaning that the valence of cobalt is +3, the estimated value of x=0.5. This reflects that the classical Heike's formula results a zero value of thermopower at the high temperature limit. However, modified Heike's formula results in a value of +154 μV/K, considering $\beta = 1/6$ which is close in agreement to the measured value +100 μV/K. In-spite of this success, some other facts remains unresolved, as follows:

i) Calculation of S from $\beta = 1/2$ will result in a value of +598 μV/K, which will overestimate the measured value of S for $NaCoO_2$. It was shown in case I that it is more likely that the possible β value for misfit cobaltates is 1/2 due to splitting of t_{2g} level.

ii) The $NaCoO_2$ does not show a saturation of S with increasing temperature up to 300 K, rather it is expected to happen even at higher temperatures.[16]

iii) Suppression of S with the magnetic field at a few Kelvin of $NaCoO_2$ was also explained from Boltzmann transport theory where $NaCoO_2$ is metallic.[28]

Nevertheless, at high temperature limit, modified Heike's formula was further extended to

i) A tool for indirect determination of the spin states of Co^{+3} or Co^{+4} ions, from the measured Seebeck coefficient at 300 K. It was claimed that Co^{+4} ions have high spin states in $Ca_3Co_4O_9$ thin film and bulk polycrystalline samples.[56],[57]

ii) The second argument was the S can be improved by tuning with the spin-orbit degeneracy, without much affecting the electrical resistivity. So, some authors in the literature started looking for new materials based on this concept.[58], [59] For example, a difference in the S of $Bi_2Sr_2CaCu_2O_{8+\delta}$ (BSCCO) and misfit cobaltates was claimed due to the absence of spin-orbit degeneracy in BSCCO system.[60]

Recently, Rivas-Murias et al,[61] pointed out that the room temperature S of misfit cobaltate thin films can be well understood at 300 K without the addition of the spin-orbit degeneracy (i.e., considering β=1) factor to Heike's formula. They argued that the discrepancy of the Hall effect can be understood from the presence of multiple carriers (localized and itinerant) in the system. This experimental result makes the validity of spin-orbit degeneracy questionable.

Scope of experiment I

From the above descriptions, it can be seen that the role of spin-orbit degeneracy on the high temperature limit of S is unclear. On the other hand, there is a discrepancy of the Hall effect electron density in the calculation of the valence state of cobalt ion. Therefore, we aimed to test such discrepancy and verify the role of spin-orbit degeneracy in case of $[Bi_2Sr_2O_{4-\delta}]^{RS}[CoO_2]q$ thin films in the incoherent transport region, which are presented in chapter 3.

1.10 Double perovskite layered cobaltates

1.10.1 General features of $LnBaCo_2O_{5.5\pm\delta}$ family of compounds

Double perovskites of $LnBaCo_2O_{5+\delta}$ (Ln = Gd, Ho, Nd, Pr)[62], [63] have attracted the attention of many researchers because of their versatile properties due to spin-charge-lattice interactions. These compounds have common features in their structural, electrical, magnetic and magneto transport properties. First, the crystal structure is double perovskite due to oxygen and cationic ordering in the specific crystallographic direction. Two types of coordination geometry in CoO_2 layers are present in the crystal structure; pyramidal (P_y) and octahedral (Oct), which result in different spin states of cobalt ions, as depicted in Figure 1.14. Secondly, these compounds generally exhibit a metal-insulator transition at ~360 K[64] as shown in Figure 1.15. Third, they may show spin blockade phenomena which prevent the motion of Co^{+2} ions in the Co^{+3} backgrounds. Fourth, they show a complex magnetic phase diagram.[65] Fifth, some of these compounds show high thermoelectric power at ~100 K.[66]

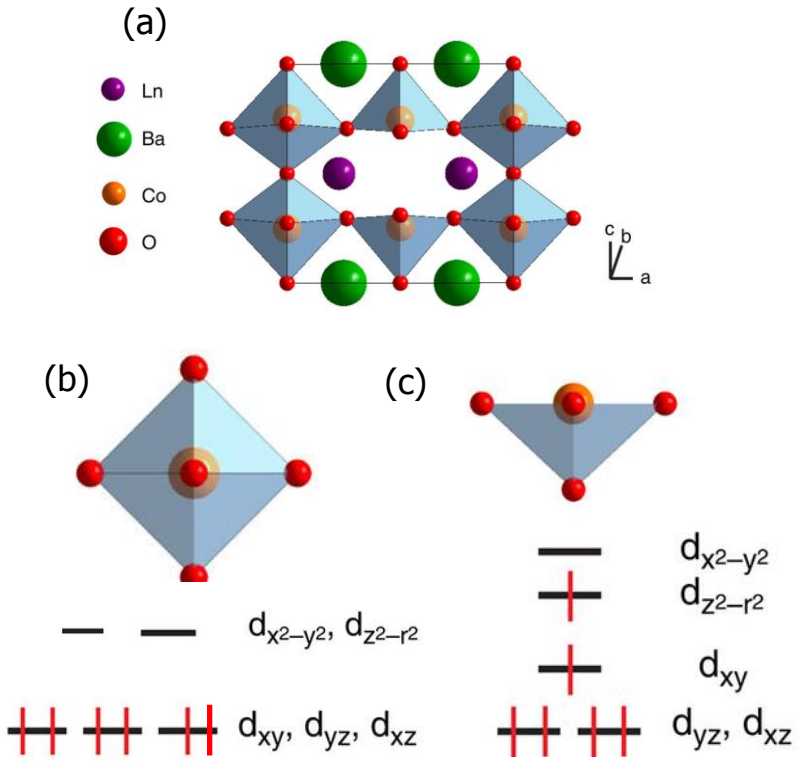

Figure 1.14 Crystal structure and the crystal field splitting.[46] (a) Schematic illustration of the crystal structure of double perovskite $LnBaCo_2O_{5.5\pm\delta}$ (Ln = Gd, Ho, Nd, Pm), (b) octahedral CoO_2 lattice and the spin states due to crystal field splitting and, (c) square pyramidal coordination of cobalt ions with different crystal field splitting of d-electronic states.

1.10.2 Transport properties of GBCO crystals

Our focus will be on the electronic and thermoelectric transport properties of $GdBaCo_2O_{5.5\pm\delta}$ systems (GBCO). Temperature dependent electrical resistivity and thermopower of a wide range of oxygen stoichiometry of GBCO crystals are depicted in Figure 1.15. Some of the interesting features are described below.

Metal-insulator transition (MIT)

Stoichiometric (δ=0) and electron doped (δ<0) GBCO crystals show sharp MIT at ~360 K. Hole doped (δ>0) GBCO crystals also exhibit a sharp MIT at relatively lower temperatures (320 K for δ = +0.15) and almost no clear transition can be found for δ > +0.2. It is believed that the metal-insulator transition (MIT) is associated with a spin state transition of Co^{+3} (LS, $t_{2g}^6e_g^0$→HS, $t_{2g}^4e_g^2$) in the octahedral coordination geometry.[64], [67] It was concluded that LS→HS state transition injects electrons into e_g orbitals from t_{2g} orbitals thus decreasing the electrical resistivity.

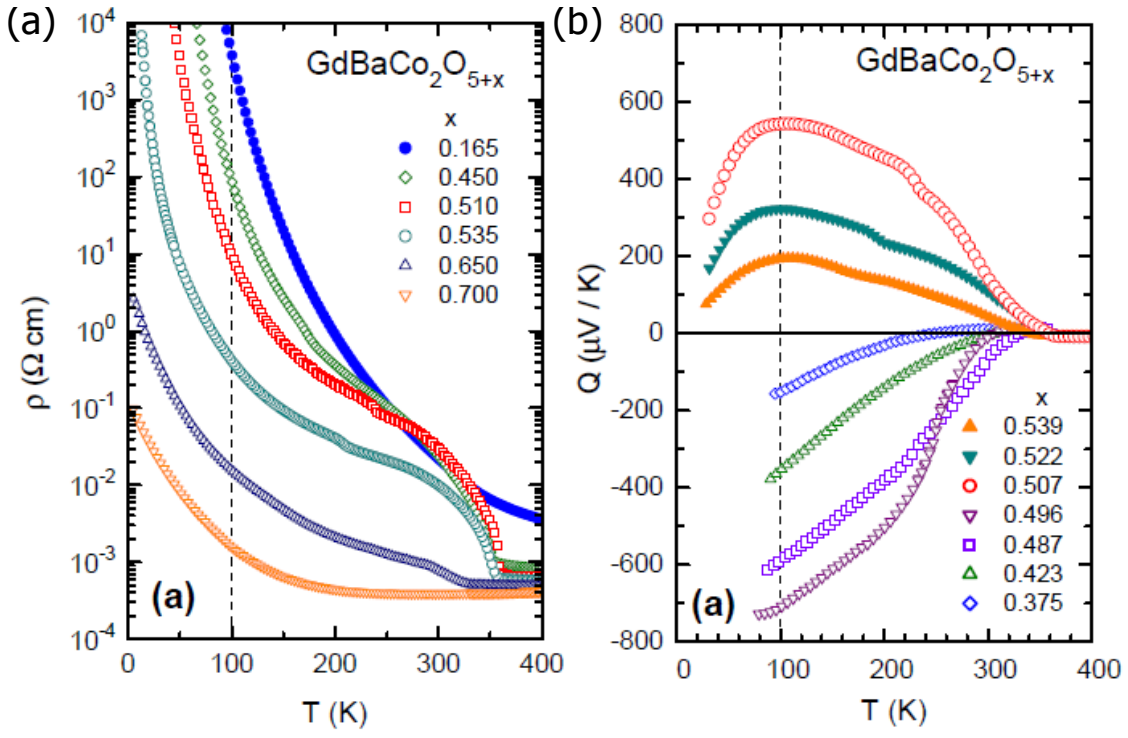

crystals. (a) Temperature dependent electrical resistivity and, (b) temperature dependent Seebeck coefficient of GBCO crystals of variable oxygen stoichiometry. Data reproduced from the literature.[49]

Electron-hole asymmetry

Doping (in CoO_2 layer) dependence on electrical resistivity shows no such clear trend at 300 K or above. But, at 100 K, it is apparent that there is an asymmetry in doping dependence of on resistivity. Electrical resistivity decreases on hole doping as expected but, resistivity increases with electron doping. Such an asymmetry in doping was explained by spin-blockade effect which is discussed in the following paragraphs.

Symmetric doping dependence on Seebeck coefficient (S)

The effect of electron and hole doping on *S* does not show a clear trend at 300 K or above. But, at 100 K, *S* shows a clear change in sign when it is electron or hole doped. The interesting point is that *S* shows a symmetric doping dependence while resistivity shows an asymmetry.

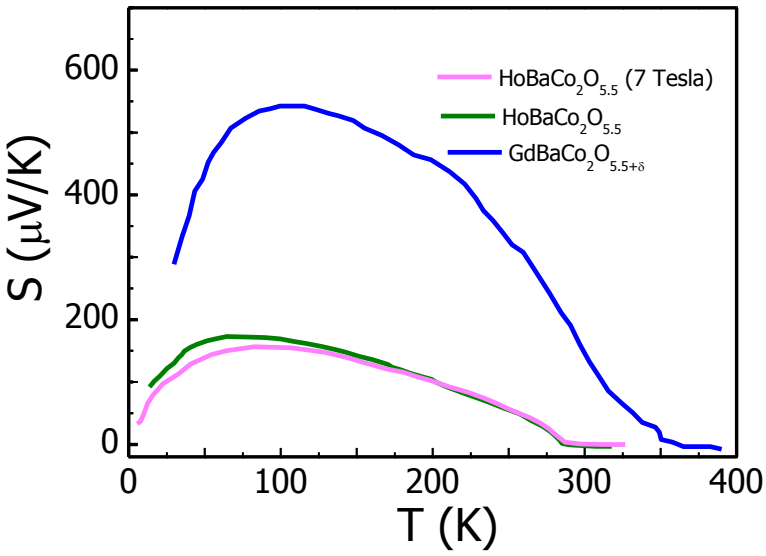

Figure 1.16 Temperature dependent Seebeck coefficients of HBCO and GBCO crystals. Seebeck coefficient of HBCO suppressed below 100 K under an applied 7 Tesla magnetic field. Data digitized from literature. [52]

Spin-Blockade effect

It will be interesting to compare *S* (*T*) of GBCO with HBCO crystal (depicted in Figure 1.16) as they have many common features. *S* is positive for stoichiometric $HoBaCo_2O_{5.5}$ crystal[68] which indicates holes as major carriers, while after metal insulator transition it is slightly negative. This observation suggests that there is competition between holes (Co^{+4}) and electrons (Co^{+2}) to dominate the conduction as a function of temperature. To explain the holes (Co^{+4}) conduction at low temperatures, a charge disproportionation reaction was described where there

was an equal number of Co^{+2} and Co^{+4} ($2Co^{+3} \leftrightarrow Co^{+2} + Co^{+4}$) due to thermal activation in the stoichiometric crystal. The hopping conduction of Co^{+2} ions are restricted due to unusual spin blockade phenomena (schematically illustrated in Figure 1.17) i.e. electrons of Co^{+2} ions are not allowed to hop in the background of low spin (LS) Co^{+3} due to unfavorable spin states. Therefore, conduction is dominated by hole transport At high temperatures ($T \geq 300K$) Co^{+3} in octahedral coordination acquire high spin (HS) states which allow Co^{+2} e_g the electrons to hop and electrons dominate the conduction. The *S* of stoichiometric $HoBaCo_2O_{5.5}$ crystal increases with decreasing temperature and passes through a maximum, as depicted in Figure 1.16.

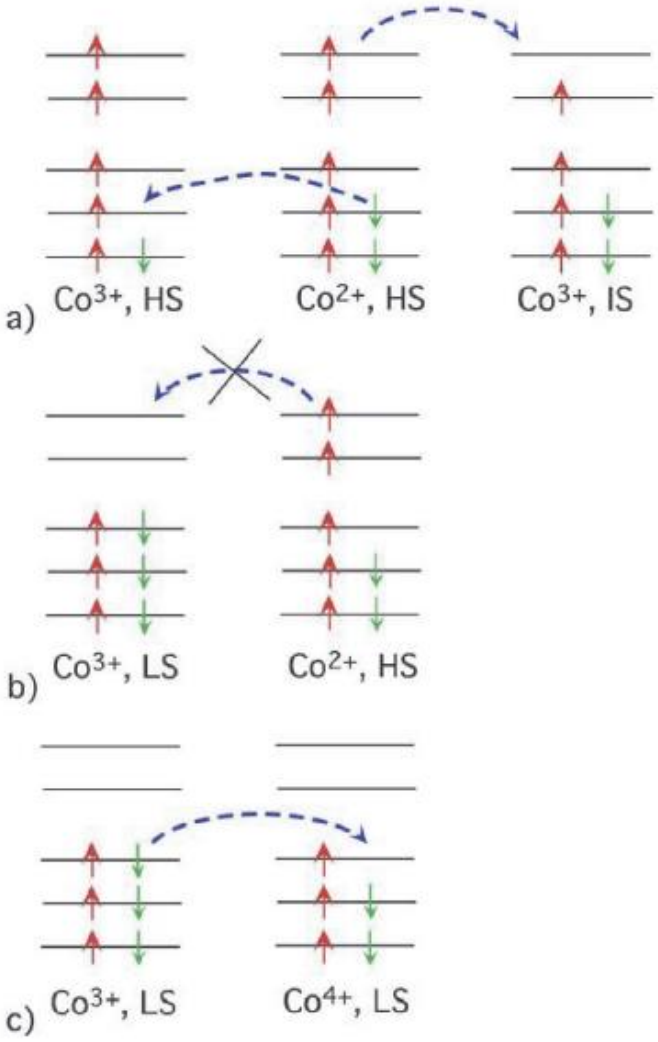

Figure 1.17 Schematic illustration of the spin-blockade phenomena observed in $HoBaCo_2O_{5.5}$ crystal, taken from[51] (a) Schematics of electron hopping (Co^{+2} ions) in the back ground of high spin (HS) and intermediate spin (IS) Co^{+3} ions, (b) restricted hopping of Co^{+2} ions in the background of LS Co^{+3} ions due to unfavorable spin states and, (c) hopping of Co^{+4} ions (holes) in the back ground of LS Co^{+3} ions. Graph is taken from Ref 51.

GBCO crystals have a similar trend of temperature dependent S, except that the S is larger in magnitude compared to HBCO below 300 K. But there are few more interesting features in the S of GBCO crystals as a function of temperature, which are not yet fully understood.

First, low temperature S of stoichiometric GBCO crystals show *n*-type conductivity (see Figure 1.15b) i.e. Co^{+2} can hop in the background of Co^{+3} (LS) while in HBCO, it is positive. Interestingly, a similar spin blockade effect was found to exhibit in the electron doped GBCO crystal.

- ❖ Therefore, the question is why stoichiometric GBCO crystals show *n*-type conductivity but not *p*-type as shown in HBCO crystals?

Secondly, the large S (and its doping dependence) at 100 K in GBCO crystals was thought to originate from the additional spin-orbital degeneracy contribution to Heike's formula. But, it is noteworthy that Heike's formula is only applicable when S is temperature independent. As can be seen from the measured S data in Figure 1.15b, S is strongly temperature dependent from 100 K down to 360 K.

- ❖ Therefore, the question is what is the true high temperature limit of S in case of GBCO?

Scope of experiment II

In chapter 4, we aimed to find out the true high temperature limit of S in the case of GBCO films grown on $SrTiO_3$ (001) substrates.

1.11 Why thin film?

Thin film deposition provides an opportunity to measure the effects of the following parameters in achieving and improving physical properties.

1. One of the main reasons for using epitaxial films is the fact that physical properties of layered compounds are generally anisotropic. The use of highly oriented films allows exploring physical phenomena taking place along particular crystallographic directions.
2. The growth of epitaxial films on mismatched substrates may induce the introduction of a certain mechanical strain (compressive or tensile depending on the substrate film mismatch) which induces changes in the crystal structure (bond length and angles), which in turn can modify the physical properties and even bring out unexpected physical properties.

Scope of experiment III

In chapter 5, our focus was to examine effect of the epitaxial strains on the thermoelectric properties of GBCO films grown on $SrTiO_3$ (001), $[LaAlO_3]_{0.3}[Sr_2TaAlO_6]_{0.7}$ (abbreviated as LSAT (001)) and $LaAlO_3$ (001) substrates.

1.12 Summary

In this chapter, the basic principles of thermoelectric effects and devices were described. Thermoelectric figure of merit needs to be high ($zT > 1$) in order to achieve maximum Carnot efficiency. Layered misfit cobaltates are promising *p*-type thermoelectric materials shows zT> 1. The discussion focused on the thermoelectric properties of misfit cobaltates and double perovskite layered cobaltates. The scientific problems, along with the scope of the experiments to address these questions were described.

- In chapter 2, the main techniques, used to perform the experiments, will be described.
- The experimental results will be presented from chapters 3 to 6. A summary of this thesis and a general discussion will be presented in chapter 7.

Bibliography

[1] J. R. Sootsman, D. Y. Chung, M. G. Kanatzidis, *Angew. Chemie - Int. Ed.* **2009**, *48*, 8616–8639.

[2] G. Tan, L. D. Zhao, M. G. Kanatzidis, *Chem. Rev.* **2016**, *116*, 12123–12149.

[3] D. Kraemer, B. Poudel, H. P. Feng, J. C. Caylor, B. Yu, X. Yan, Y. Ma, X. Wang, D. Wang, A. Muto, et al., *Nat. Mater.* **2011**, *10*, 532–538.

[4] G. J. Snyder, E. S. Toberer, *Nat. Mater.* **2008**, *7*, 105–114.

[5] D. M. Rowe, **1995**, CRC Handbook of thermoelectrics.

[6] Tutorial on thermoelectrics: https://www.youtube.com/watch?v=BAJvlwbxvFM

Nanohub: Series of lectures by Prof. S, Datta. *https://www.youtube.com/watch?v=Svf3VyvVXWw*

[7] S. Lundstrom, M. and Datta, *https://www.youtube.com/watch?v=Nilx8sfmEMo* **2015**.

[8] S. Datta, Lessons from Nanoelectronics, Lecture notes: *World Sci. Publ. Co.* **2012**.

[9] L. D. Hicks, M. S. Dresselhaus, *Phys. Rev. B* **1993**, *47*, 727–731.

[10] L. D. Hicks, M. S. Dresselhaus, *Phys. Rev. B* **1993**, *47*, 16631.

[11] L. D. Hicks, T. C. Harman, X. Sun, M. S. Dresselhaus, *Phys. Rev. B* **1996**, *53*, R10493–R10496.

[12] G. S. Nolas, J. L. Cohn, G. A. Slack, S. B. Schujman, *Appl. Phys. Lett.* **1998**, *73*, 178–180.

[13] S. Bhattacharya, A. L. Pope, R. T. Littleton, T. M. Tritt, V. Ponnambalam, Y. Xia, S. J. Poon, *Appl. Phys. Lett.* **2000**, *77*, 2476–2478.

[14] T. Caillat, J.-P. Fleurial, A. Borshchevsky, *J. Phys. Chem. Solids* **1997**, *58*, 1119–1125.

[15] S. R. Brown, S. M. Kauzlarich, F. Gascoin, G. Jeffrey Snyder, *Chem. Mater.* **2006**, *18*, 1873–1877.

[16] I. Terasaki, Y. Sasago, K. Uchinokura, *Phys. Rev. B* **1997**, *56*, R12685–R12687.

[17] R. Funahashi, I. Matsubara, *Appl. Phys. Lett.* **2001**, *79*, 362–364.

[18] D. A. WRIGHT, *Nat. Mater.* **1958**, *181*, 834–834.

[19] H. Beyer, J. Nurnus, H. B. Ottner, A. Lambrecht, E. Wagner, G. Bauer, *Phys. E* **2002**, *13*, 965–968.

[20] K. Biswas, J. He, I. D. Blum, C.-I. Wu, T. P. Hogan, D. N. Seidman, V. P. Dravid, M. G. Kanatzidis, *Nature* **2012**, *489*, 414–8.

[21] K. Koumoto, I. Terasaki, *MRS Bull.* **2006**, *31*, 206–210.

[22] A. A. Taskin, A. N. Lavrov, Y. Ando, *Phys. Rev. B - Condens. Matter Mater. Phys.* **2005**, *71*, 1–28.

[23] P. Lemmens, V. Gnezdilov, N. N. Kovaleva, K. Y. Choi, H. Sakurai, E. Takayama-Muromachi, K. Takada, T. Sasaki, F. C. Chou, D. P. Chen, et al., *J. Phys. Condens. Matter* **2004**, *16*, DOI 10.1088/0953-8984/16/11/041.

[24] A. Satake, H. Tanaka, T. Ohkawa, T. Fujii, I. Terasaki, *J. Appl. Phys.* **2004**, *96*, 931–933.

[25] Y. Wang, N. S. Rogado, R. J. Cava, N. P. Ong, *Nature* **2003**, *423*, 425–428.

[26] D. J. Singh, D. Kasinathan, *J. Electron. Mater.* **2007**, *36*, 736–739.

[27] D. J. Singh, *Phys. Rev. B* **2000**, *61*, 397–402.

[28] H. J. Xiang, D. J. Singh, *Phys. Rev. B* **2007**, *76*, 195111.

[29] S. Kuno, T. Takeuchi, H. Ikuta, T. Kondo, A. Kaminski, Y. Saito, S. Fujimori, S. Radiation,

E. Agency, *IEEE Int. Conf. Thermoelectr.* **2007**, *2*, 99.

[30] T. Takeuchi, T. Kondo, T. Takami, H. Takahashi, H. Ikuta, U. Mizutani, K. Soda, R. Funahashi, M. Shikano, M. Mikami, S. Tsuda, T. Yokoya, S. Shin, T. Muro, *Phys. Rev. B* **2004**, *69*, 125410.

[31] K. Kuroki, R. Arita, *J. Phys. Soc. Japan* **2007**, *76*, 3–6.

[32] K. Fujita, T. Mochida, K. Nakamura, *Jpn. J. Appl. Phys.* **2001**, *40*, 4644–4647.

[33] R. Funahashi, I. Matsubara, H. Ikuta, T. Takeuchi, U. Mizutani, S. Sodeoka, *Jpn. J. Appl. Phys.* **2000**, *39*, L1127–L1129.

[34] J. Rouxel, A. Meerschaut, G. A. Wiegers, *J. Alloys Compd.* **1995**, *229*, 144–157.

[35] H. Yamauchi, K. Sakai, T. Nagai, Y. Matsui, M. Karppinen, *Chem. Mater.* **2006**, *18*, 155–158.

[36] A. M. W. Kobayashi, S. Hébert, H. Muguerra, D. Grebille, D. Pelloquin, *IEEE Int. Conf. Thermoelectr.* **2007**, *2*, 117.

[37] P. Boullay, R. Seshadri, F. Studer, M. Hervieu, D. Groult, B. Raveau, *Chem. Mater.* **1998**, *10*, 92–102.

[38] D. Pelloquin, A. Maignan, S. Hébert, C. Martin, M. Hervieu, C. Michel, L. B. Wang, B. Raveau, *Chem. Mater.* **2002**, *14*, 3100–3105.

[39] R. Tian, R. Donelson, C. D. Ling, P. E. R. Blanchard, T. Zhang, D. Chu, T. T. Tan, S. Li, *J. Phys. Chem. C* **2013**, *117*, 13382–13387.

[40] Y. Huang, B. Zhao, S. Lin, Y. Sun, *J. Phys. Chem. C* **2015**, *119*, 7979–7986.

[41] N. Créon, O. Ferez, J. Hadermann, Y. Klein, S. Hébert, M. Hervieu, B. Raveau, *Chem. Mater.* **2006**, *18*, 5355–5362.

[42] M. Schrade, H. Fjeld, T. G. Finstad, T. Norby, *J. Phys. Chem. C* **2014**, *118*, 2908–2918.

[43] M. Schrade, S. Casolo, P. J. Graham, C. Ulrich, S. Li, O-M. Løvvik, T. G. Finstad, T. Norby, *J. Phys. Chem. C* **2014**, *118*, 18899–18907.

[44] P. Limelette, V. Hardy, D. Jérome, D. Flahaut, S. Hébert, R. Frésard, C. Simon, *Phys. Rev. B* **2005**, *71*, 233108.

[45] I. Terasaki, *J. Appl. Phys.* **2011**, *110*, 53705.

[46] P. M. Chaikin and G.Beni, *Phys. Rev. B* **1976**, *13*, 647.

[47] A. Nag, V. Shubha, *J. Electron. Mater.* **2014**, *43*, 962–977.

[48] P. L. Bach, V. Leborán, E. Ferreiro-vila, B. Rodríguez-gonzález, *APL Mater.* **2013**, *1*, 21101.

[49] M. Pollet, J. P. Doumerc, E. Guilmeau, D. Grebille, J. F. Fagnard, R. Cloots, *J. Appl. Phys.* **2007**, *101*, 83708.

[50] T. Yamamoto, I. T. Uchinokura, K, *Phys. Rev. B* **2002**, *65*, 184434.

[51] V. Brouet, A. Nicolaou, M. Zacchigna, A. Tejeda, L. Patthey, S. Hébert, W. Kobayashi, H. Muguerra, D. Grebille, *Phys. Rev. B - Condens. Matter Mater. Phys.* **2007**, *76*, 100403.

[52] J. Bobroff, S. Hébert, G. Lang, P. Mendels, D. Pelloquin, A. Maignan, *Phys. Rev. B* **2007**, *76*, 100407.

[53] W. Koshibae, S. Maekawa, *Phys. Rev. Lett.* **2001**, *87*, 236603.

[54] W. Koshibae, K. Tsutsui, S. Maekawa, *Phys. Rev. B* **2000**, *62*, 6869–6872.

[55] T. D. Sparks, *Oxide Thermoelectr. Role Cryst. Struct. Thermopower Strongly Correl. Spinels* **2014**, *PhD Thesis*.

[56] Y. Huang, B. Zhao, R. Ang, S. Lin, Z. Huang, S. Tan, Y. Liu, W. Song, Y. Sun, *J. Phys. Chem. C* **2013**, *117*, 11459–11470.

[57] R. F. Klie, Q. Qiao, T. Paulauskas, A. Gulec, A. Rebola, S. O¨u¨ g¨t, M.P. Prange, J. C. Idrobo, S.T. Pantelides, S. Kolesnik, B. Dabrowski, M. Ozdemir, C. Boyraz, D. Mazumdar, A. Gupta, *Phys. Rev. Lett.* **2012**, *108*, 196601.

[58] Z. Li, C. Xiao, H. Zhu, Y. Xie, *J. Am. Chem. Soc.* **2016**, *138*, 14810–14819.

[59] Q. Wen, C. Chang, L. Pan, X. Li, T. Yang, H. Guo, Z. Wang, J. Zhang, F. Xu, Z. Zhang, et al., *J. Mater. Chem. A* **2017**, *5*, 13392–13399.

[60] I. Terasaki, *APL Mater.* **2016**, *4*, DOI 10.1063/1.4954227.

[61] B. Rivas-Murias, J. Manuel Vila-Fungueiriño, F. Rivadulla, *Sci. Rep.* **2015**, *5*, 11889.

[62] C. Bernuy-Lopez, K. Høydalsvik, M. A. Einarsrud, T. Grande, *Materials (Basel).* **2016**, *9*, DOI 10.3390/ma9030154.

[63] A. Grimaud, K. J. May, C. E. Carlton, Y.-L. Lee, M. Risch, W. T. Hong, J. Zhou, Y. Shao-Horn, *Nat. Commun.* **2013**, *4*, 1–7.

[64] C. Frontera, J. L. García-Muñoz, A. Llobet, M. A. G. Aranda, *Phys. Rev. B* **2002**, *65*, 180405.

[65] A. A. Taskin, A. N. Lavrov, Y. Ando, *Phys. Rev. Lett.* **2003**, *90*, 227201.

[66] A. A. Taskin, A. N. Lavrov, Y. Ando, *Phys. Rev. B* **2006**, *73*, 121101.

[67] V. Pardo, D. Baldomir, *Phys. Rev. B* **2006**, *73*, 165117.

[68] A. Maignan, V. Caignaert, B. Raveau, D. Khomskii, G. Sawatzky, *Phys. Rev. Lett.* **2004**, *93*, 26401–1.

Chapter 2: Experimental methods

A brief overview of the main techniques used to grow thin films, their structural characterization and the measurement of physical properties is presented in this chapter.

2.1 Introduction

This chapter provides a general overview of the principles of the methods employed to carry out the growth of the films, their structural characterization, nanoscale characterization, electronic and thermoelectric transport property measurements.

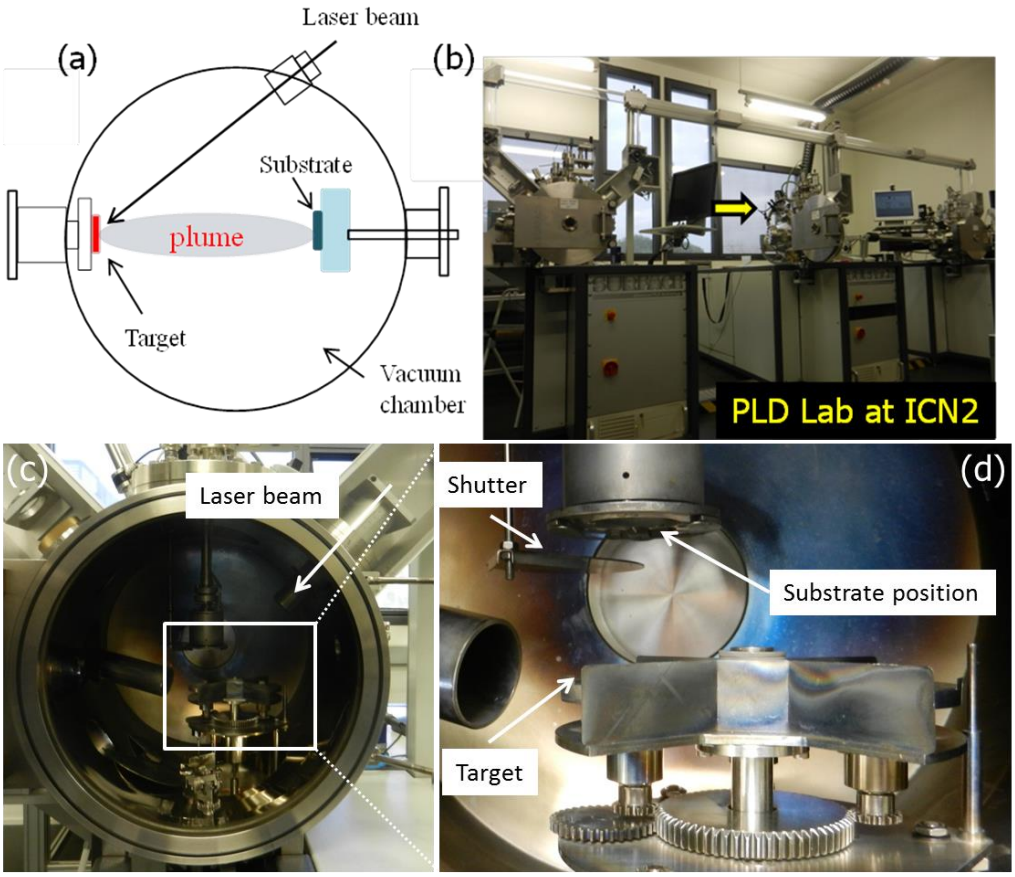

Figure 2.1 Schematic illustrations of thin film deposition by PLD technique: (a) Sketch of the PLD chamber, (b) PLD work station at ICN2 (arrow indicates the chamber where we have grown the films), (c) closer look of the PLD chamber and, (d) actual image of the target position, substrate position and the window from where laser is focused to the solid target.

2.2 Pulsed laser deposition (PLD)

PLD is one of the most widely used techniques to grow thin films. One of the major advantages of this technique is the congruent transfer of the composition from target to substrate. Thin films of metal oxides were grown by pulsed laser deposition (PLD) method in a PLD-workstation, manufactured at ICN2 by SURFACE systems + technology GmbH & Co

(using a Lambda Physic Compex 201 KrF pulsed excimer laser, with a wavelength of 248 nm, energy up to 700 mJ per pulse and a repetition rate of 1 to 10 Hz). The working principles of the PLD technique are presented schematically in Figure 2.1a. An UV-excimer emitting high energy laser pulses (pulse duration 20 ns) is focused through a lens into an entrance window of the PLD chamber (kept in a vacuum) on the solid target, typically a high density ceramic pellet of the same composition as the films one intends to grow. The energy absorbed by the small volume of target surface is enough to evaporate the high melting temperature of oxide materials. Immediately after laser illumination, a high pressure gas (containing ions, atoms, molecules etc.) is produced within that small volume. Due to the pressure gradient, a supersonic jet of the atoms is ejected normal to the surface of the target. By absorbing energy density from the laser beams, the hot plasma propagates towards the surface of the substrate. In this study, the distance between substrate and target was kept at 55 mm for all film deposition experiments. Variable oxygen pressure (from 50 mTorr to 600 mTorr) was used to stabilize crystallinity and for controlling the oxygen stoichiometry of our films. One of the important advantages of PLD technology is congruent transfer of compositions.

2.3 Structural characterization

We used X-ray related techniques such as X-ray diffraction (XRD), X-ray reflectivity (XRR) and, X-ray reciprocal space maps (RSMs) to determine the crystalline phase, thickness, and interface between films grown on single crystal perovskite substrates. Detailed nanoscale characterization was performed by transmission electron microscopy techniques (TEM) and scanning transmission electron microscopy (STEM).

2.3.1 Standard X-ray diffraction

X-ray diffraction is one of the most important and widely used tools to characterize crystalline materials. When X-rays interact with the crystalline lattice, secondary diffracted beams are generated. W. H. Bragg and W. L. Bragg explained X-ray diffraction by modelling the crystals as a set of parallel planes spaced at a distance d_{hkl} (Figure 2.2). A diffraction peak is produced when there is a coherent interference between the diffracted waves of different planes. The condition in which the scattered waves interfere coherently is known as the Bragg's Law:

$$n\lambda = 2d_{hkl}sin\theta \qquad (2.1)$$

where, d_{hkl} is the inter-planar spacing with Miller indexes (hkl), θ is the angular peak position, n is an integer and λ is the wavelength. X'Pert PANnalytical Pro MRD diffractometer at ICN2 has been extensively used to characterize the thin films. It is a four-angle goniometer of high precision together with X-ray optics (parabolic mirror and the monochromator) that enable high resolution setups for different analyses. As an examples, the standard diffraction patterns obtained for the $GdBaCo_2O_{5.5+\delta}$ (GBCO) films grown on $SrTiO_3$ (001) and $NdGaO_3$ (110) substrates are depicted in Figure 2.3.

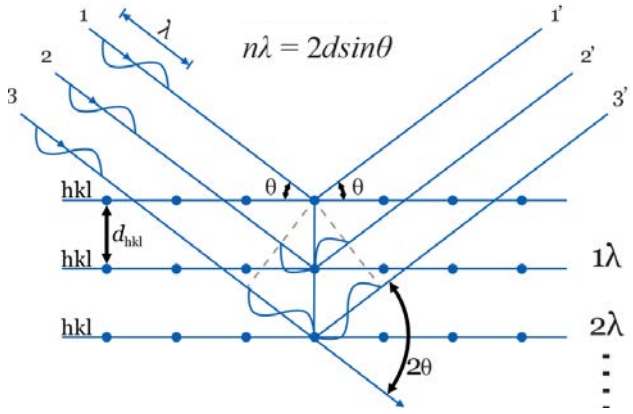

Figure 2.2 Schematics illustrates the diffraction of X-ray by atomic planes.

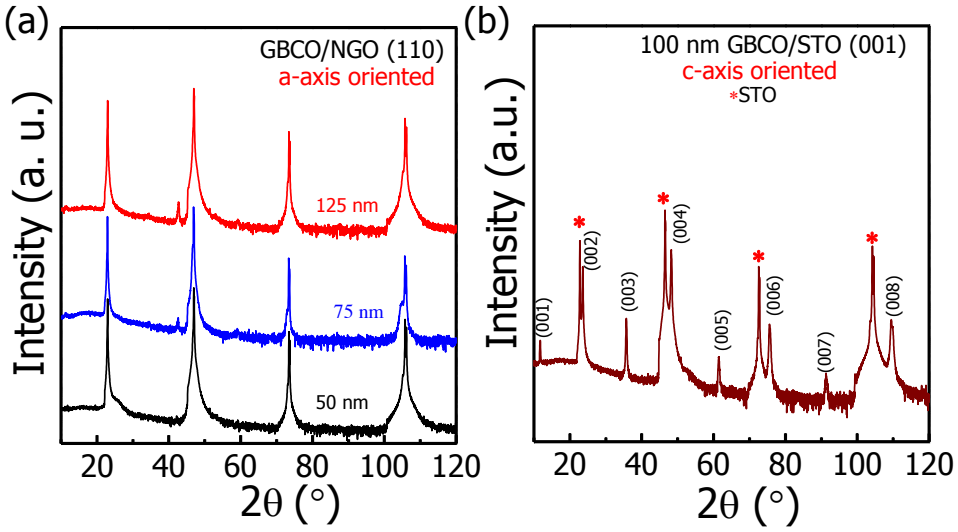

Figure 2.3 X-ray diffraction patterns of GBCO films. Standard 2θ/ω patterns of (a) GBCO/NGO (110), a-axis oriented films and, (b) GBCO/STO (001); c-axis oriented film.

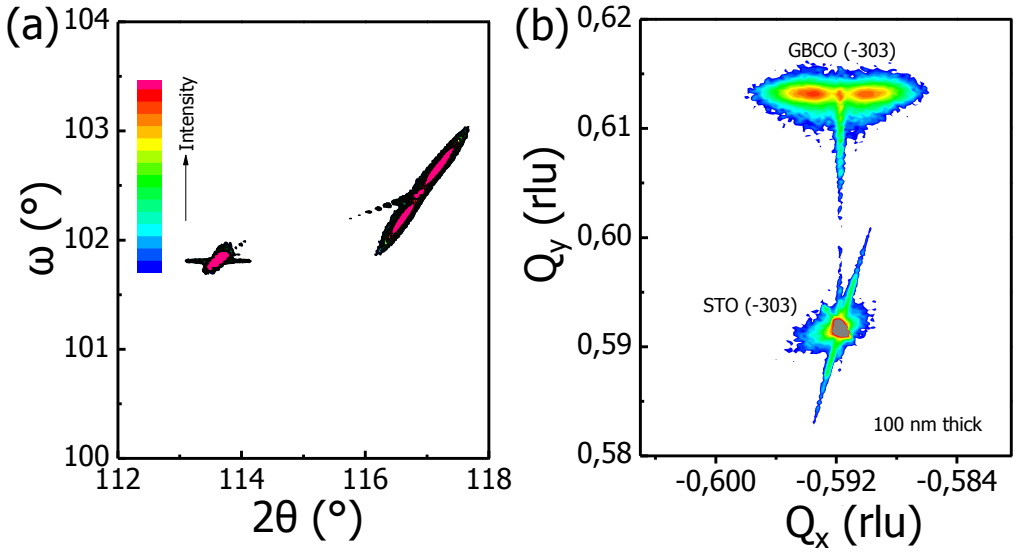

Figure 2.4 RSM of GBCO film. (a) Combined 2θ and ω scan around (-303) reflection and, (b) RSM around (-303) of STO in GBCO/STO (001).

2.3.2 Reciprocal space maps (RSMs)

Reciprocal space lattice is an alternative description of the real lattice. It shows the same symmetry as the direct crystal. In the case of the epitaxial layer, the relative positions of the atomic planes can easily be seen in the reciprocal space. In this experiment, an intense asymmetric family of planes was chosen to determine the in-plane and out-of-plane lattice parameters of the epitaxial layer. Asymmetric means that the angle omega is not equal to 2theta/2 ($\omega \neq 2\theta/2$). In this way, the position in the reciprocal space that can be determined by an accurate scan i.e., a combined scan of 2 theta and omega provides information about the in-plane and out-of-plane components of the cell parameters. The goniometer was positioned to the asymmetric reflection in order to obtain the maximum intensity by optimizing 2θ and ω. Hybrid monochromator (combined with parabolic mirror and a 2-Ge channel cut crystal) was used for the wavelength filtering. This area scan involved the 2θ-ω measurement over 14° range of the selected asymmetric reflections by tilting the angle ω over a certain range (±3°). This resulted in a ω vs 2θ map where the substrate peak is found in the center of the map and the thin film's peak has a relative position to the origin depending on its d_{hkl}-spacing in relation to the substrate's, as depicted in Figure 2.4 for GBCO film grown on STO (001) . The surface vector of an asymmetric plane has in-plane and out-of-plane component. In the reciprocal space, Q_x and Q_y are reciprocal space coordinates expressed in reciprocal lattice units (r.l.u.) corresponding to the

in-plane and out-of-plane directions respectively. This is the why converting the ω vs 2θ map into a reciprocal space map is a useful and visual way to study the epitaxial growth of thin films.

Furthermore, from Q_x and Q_y positions of a (*h* 0 *l*) peak [for simplicity, one may pick (*h k l*) reflections with k = 0], the in-plane (a) and the out-of-plane (c) cell parameters can be easily calculated by the using equations 2.2 and 2.3. However, before performing any calculation, it is important to determine an offset correction. The substrate peak position may serve as a reference to correct for any offset produced typically by a sample misalignment in the experimental omega value. These Q's are expressed in r.l.u. (reciprocal lattice units); very commonly used by Panalytical. However, a more consistent representation is using a factor, $Q_x = \frac{4\pi}{\lambda} \times sin\theta \sin(\theta - \omega)$ and $Q_y = \frac{4\pi}{\lambda} \times sin\theta \cos(\theta - \omega)$ have $Å^{-1}$ unit.

$$a = \frac{h.\lambda_{Cu}}{2Q_x} \qquad (2.2)$$

$$c = \frac{l.\lambda_{Cu}}{2Q_y} \qquad (2.3)$$

2.3.3 X-ray reflectivity (XRR)

XRR measurements were performed by measuring the intensity of reflected X-rays by a film at grazing angle maintaining the condition ω = 2θ/2. It is measured in standard 2θ-ω coupled scan where the incident angle, ω, is half of diffraction angle 2θ. The X-ray reflection at the interface occurs because of the different electron density of electrons in different layers. The penetration depth of an X-ray is a few nanometers in the film when the incident angle is below the critical angle (θ_c) and above the critical angle, penetration depth increases sharply. One part of the X-ray incident beam is reflected where the electron density changes and it is possible to detect the interference of X-rays scattered at the interfaces and thus thickness fringes can be observed as depicted in Figure 2.5. The minima and the maxima of the fringes correspond to the destructive interference and constructive interference respectively. The periods in the fringes are related to the thickness and the intensity fall is related to the roughness of the film. The thickness of the film can be measured from the maxima or the minima of the fringes using Fresnel's model. We have used the Reflectivity software from Panalytical which offers different ways to analyse film thicknesses (either simplified minima-maxima separation, full scan Fourier transformation or full profile fitting).

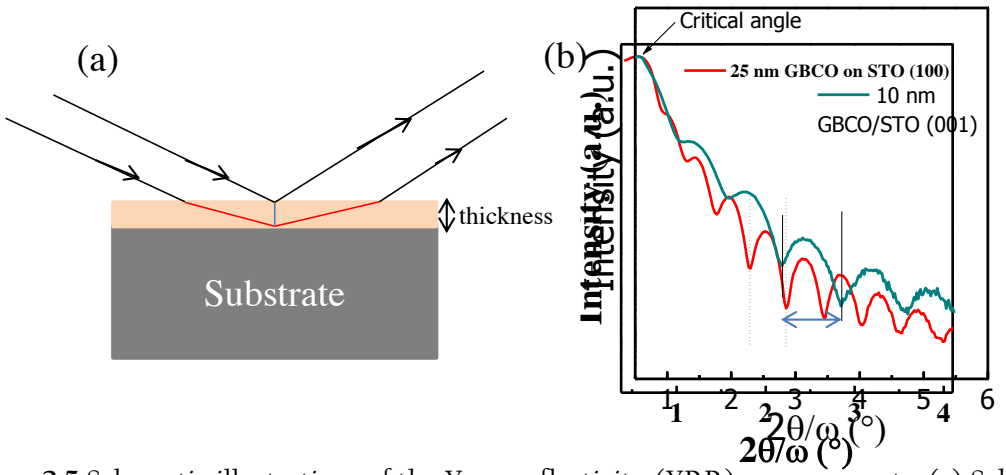

Figure 2.5 Schematic illustrations of the X-ray reflectivity (XRR) measurements. (a) Schematics of the X-ray reflectivity and (b) measured XRR of 25 nm GBCO film grown on $SrTiO_3$ (001) substrate.

2.4 Surface characterization

Surface of the thin films were characterized by two different techniques; X-ray photoelectron spectroscopy and the scanning electron microscopy.

2.4.1 X-ray photoelectron spectroscopy (XPS)

XPS is a surface sensitive spectroscopic technique often used as a probe to detect chemical composition as well as electronic structure. It is based on the photoelectric effect described by Einstein in 1905. It works by irradiating a material with X-ray beams and then quantifies the kinetic energy and number of the photo-electrons that are emitted from a material. It provides information about the nature of chemical bonds. The key advantages of this technique are that it is surface sensitive, non-destructive and also provides quantitative information. The energy of the incident X-rays is absorbed by the atoms and the inner shell electrons are ejected as demonstrated in Figure 2.6. The difference between incident and the emitted energy corresponds to the binding energy. Kinetic energy of the emitted electrons can be calculated from the following equation:

$$E_{binding} = E_{photon} - (E_{kinetic} + \varphi) \qquad (2.4)$$

where φ, the work function, is the minimum energy required to eject an electron from the surface of the material to immediately outside in a vacuum. The kinetic energy of the ejected electron is unique for each element. Thus, it is possible to quantify the composition of the elements present

in the materials. $E_{binding}$ represents the binding energy of electrons and E_{photon} represents incident X-ray energy.

An example of an XPS spectrum is shown in Figure 2.6. It contains the full XPS spectrum obtained for $Ca_3Co_4O_9$ ceramics.

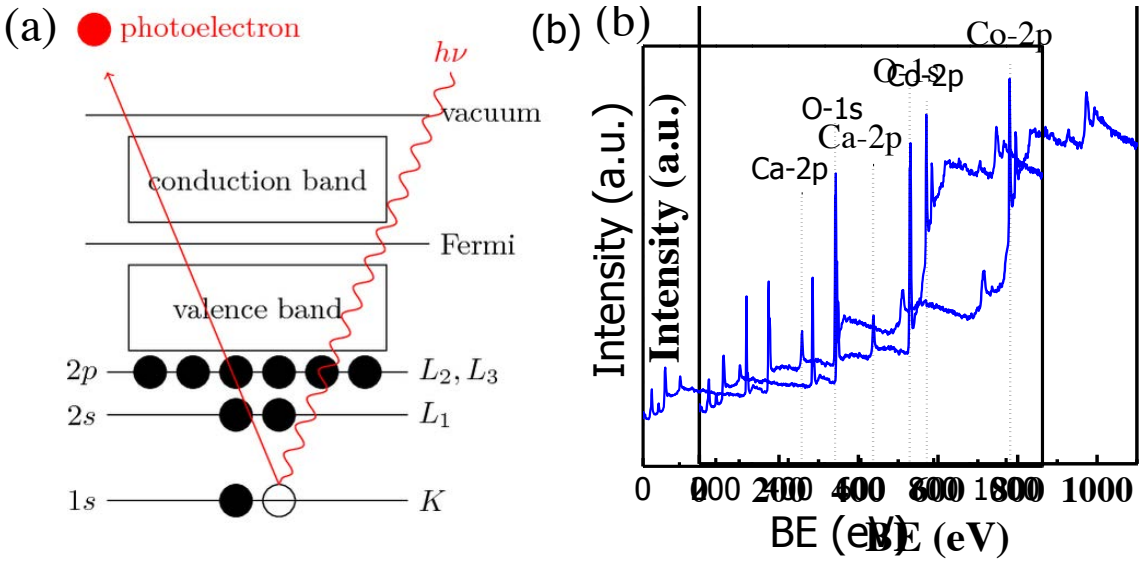

Figure 2.6 Schematic illustrations of the X-ray photoelectron spectroscopy (XPS) measurements. (a) Energy diagram and, (b) measured overall XPS spectrum of $Ca_3Co_4O_9$ ceramics.

2.4.2 Scanning Electron microscopy

SEM is a very surface sensitive technique. In SEM, a high energy electron beam is focused on the sample surface to generate various signals. The generated signals include, characteristic X-ray (used to quantify elemental composition), back scattered electrons and, secondary electrons. Secondary electrons are useful for forming an image of the topography and surface morphology. Backscattered electrons are useful for illustrating the contrast between elements of different atomic weight. Images of the surface of GBCO films grown on STO (001) substrates are shown in Chapter 4.

2.5 Nanoscale characterization

Nanoscale characterization of the GBCO films was carried out by transmission electron microscopy and scanning-TEM.

2.5.1 Transmission electron microscopy (TEM)

Transmission electron microscopy (TEM) uses a beam of electrons exploiting the wave nature of electrons. It consists of an electron emission source, electromagnetic lenses and an

electron detector. A very thin sample is positioned along the electron beam. The electron beam is produced, accelerates and is then forced to transmit through the sample. The beam modifies it and imprints its image. The beam is then magnified by other lenses and detected by a fluorescence screen or by a charged-coupled device (CCD). TEM allows the magnifying of images of very thin samples down to atomic resolution. When the electron beam passes through the sample, it scatters. If the sample is crystalline, then electrons form a diffraction pattern. Thus crystalline structure can be determined from electron diffraction.

An example of the high resolution cross-section of a TEM image and an electron diffraction pattern of GBCO film grown on LSAT (001) substrate is depicted in Figure 2.7. Details of the nanoscale characterization of GBCO films grown on different substrates will be discussed in chapters 5 and 6.

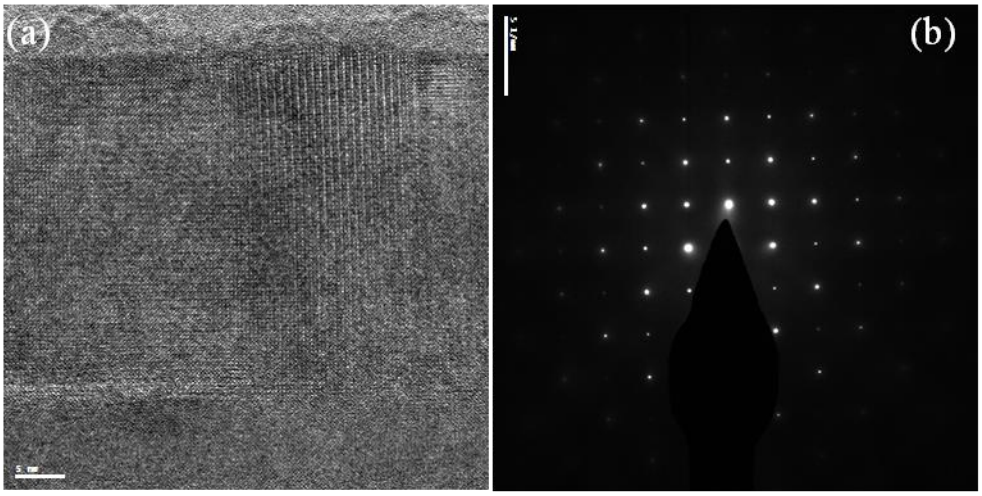

Figure 2.7 TEM images of GBCO film grown on $LaSrTaAlO_3$ (LSAT) substrate; (a) Cross section high resolution TEM image and, (b) Selected area electron diffraction pattern.

2.5.2 Scanning transmission electron microscopy (STEM)

Scanning-TEM is a type of TEM. It works in a similar way to SEM. An electron beam is focused onto a narrow spot and then it is scanned over the sample. As the electrons pass through the sample, the collected intensities can be used to produce transmission images depending on the sample local absorption. At the same time, characteristics X-rays and backscattered electrons are produced. STEM combined with high angle annular dark field detection (HAADF) produces high resolution images where the contrast is directly related to the atomic number of elements (proportional to $Z^{1.5}$), and therefore it is very useful to detect the formation of different phases and inter-diffusion between film and substrate.

An example of the STEM-HAADF image of GBCO film grown on STO (001) substrate is depicted in Figure 2.8. Details of the STEM-HAADF images will be discussed in chapter 5.

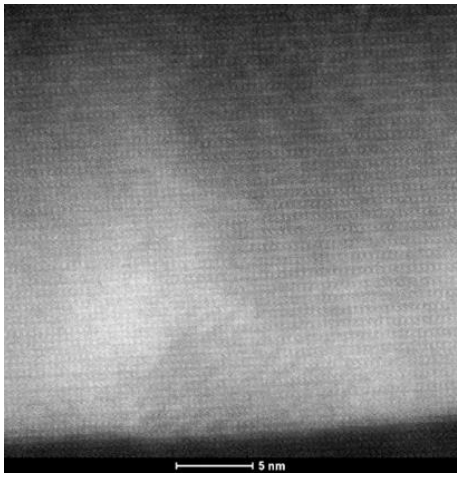

Figure 2.8 HAADF-STEM image of GBCO film grown on $SrTiO_3$ (001) substrate.

2.6 Measurement of transport properties

In this section, electronic and thermoelectric transport property measurement techniques are described.

2.6.1 Seebeck effect measurements

In order to perform Seebeck effect measurements of our film, a temperature gradient has to be induced and accurately controlled. For this, one Pt heater and two Pt resistors were deposited by optical lithography (shown in Figure 2.9). The heater was electrically isolated from the film surface. These two resistors (T1 and T2) acted as thermometers. Pt resistors were calibrated at a very slow cooling rate (0.2K/min) by measuring 4-point resistance as a function of base temperature (Figure 2.9b). Base temperature was overall temperature of the sample holder (where sample holder was in contact with the heating plate). Resistance at a particular base temperature was assigned to measure actual temperature during Seebeck measurements.

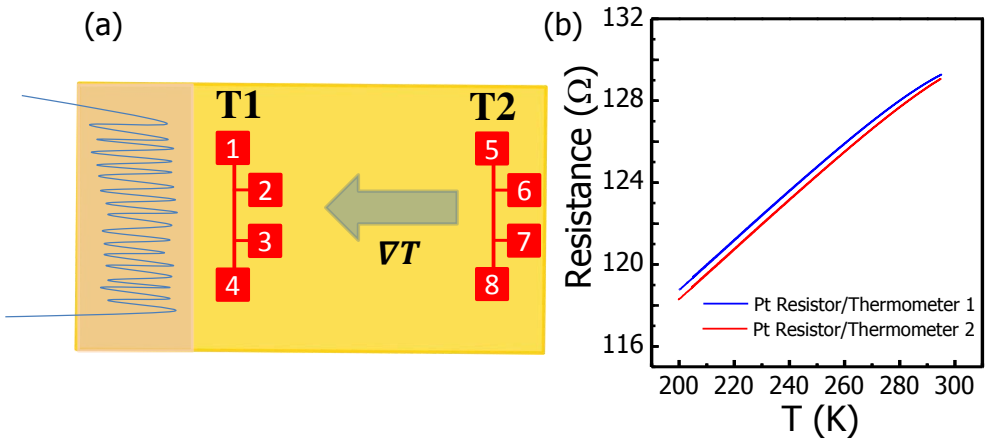

Figure 2.9 Schematics of the Seebeck effect measurements: (a) Sketch of the set up used (top view). Two Pt resistors (acts as thermometer) and a Pt heater were fabricated. (b) Calibration of the Pt resistors; resistance as function of base temperature.

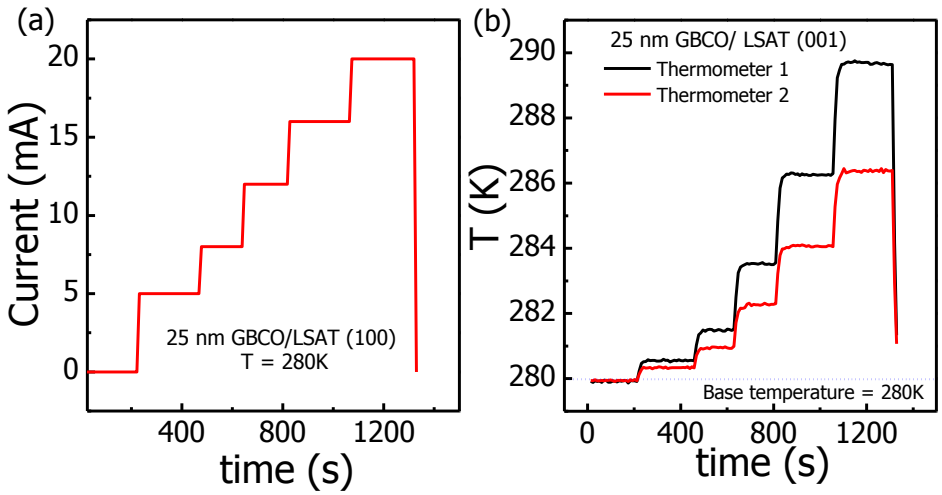

Figure 2.10 Stabilization of temperature gradient for Seebeck effect measurement. (a) Power applied to the heater and, (b) stabilized temperature gradients.

By varying the current to the heater, a series of temperature gradients were created in the sample (Figure 2.10) and at the same time Seebeck voltages were collected (Figure 2.11). Temperature gradient, ΔT, and Seebeck voltage are proportional to the applied power which proves its thermoelectric origin (depicted in Figure 2.12).

The sign of the Seebeck coefficient is determined from the relation given by equation 2.5. Thus, if *S* is positive, the voltage collected at the hot end should be less than at the cold side and

vice versa for negative S. S was calculated from the slope of $V_{Seebeck}$ (or −ΔV) vs ΔT curve (Figure 3.14).

$$S = -\frac{V_{Hot} - V_{Cold}}{T_{Hot} - T_{Cold}} = \frac{-\Delta V}{\Delta T} = \frac{V_{Seebeck}}{\Delta T} \qquad (2.5)$$

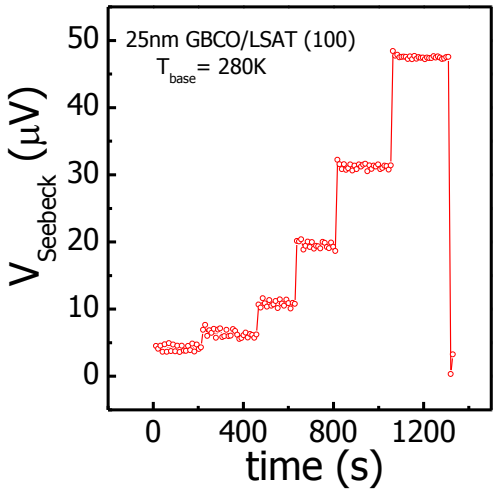

Figure 2.11 Seebeck voltage measured when a series of temperature gradients were stabilized at a fixed base temperature.

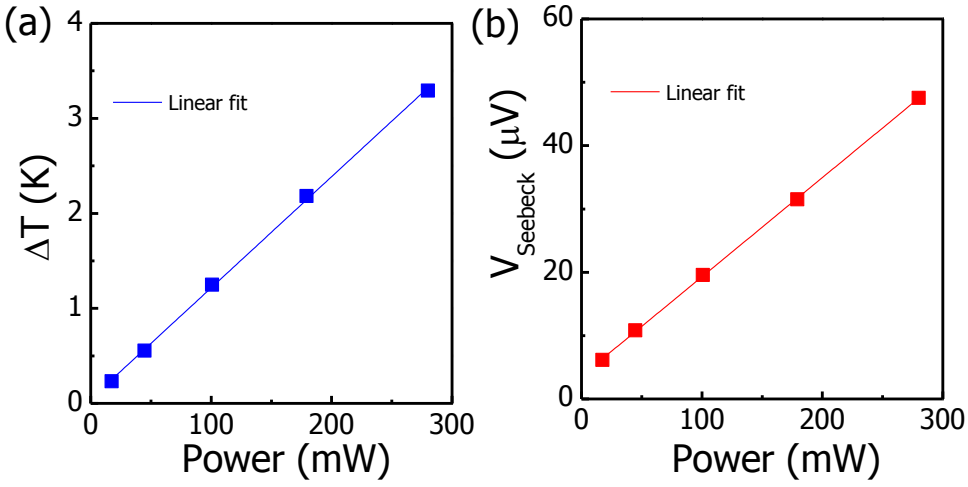

Figure 2.12 Temperature gradient and Seebeck voltage is proportional to the applied power. This is the evidence of the thermoelectric origin of the measured voltages.

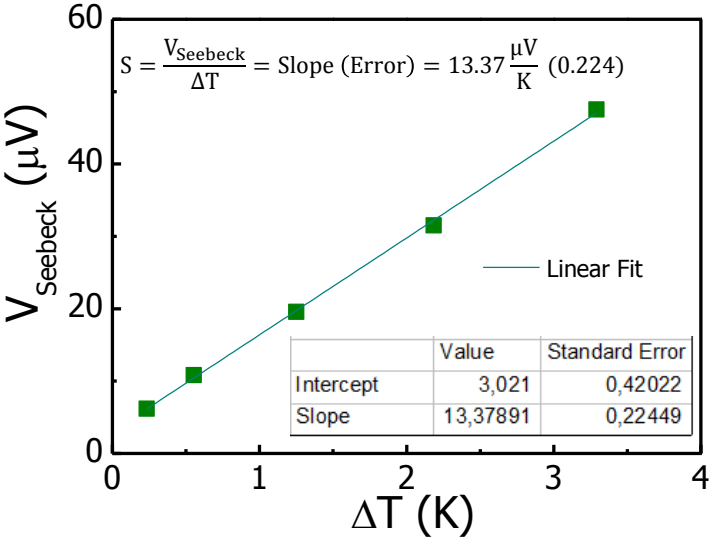

Figure 2.13 Seebeck coefficient (S) was calculated from the slope of the $V_{Seebeck}$ (or $-\Delta V$) vs ΔT curve. S depends only on the slope but not on the intercept.

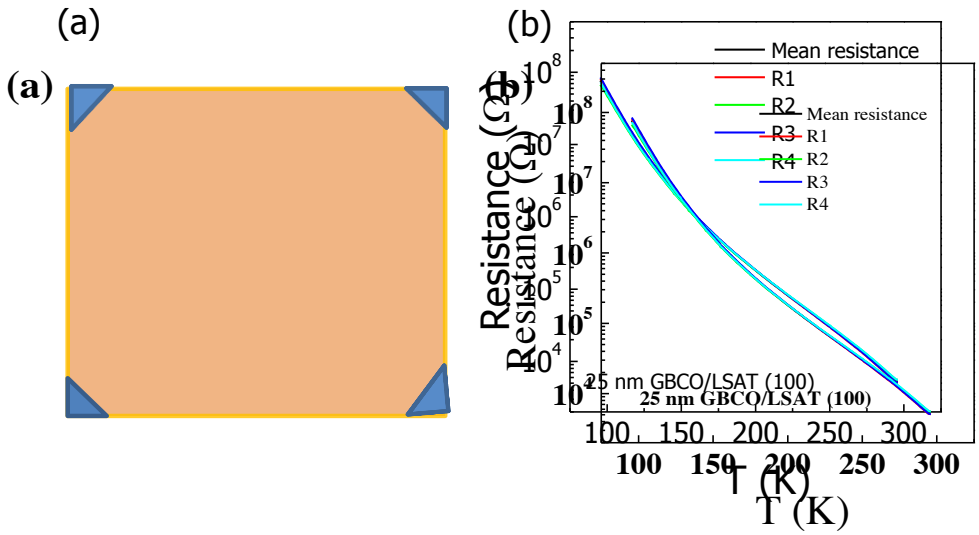

Figure 2.14 Measurement of resistance by van der Pauw method. (a) Schematic illustration of the geometry used for resistance measurement and, (b) measured resistance of 25 nm GBCO film grown on LSAT (001) substrate from 300 K to 80 K.

2.6.2 Electrical resistance measurements

Electrical resistance of the thin films was measured by the Van der Pauw method. Pt metal was deposited by electron-beam deposition at the four corners of the 5×5 mm^2 film surface. Figure 2.14 shows the measured resistance of the 25 nm GBCO film grown on LSAT (001) substrate. R1, R2, R3 and R4 are the temperature dependent resistance of GBCO films

when injection of the current (and collected voltage) was rotated in a 90° angle each time to check the homogeneity. The coincidence of all measured R i.e., the mean resistance is an indication of sample homogeneity and low resistance Pt contacts. The mean resistance was taken to calculate the resistivity of the films from the following equation.

$$\rho_{film} = \frac{\pi.(film\ thickness).(mean\ resistance)}{\ln(2)} \qquad (2.6)$$

2.6.3 Hall effect measurements

Hall effect measurements were performed by the Van der Pauw method. Transverse Hall voltages were collected when magnetic was applied perpendicular to the surface of film. Electron density was calculated from the following relation; $R_H = -1/n.e$, where, R_H is the Hall resistance, e is elementary charge of electron and *n* is the density of carriers.

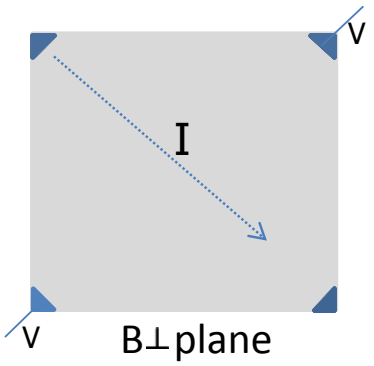

Figure 2.15 Schematic illustration of the geometry for Hall measurement.

Chapter 3: Thermoelectric properties of misfit cobaltate $[Bi_2Sr_2O_{4-\delta}]^{RS}[CoO_2]_q$ thin films

Thermopower of $[Bi_2Sr_2O_{4-\delta}]^{RS}[CoO_2]_q$ misfit cobaltate is temperature independent from ~200 to 300 K. Therefore, it is considered to be the high temperature limit and it can be expressed by Heike's formula. Some authors have claimed that in addition to the Heike's formula, entropy related to spin-orbit degeneracy contributes to thermopower at its high temperature limit. Other authors have claimed that thermopower at 300 K can be understood without the spin-orbit degeneracy factor.

This chapter therefore, focused on the role of spin-orbit degeneracy to explain the thermopower of our films at 300 K.

3.1 Introduction

The discovery of large thermopower (*S*~100 μV/K at 300 K) with metallic conductivity (~5000 S/cm at 300 K) in $NaCo_2O_4$ crystal has attracted a great deal of attention from the thermoelectric community.[1] Closely related layered misfit cobaltates, such as $Bi_2Sr_2Co_2O_y$ (BSCO),[2] $Ca_3Co_4O_9$ (CCO),[3] were found to exhibit large S (100-150 μV/K) at 300 K and metallic electrical conductivity (resistivity < 10mΩcm). These cobaltates are characterized by two dimensional triangular CoO_2 lattice blocks of edge sharing CoO_6 octahedra, sandwiched between electrically insulating rock-salt type blocks; along the crystallographic c-axis (Figure 3.1). Additionally, the building blocks of this class of compounds are expressed as $[ABO_4]^{RS}[CoO_2]_q$ (A = Ca, Bi and B = Ba, Sr) and, match perfectly along the crystallographic a- and c-axes. However, there is a large mismatch along the b-axis orientation because of their different b-lattice parameters ($q = b_{RS}/b_{CoO2}$, called misfit ratio; q=1.82 for BSCO[4]). The misfit nature of the crystal structure results in low thermal conductivity, which together with a large S and a low resistivity shows a $zT \geq 1$ [$zT = (\sigma S^2/\kappa)*T$, where σ, S, κ and T are electrical conductivity, thermopower, thermal conductivity and absolute temperature respectively] at 1000 K in BSCO crystal.[5] Thus, this class of compounds is considered as promising thermoelectric material for practical applications.

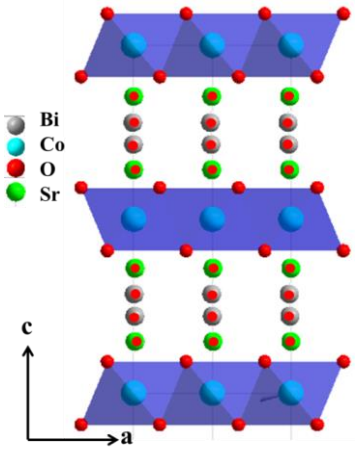

Figure 3.1 Crystal structure of misfit $Bi_2Sr_2Co_2O_y$. Electrically insulating rock salt type layers and hexagonal CoO_2 layers form a super lattice along c-axis.

The decoupling nature of electrical conductivity and S were observed in misfit cobaltates thin films. Whereas no change in thermopower was observed in $Na_{0.5}CoO_2$ (NCO),[6] and BSCO thin film[7] upon reducing the film thickness down to 5 nm, a considerable increase in the

electrical resistivity was observed below 30 nm. As thermal conductivity is mainly governed by the misfit nature of the building blocks, overall thermoelectric performance can be improved by individually tuning the transport coefficients.

An epitaxial thin film is a useful platform for investigating the crystal structure and thus, physical properties. A huge increase in power factor has been observed recently in Na_xCoO_2 thin films by microstructural engineering (by controlling crystallinity and average grain size). The measured power factor of Na_xCoO_2 thin film grown on LSAT (001) substrate was as high as ~ 8 $\mu W/cmK^2$ at 300 K combined with a dramatically low cross plane thermal conductivity ($\varkappa$ = 1.4 ± 0.1 W/mK).[8]

The origin of high S of layered cobaltates is still a matter of intense debate. S was calculated for Na_xCoO_2 using Boltzmann transport theory of metals by Singh et al.[9] Later, a very good match was observed between measured temperature dependent S and that calculated from high resolution ultraviolet photoemission spectroscopy near Fermi energy.[10], [11] Therefore, the unique electronic band structure was proposed as being responsible for the coexistence of metallic electrical conductivity and large S. On the other hand, S near 300 K tends to saturate for misfit cobaltates. Such a saturation of S is considered as the high temperature limit, typically observed for systems with strongly interacting localized charge carriers (polarons), expressed by Heike's formula, as shown in equation 1.21, where *x* is the number of electrons per unit cell, which can be measured by Hall effect . However, valence of cobalt ion (or oxidation state) obtained from Hall effect measurement was found to be lower[12] than that obtained from other experimental techniques, such as angle resolved photoelectron spectroscopy (ARPES).[11] Therefore, calculation of the expected S from Heike's formula using the measured *x* from different experimental techniques, overestimate the measured S, clearly demonstrating a discrepancy between the Hall measurement and ARPES measurements. Koshibae et al [13], [14] suggested that entropy due to spin-orbital degeneracy (β), in addition to the Heike's formulae, has an important contribution to the large S. Hence, an extended Heike's formula (equation 1.21) have been frequently used by many authors to interpret the data. Recently, Rivas-Murias et. al.[15] have shown that room temperature thermopower can be well understood without the spin orbit degeneracy factor (β).

$$S_{T\to\infty} = -\frac{\kappa_B}{e}\ln\left(\beta\frac{x}{1-x}\right) \qquad (1.21)$$

In this chapter, we aim to test such discrepancy between the Hall effect and thermopower in a series of highly c-axis oriented BSCO thin films having different oxygen stoichiometry and therefore different charge carrier concentrations.

3.2 Preparation of BSCO target

$Bi_2Sr_2Co_2O_y$ target (diameter=2cm and thickness=3mm) was synthesized by conventional high temperature solid state diffusion reaction. A stoichiometric mixture of Bi_2O_3, $SrCO_3$, Co_3O_4, $CaCO_3$ was mixed in an agate mortar to obtain homogeneous powder. The powder was pressed using a stainless steel die in a pellet under a 25 metric ton uniaxial press. The heating profile of the synthesis was a two step processes consisting of calcination followed by sintering in air. The pellet was slowly heated up to 860 °C and calcined for 40 hours in air at the same temperature and then slowly cooled down to room temperature. The calcined pellet was ground into fine powder and then pressed into a pellet under 30 metric ton uniaxial press for 30 minutes to achieve high density. The pellet was then placed into a tubular furnace and sintered at 890 °C for 20 hours at pure 1atm O_2. The powder X-ray diffraction patterns of the BSCO target before and after annealing are depicted in Figure 3.2. A subset of reflections coming from the rock salt layer arrangement was indexed and no impurity phases were detected.

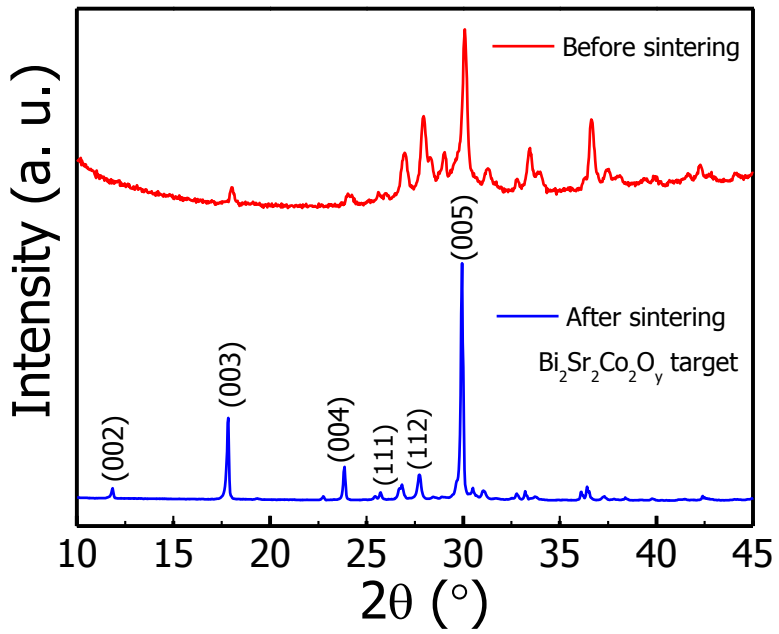

Figure 3.2 PXRD pattern of BSCO target before and after sintering.

3.3 Thin film deposition

Stoichiometric $Bi_2Sr_2Co_2O_y$ target was used deposit thin film by pulsed laser deposition (PLD) technique. Thin film deposition was carried out by using a KrF excimer (248 nm) at 3Hz pulse repetition rate at a laser fluency of 1.8 J/cm^2 at 700°C. A stable pO_2 (≈150 mTorr-) was maintained throughout the deposition process and the pO_2 was increased to 600 mTorr while cooling down. BSCO films were grown on LAO (001) and STO (001) substrates in exactly the same conditions.

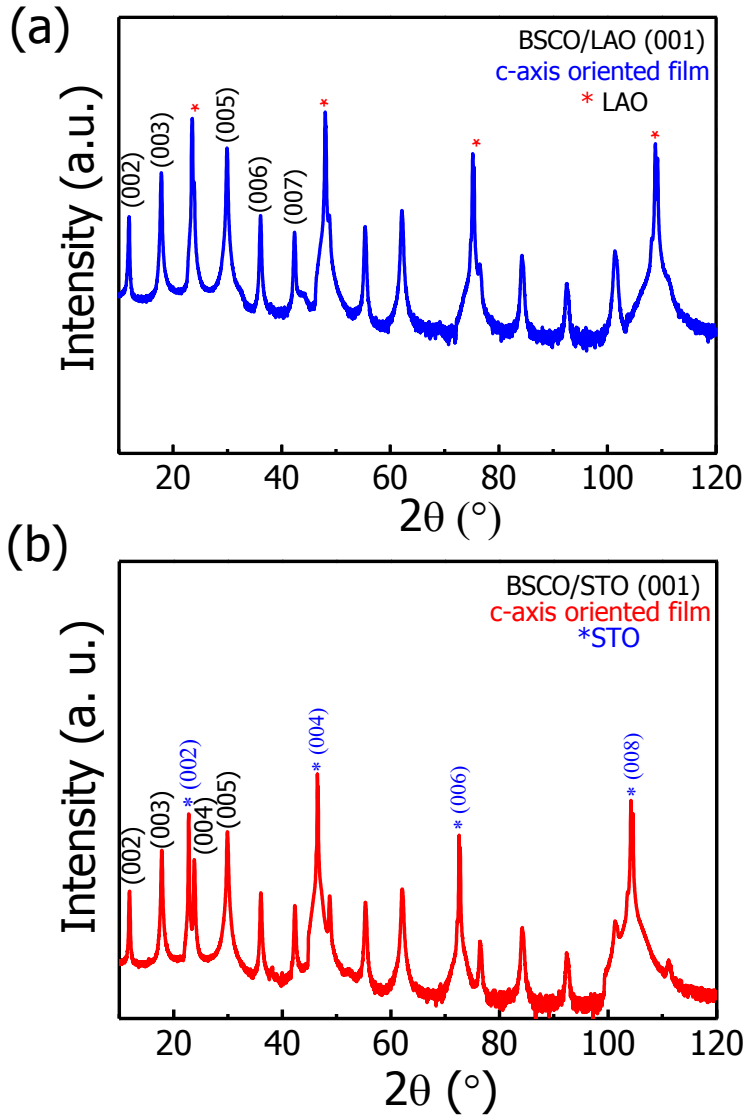

Figure 3.3 XRD patterns of BSCO thin film grown on (a) LAO (001) and (b) STO (001). Both the films are highly c-axis oriented.

3.4 Structural characterization of BSCO thin film by X-ray diffraction

Figure 3.3 depicts the X-ray diffraction patterns of a 200 nm thick $Bi_2Sr_2Co_2O_y$ thin film grown on $LaAlO_3$ (001) and $SrTiO_3$ (001) substrates. The pattern shows only diffractions from the (00*l*) planes of BSCO with an out-of-plane c-parameter 14.928 Å (error estimated $\pm 10^{-4}$ Å). Thus, the BSCO film is purely c-axis oriented. In attempt to analyse the in-plane texture of the film on LAO (001), pole figures (PF) were measured of asymmetric reflections (113). Figure 3.4 represents (the stereographic projection of plane orientation distributions) PF measurement of the BSCO film around (113) reflections and substrate LAO single crystal around (101) reflections, respectively. Four different reflections separated by 90° in ϕ-angle (azimuthal angle) and constant χ = 45°were observed for (101) plane of LAO crystal as it corresponds to pseudo cubic structure (single crystal substrate) while in the (113) reflection of BSCO film appears continuously in the ϕ-scan forming a ring in the stereographic projections at a constantχ = 45° which means that (113) asymmetric reflections have no preferred in plane orientation.

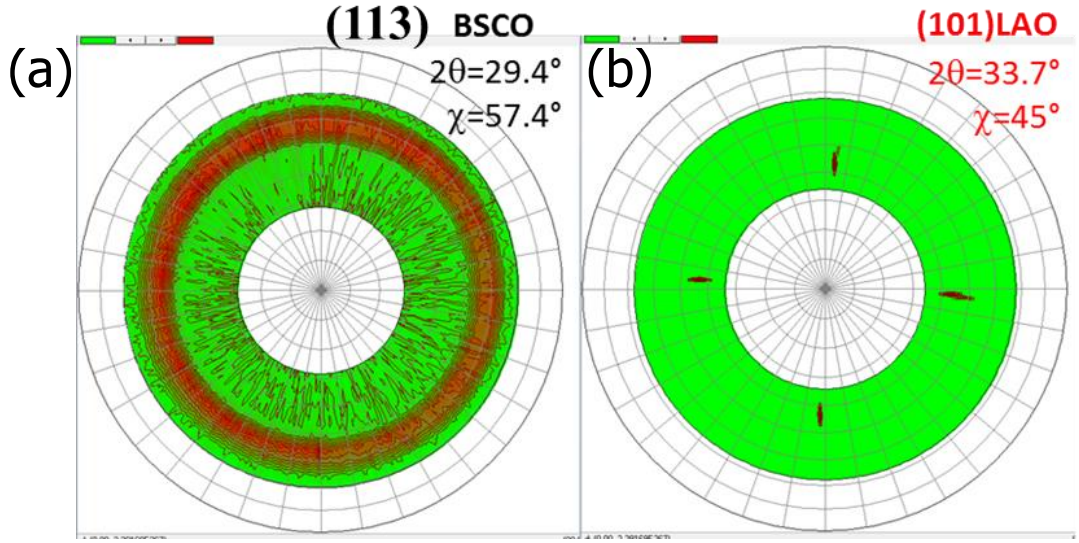

Figure 3.4 X-ray pole figure measurement of BSCO thin film grown on LAO (001) substrate. BSCO film shows random distribution of in-plane texture: (a) In-plane orientation of BSCO film and, (b) in-plane texture of the LAO (001) substrate.

In spite of the film not being fully epitaxial, the high c-axis orientation preserves the layered structure (only random crystal orientation is observed in the ab plane). This makes the measurement of these films highly interesting and somehow closely related to what is expected in the case of single crystalline materials.

3.5 Valence band XPS

No information about the electrically conducting CoO_2 layer, which was sandwiched between rock salt type layers, was obtained from XRD. The electronic transport property is mainly governed by the conducting CoO_2 layer. Therefore, the density of states near the Fermi energy (E_F) should be dominated by the Co(3d)-O(2p) hybrid molecular orbitals.[16] The valence band spectrum of our film at 300 K shows Co(3d)-O(2p) hybridization dominating from Fermi energy to 2 eV, as shown in Figure 3.5. The sharp peak around 1.5 eV indicates the low spin states ($t_{2g}^6 e_g^{0,}$ LS) of Co^{+3} ions. [11] Carbon impurity on the surface of BSCO thin film was observed but, we did not expect the carbonate to interfere with the valence band spectra of CoO_2. VB-XPS spectra of $Bi_2Sr_2Co_2O_y$ thin film shows similar behavior like bulk crystals,[11],[17] proving the high crystalline quality of our films.

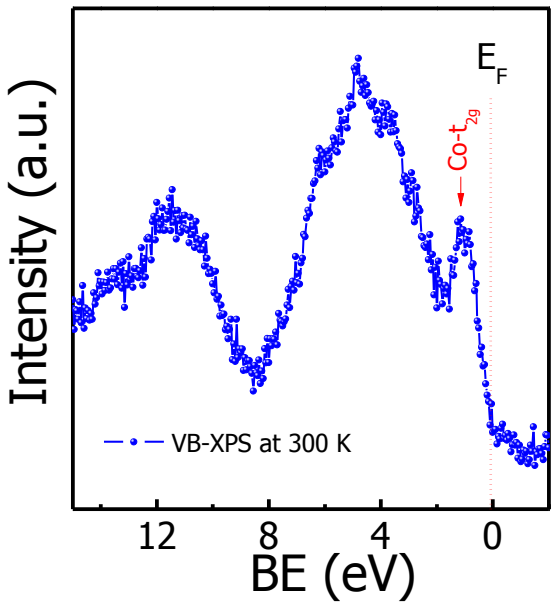

Figure 3.5 Valence band-XPS of BSCO film. VB-structure is dominated by Co-3d and O-2p hybridization.

3.6 High temperature stability of BSCO thin film

High temperature stability of the thin film was checked by high temperature X-ray diffraction in a synthetic air atmosphere (21% O_2 + 79% N_2). X-ray patterns (shown in Figure 3.6) of selected region were collected during heating up to 500 °C and during cooling down. The c-

axis parameters were extracted from the (009) reflection. The progressive shift to lower 2θ angles of the peak position from RT to 500 °C indicates the thermal expansion of c-parameters from 14.921 to 15.038 Å. A linear variation of the c-parameter was observed while heating the film from RT to 600 °C and cooling from 600°C down to RT. The change of c-parameters was from 15.038 Å to 14.945 Å during cooling down. However, cooled sample showed a larger c-parameter than the as grown film. A closer look at the cell parameter variation may indicate the onset of the energy loss at this low temperature. The cooling data shows a linear dependence with temperature. The thermal expansion coefficient is 1.31 x 10^{-5} K^{-1} calculated from cooling data in Figure 3.6c and a temperature of 600 °C was chosen to perform subsequent annealing at different pO_2.

3.7 Stabilization of oxygen non-stoichiometry in the thin film

Different oxygen non-stoichiometry was stabilized by annealing the film at different pO_2 (from 10^{-5} atms to 1 atms) at 600 °C. To check how the change of pO_2 affected the film, an in-situ ac-conductivity measurement at 1 kHz frequency (2 contact measurement) was performed. Electrical conductivity was very stable when 1 atm pO_2 was maintained at high temperature, as depicted in Figure 3.7a. BSCO/LAO films show metallic conductivity with increasing temperature (linear variation of conductivity with T) and there is a slight change in the slope while heating. When the film was annealed at N_2 atmosphere (20 ppm pO_2); the conductivity started decreasing and saturated after a certain time, while cooling down, conductivity followed a different trajectory (Figure 3.7). When the film was reannealed at 1 atm pO_2, the conductivity started to decrease following the same value as previous step until about 500 K. It then started to increase, recovering the higher maximum conductivity at about 700 K (presumably recovering the oxygen content) from which it began to decrease again following a straight line. Once the 1 atm pO_2 was maintained conductivity started increasing with increasing temperature. It saturated after a certain time and follows a different trajectory. Once the 1 atm pO_2 is maintained, the film showed metallic behavior, as before. This indicates that the film can be fully oxidized or reduced reversibly. These oxidation-reduction behaviour is very similar with the oxygen stoichiometry changes measured by thermogravimetric analysis observed in bulk crystals.[18] Therefore, we assign the change of conductivity to the change of the oxygen stoichiometry in the thin film. This implies that a certain oxygen stoichiometry can be stabilized in film if a controlled pO_2 is maintained during the annealing process. The sample was kept at a constant temperature (450 °C and 600 °C) and pO_2 was varied in the range of (3×10^{-2} atms to 1 atms) with different mixture of nitrogen and oxygen flow. Sufficient time (1 hour) was held to gradually reach the

equilibrium after every pO_2 change and conductivity was measured. The pO_2 dependence of the conductivity provides a positive slope with as depicted in Figure 3.7c. This indicates that the BSCO film is dominated by hole transport. The higher the temperature, the lower the conductivity indicates that oxygen content decreases with increasing temperature (meaning the higher the T, the higher the Co^{+4}/Co^{+3} ratio). This is expected for misfit cobaltates which contain a mixed valence of cobalt ion of a Co^{+3}/Co^{+4} pairs. Three different films grown on LAO (001) were annealed in the same conditions as mentioned before, for thermoelectric characterization. Thermoelectric properties of the BSCO/LAO films were measured in order to compare with data reported in the literature. As grown film, film annealed at 600°C in 1 atms pO_2 (will be abbreviated as O_2-annealed) and another film annealed at 600°C in 20 ppm pO_2 (will be referred to as N_2 annealed).

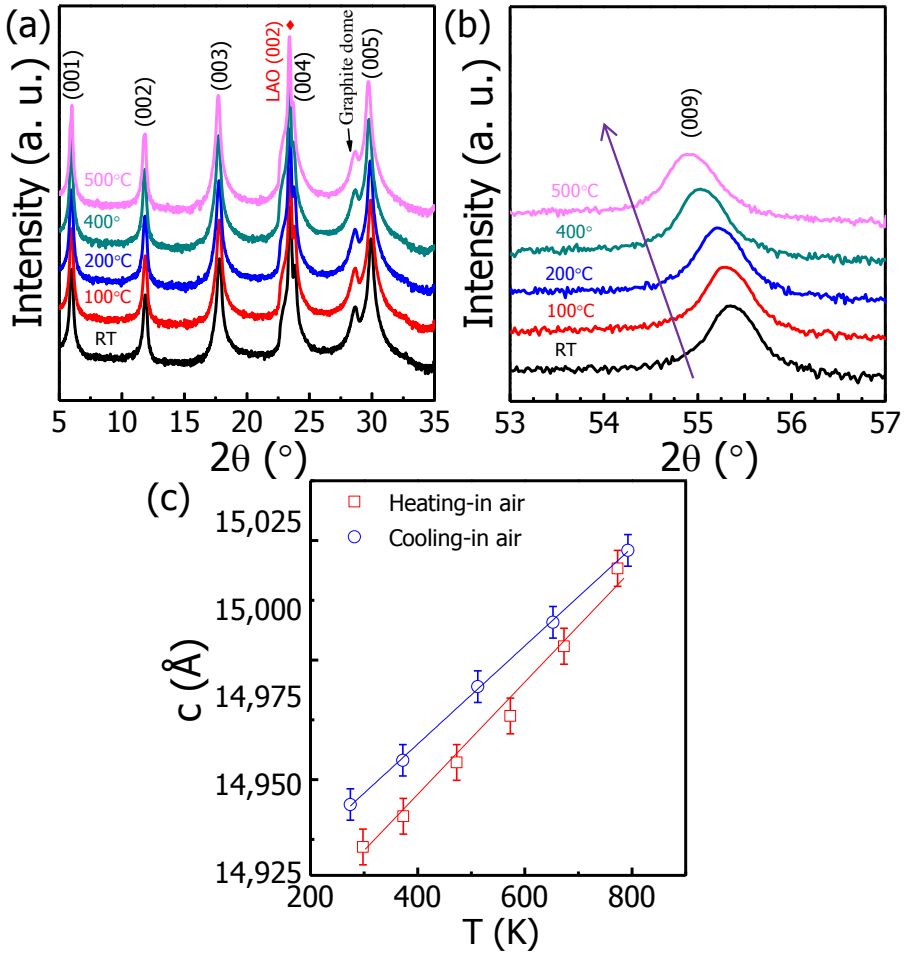

Figure 3.6 High temperature XRD patterns of BSCO film. a) Standard 2θ-ω XRD patterns at different temperature, b) shift of (009) reflection of BSCO film towards left in 2θ with increasing temperature and, c) variation of c-parameter as a function of temperature.

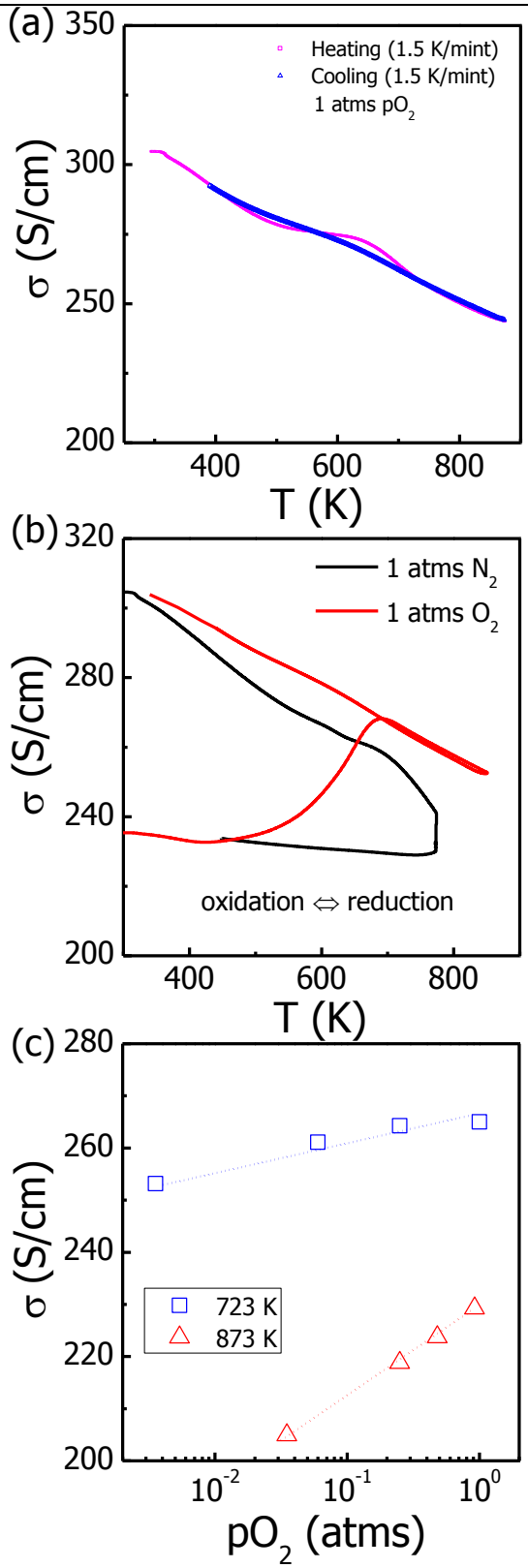

Figure 3.7 High temperature electrical conductivity measurements of BSCO film: a) metallic conductivity when 1 atm pO_2 is maintained, b) isobaric temperature dependent ac-conductivity and, c) isothermal pO_2 dependent ac-electrical conductivity.

3.8 Low temperature dc-electrical conductivity

Figure 3.8 represents the temperature dependent dc-electrical conductivity (σ) of all three GBCO/LAO films. As can be observed, σ increases with decreasing temperature from 300 K down to ~100 K (or lower) for as grown and oxygen annealed films, which is a typical metallic behavior. The conductivity then decreases below 100 K which is consistent with the report for BSCO films grown by other authors.[7],[19] A thermal activation behaviour on the $\sigma(T)$ was observed for N_2-annealed film throughout the whole temperature range of our measurements.

Hall measurements were carried out at 300 K for all the films to understand the origin of change in conductivity (Table 3.1). An increase or decrease of conductivity might be associated either with the change of charge carrier density or with the variation in carrier mobility. The changes of mobility of carriers of the as grown and the annealed samples are subtle as depicted in Table 3.1. Therefore, the changes of σ in the O_2 and N_2 annealed samples were more likely to be caused by changes in the charge carrier concentration rather by change in the mobility.

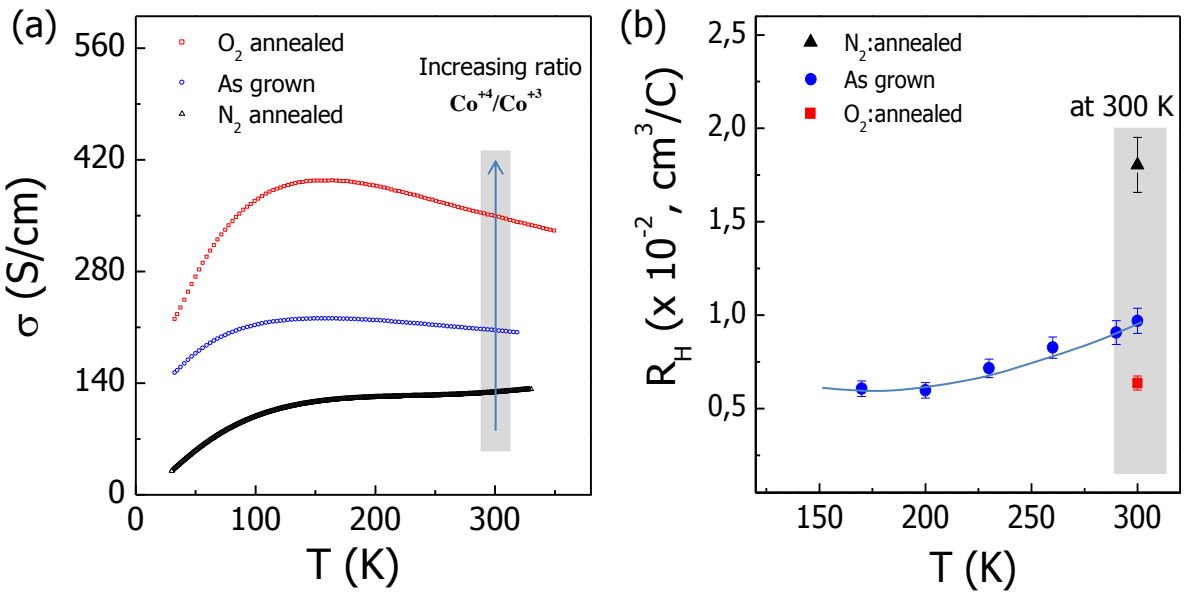

Figure 3.8 Electronic transport properties of BSCO films. (a) Temperature dependent electrical conductivity of as grown and annealed BSCO films from 350 K down to 30 K. (b) Hall resistance of the BSCO as grown and annealed films. Charge in conductivity at 300 K is assigned due to the increase of Co^{+4}/Co^{+3} ratio.

Table 3.1 Electron density of BSCO films at 300 K.

Sample	Hall electron density, n ($\times 10^{20}$ cm^{-3})	Cell volume ($\times 10^{-24}$ cm^3)	Electron concentration, x, per unit cell	Electrical conductivity (S/cm)	Electron mobility μ (cm^2/V.s)
N_2-annealed	3.00±0.24	372.6	0.1143±0.009	129	2.68±0.21
As grown	6.38±0.39		0.2143±0.013	206	2.01±0.12
O_2-annealed	9.78±0.40		0.3736±0.015	350	2.23±0.09

3.9 Seebeck effect

Schematic illustration of the Seebeck effect measurement of BSCO/LAO films is shown in Figure 3.9. Two different experimental set up (and sample dimensions) were used to measure S and data were plotted separately in Figure 3.12. From 300 to 50 K, the measurements were performed with a homebuilt cryostat in vacuum (Figure 3.9a) while a different set of samples were used to measure high temperature S (Figure 3.9b) with a LINSEIS instrument in a fixed helium atmosphere. Figure 3.10 depicts the thermoelectric response when a fixed temperature

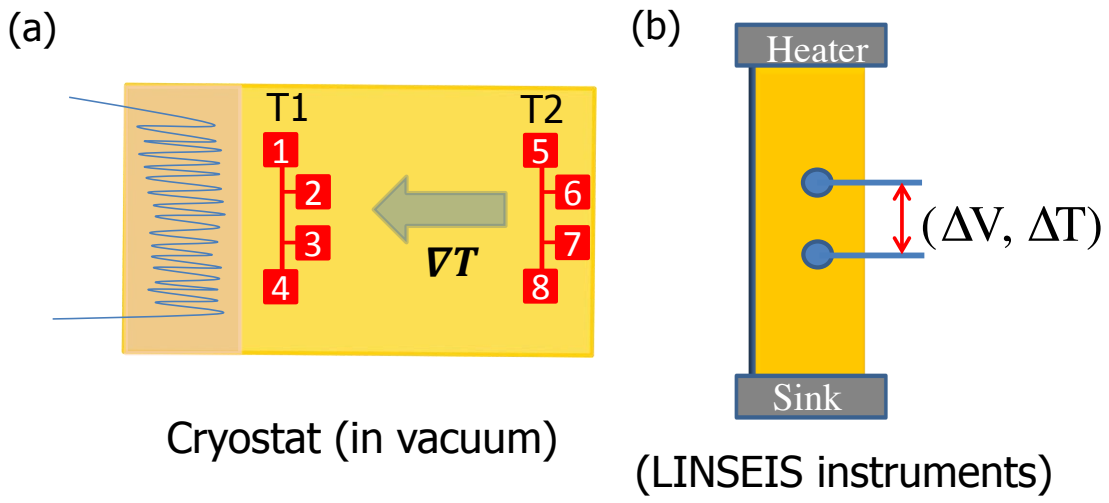

Figure 3.9 Schematic illustration of the Seebeck effect measurement: (a) in cryostat at low temperature (sample dimensions were 5 mm×5mm×200 nm) and, (b) at high temperature in LENSEIS instruments (sample dimensions were 10 mm×5 mm×200 nm).

gradient is established from the set up shown in Figure 3.9a. As can be observed, thermoelectric voltage varies linearly with the applied power ($\Delta V \propto i^2R$, where i and R is the applied current and resistance of the ceramic heater) and the temperature difference (T_1-T_2=ΔT) between two resistors is also proportional to the power ($\Delta T \propto i^2R$). This indicates that the measured open

circuit voltage originates from the thermoelectric effect. Seebeck coefficient (*S*) was calculated from the slopes of -ΔV/ΔT curve as depicted in Figure 3.11. One of the interesting finding is that the ΔT decreases with decreasing temperature when a fixed power is applied (highlighted in Figure 3.10b). This is in good agreement with the increase of thermal conductivity of LAO substrate.[20] Thus, it can be concluded that the majority of the heat was transported through the LAO substrate.

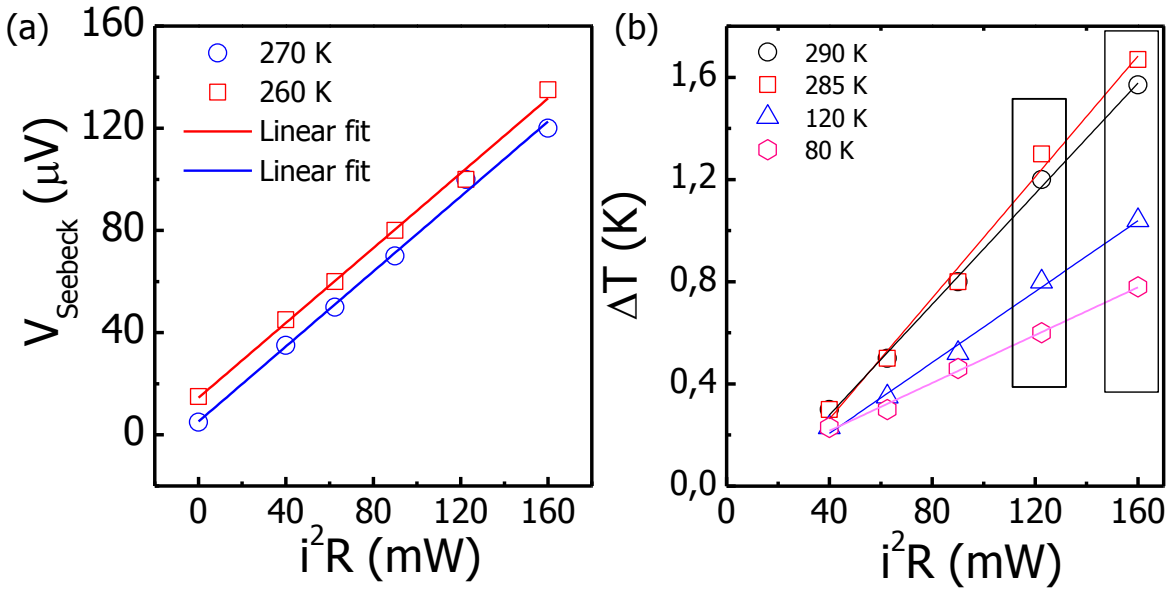

Figure 3.10 Thermoelectric Seebeck effect. Linear response of (a) the Seebeck voltage (ΔV) and (b) the temperature gradient (ΔT) with the power applied to the heater of the as grown BSCO film. Empty square rectangular boxes show that the ΔT decreases with increasing temperature when a fixed power applied.

Temperature dependent *S* from 40 to 500 K of all the films is plotted in Figure 3.12. Measured *S* of as-grown and N_2-annealed films at 40 K are 73 and 89 μV/K, respectively. *S* increases linearly with increasing temperature from 40 to 100 K for the as-grown film and 40 to 150 K for N_2-annealed film, which is typical metallic behavior. *S* measurements in two different experimental set ups in separate ranges of temperature is quiet comparable at 300 K. High temperature measurements from 320 K to 500 K reveal that these *S* remains almost temperature independent for both the films. O_2-annealed BSCO film achieves an S value of 95 μV/K at 320 K. It remains almost temperature independent up to 400 K and then started to increase with increasing temperature further to 450 K. Such temperature independent S is typical for polarons. This can be expressed by Heike's formula as shown in equation 1.21.

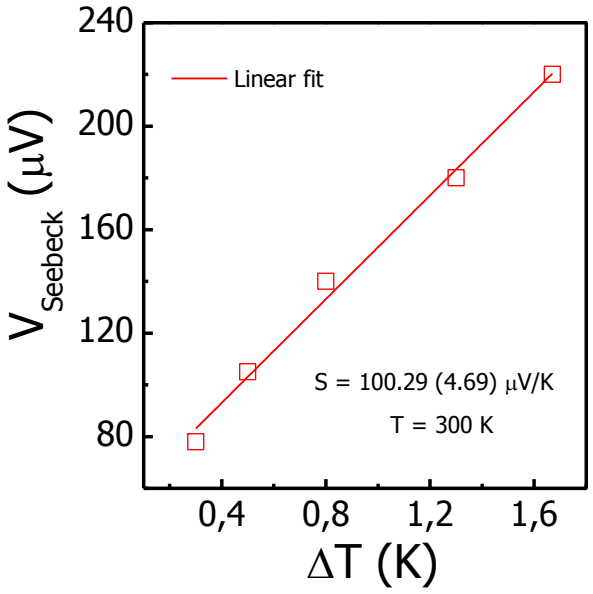

Figure 3.11 Seebeck coefficient of as grown BSCO film at 300 K calculated from the slope of -ΔV vs ΔT curve.

It follows that S can be calculated from Heike's formula if *x* and β values are known independently. *x* can be calculated if the charge carrier density is known by using equation 3.2. We performed Hall effect measurements at 300 K and the calculated *x* is summarized in Table 3.1 Spin-orbit degeneracy, β, can be calculated once the spin states of cobalt ions and orbit splitting are known. In this chapter, our aim is to verify whether the calculated S from Hall carrier density (n, cm^{-3}) by Heike's expression agrees with the measured S at 300 K or not. The value of β depends on the spin-states and orbital degeneracy of Co^{+3} and Co^{+4} ions, which can be low spin (LS), intermediate spin (IS) and, high spin (HS), depending on the crystal field splitting. Considering these possibilities, a range of β values can be calculated. In the case of BSCO crystal, the reported spin states of Co^{+4} and Co^{+3} ions are low spin of electronic configuration $t_{2g}^5 e_g^0$ and $t_{2g}^6 e_g^0$, respectively. Therefore, we assume the same spin states are present in the BSCO films for cobalt ions. The calculated β value will be 1/6. Interestingly, because of triangular distortion in the CoO_2 layer of BSCO misfit crystal, orbital degeneracy of t_{2g} orbit can be lifted and therefore, it splits into a narrow a_{1g} and a broad e_g' sub band. [21], [11] Taking this fact into consideration, a β value of $^1/_2$ can be calculated.

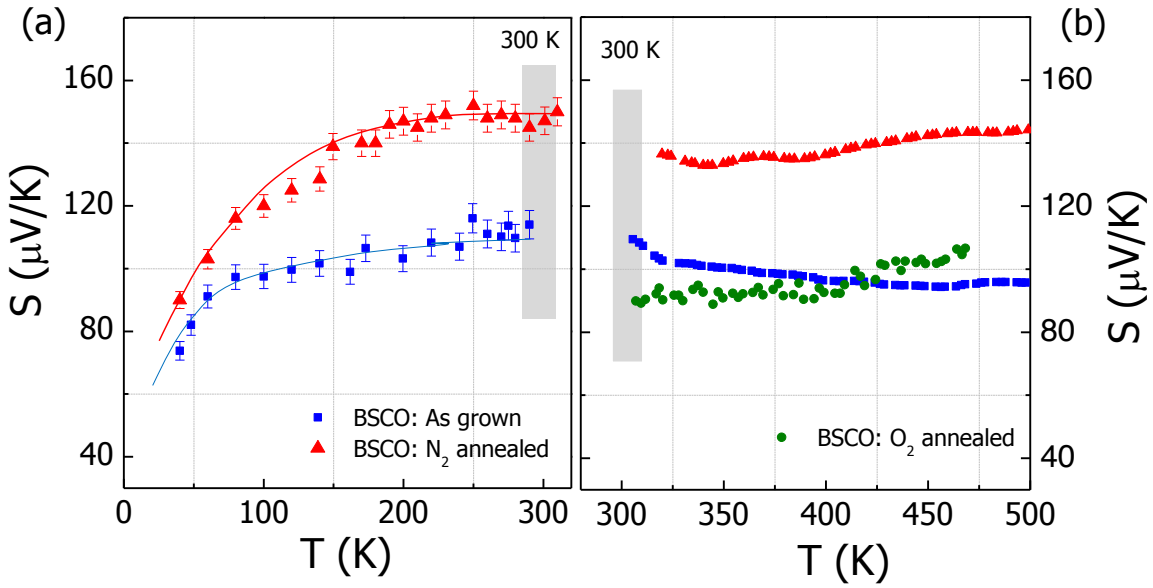

Figure 3.12 Temperature dependent Seebeck coefficient of BSCO films grown on LAO (001) substrates from 40 K to 500 K. (a) Temperature dependent Seebeck coefficient of as grown and N_2-annealed BSCO films from 300 K to 40 K were measured in a cryostat (sample dimensions were 5 mm×5 mm×200 nm) and, (b) Seebeck coefficient of all the three films from 320 K to 500 K were measured in LINSEIS instrument (Sample dimensions were 10 mm×5 mm×200 nm).

$$x = \frac{\text{carrier concentration}}{\text{unit cell}}$$

$$x = \text{Hall electron density}, n_e, (\text{cm}^{-3}) \times \text{Unit cell volume } (\text{cm}^3) \qquad (3.2)$$

Certainly, there is some uncertainty regarding whether to use 1/2 or 1/6 β values to calculate *S* at 300 K. Therefore, *S* was calculated from *x* and all possible β values and more importantly, also without considering β (i.e. β=1) which renders the classical Heike's formula. Figure 3.13 depicts the calculated and the measured values of *S* at 300 K assuming different β values. Apparently the measured and calculated values are close when the factor β (= 1) is neglected. Our results are consistent with the previous report.[15] It can be concluded that in case of our films, *S* at 300 K can be understood without the spin-orbit degeneracy factor (β) in addition to the Heike's formula.

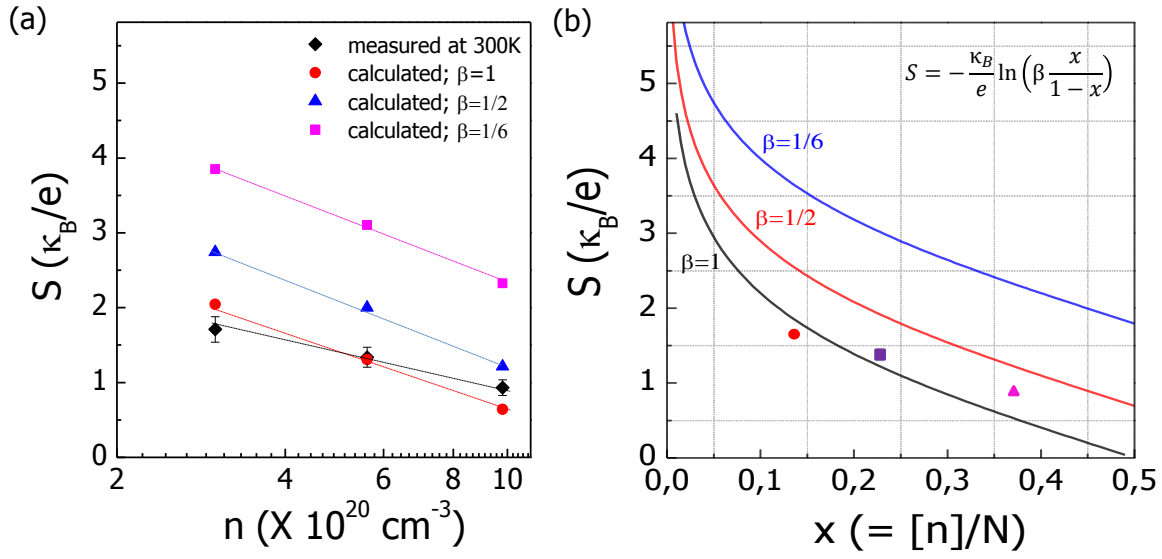

Figure 3.13 Measured Seebeck coefficient and expected from Heike's formula (using Hall electron density data) at 300 K of the as grown and annealed BSCO films grown on LAO (001) substrates (left) and Expected dependence of S with number of electrons per unit cell from Heike's formula (right). Filled red circle, filled Violet Square and filled pink triangles are the measured Seebeck coefficient for three different BSCO/LAO film.

3.10 Conclusion

In summary, we grew highly c-axis oriented BSCO thin films by the PLD technique. Charge carrier density was controlled by annealing in different oxygen atmosphere. Our results demonstrate that in case of our films, the temperature independent S near 300 K can be understood solely by the Heike's formula without consideration of the spin-orbit degeneracy factor. This means that search for new materials based on the concept of spin-orbit degeneracy factor will be unreliable. Furthermore, indirect determination of spin-states from thermopower measurement will also be unreliable unless an independent experiment is done to determine the spin-states accurately.

Bibliography:

[1] I. Terasaki, Y. Sasago, K. Uchinokura, *Phys. Rev. B* **1997**, *56*, R12685–R12687.

[2] M. Hervieu, A. Maignan, C. Michel, V. Hardy, N. Créon, B. Raveau, *Phys. Rev. B* **2003**, *67*, 45112.

[3] M. Shikano, R. Funahashi, *Appl. Phys. Lett.* **2003**, *82*, 1851–1853.

[4] M. K. H. Yamauchi, K. Sakai, T. Nagai, Y. Matsui, *Chem. Mater.* **2006**, *18*, 155–158.

[5] R. Funahashi, M. Shikano, **2016**, *1459*, 2000–2003.

[6] P. Brinks, G. Rijnders, M. Huijben, *Appl. Phys. Lett.* **2014**, *105*, 1–5.

[7] J. Ravichandran, A. K. Yadav, W. Siemons, M. A. McGuire, V. Wu, A. Vailionis, A. Majumdar, R. Ramesh, *Phys. Rev. B - Condens. Matter Mater. Phys.* **2012**, *85*, 85112.

[8] P. Brinks, B. Kuiper, E. Breckenfeld, G. Koster, L. W. Martin, G. Rijnders, M. Huijben, *Adv. Energy Mater.* **2014**, *4*, 1301927.

[9] D. J. Singh, *Phys. Rev. B* **2000**, *61*, 397–402.

[10] S. Kuno, T. Takeuchi, H. Ikuta, T. Kondo, A. Kaminski, Y. Saito, S. Fujimori, S. Radiation, E. Agency, *IEEE Int. Conf. Thermoelectr.* **2007**, *2*, 99.

[11] S. S. and T. Takeuchi, Tsunehiro, Takeshi Kondo, Tsuyoshi Takami, Hirofumi Takahashi, Hiroshi Ikuta, Uichiro Mizutani, Kazuo Soda, Ryoji Funahashi, Masahiro Shikano, Masashi Mikami, Syunsuke Tsuda, Takayoshi Yokoya, *Phys. Rev. B* **2004**, *69*, 125410.

[12] T. Yamamoto, I. T. Uchinokura, K, *Phys. Rev. B* **2002**, *65*, 184434.

[13] W. Koshibae, K. Tsutsui, S. Maekawa, *Phys. Rev. B* **2000**, *62*, 6869–6872.

[14] W. Koshibae, S. Maekawa, *Phys. Rev. Lett.* **2001**, *87*, 236603.

[15] B. Rivas-Murias, J. M. Vila-Fungueiriño, F. Rivadulla, *Sci. Rep.* **2015**, DOI: 10.1038/srep11889.

[16] T. Mizokawa, L. H. Tjeng, P. G. Steeneken, N. B. Brookes, I. Tsukada, T. Yamamoto, K. Uchinokura, *Phys. Rev. B* **2001**, *64*, 115104.

[17] Y. Wakisaka, *Phys. Rev. B* **2008**, *78*, 235107.

[18] Y. Morita, J. Poulsen, K. Sakai, T. Motohashi, T. Fujii, I. Terasaki, H. Yamauchi, M. Karppinen, *J. Solid State Chem.* **2004**, *177*, 3149–3155.

[19] S. Wang, A. Venimadhav, S. Guo, K. Chen, Q. Li, A. Soukiassian, D. G. Schlom, M. B. Katz, X. Q. Pan, W. Wong-ng, et al., *Appl. Phys. Lett.* **2009**, *94*, 22110.

[20] E. Langenberg, V. Leborán, A. O. Fumega, V. Pardo, F. Rivadulla, E. Langenberg, V. Leborán, A. O. Fumega, V. Pardo, *APL Mater.* **2016**, *4*, 104815.

[21] M. Pollet, J. P. Doumerc, E. Guilmeau, D. Grebille, J. F. Fagnard, R. Cloots, *J. Appl. Phys.* **2007**, *101*, 83708.

Chapter 4: Thermoelectric properties of epitaxial $GdBaCo_2O_{5.5+\delta}$ thin films

The thermopower of $GdBaCo_2O_{5.5+\delta}$ bulk crystals is very high (> 500 μV/K) at 100 K but the resistivity is also very high (>1-10^2 ohm.cm). Furthermore, the origin of such high thermopower and doping dependence were explained in terms of the spin-orbit degeneracy (in addition to Heike's formula) of the cobalt ions present in the octahedral and pyramidal CoO_2 coordination geometries. It is noteworthy that Heike's formula is strictly applicable when thermopower is temperature independent.

In this chapter, a strong temperature dependence on the thermopower of the thin films is observed from 200 to 300 K similar to bulk crystals. Therefore, the experimental results; presented here are analyzed in order to find out the true high temperature limit of the thermopower in the case of $GdBaCo_2O_{5.5+\delta}$ thin film grown on $SrTiO_3$ (001) substrates.

4.1 Introduction

Layered cobaltates can be differentiated based on the type of CoO_2 layer present in the crystal. As discussed in the last chapter, misfit cobaltates have triangular CoO_2 layers with Co in the center of an oxygen octahedral connected by edge sharing, while layered perovskites, such as $GdBaCo_2O_{5.5+\delta}$ (GBCO) can be derived from a square CoO_2 lattice with octahedral connected by their corners. In this compound, Gd and Ba cations layers alternate in the crystal structure along the crystallographic c-axis. CoO_2 layers are sandwiched between the GdO and BaO layers (Figure 4.1). Therefore, the sequence of the layer stacking along the c-axis is – [BaO] – [CoO_2] – [GdOx] – [CoO_2] –, which doubles the c-parameter with respect to simple perovskites. Non-stoichiometric compounds can accommodate additional oxygen vacancies and therefore, a structural phase transition is present in the crystals depending on the amount of oxygen vacancies they hold. The reported crystal structure of stoichiometric GBCO is orthorhombic (of space group *Pmmm*) at room temperature. [1], [2]

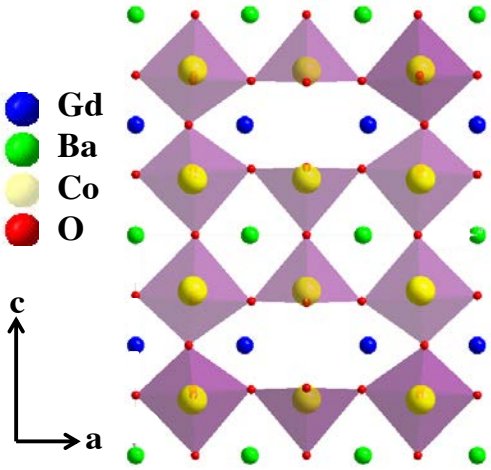

Figure 4.1 Crystal structure of $GdBaCo_2O_{5.5}$. Cobalt ions are present in two types of coordination geometries; octahedral and pyramids.

We start the discussion from section 1.10 in chapter 1, where the transport properties of GBCO and HBCO crystals were described. This chapter is focused on understanding the true high temperature limit of S in GBCO films grown on STO (001) substrates. A series of GBCO films of 10 to 100 nm thickness, were grown and the thermoelectric properties of GBCO thin films are reported here for the first time. Thermopower (*S*), electrical resistivity (ρ) and the Hall effect (at 300K) of 25 to 100 nm GBCO films were measured as a function of temperature. Temperature independent S (T≥300K) is discussed in the light of Heike's formula.

4.2 Thin film growth and structural characterization

GBCO films were grown by the pulsed laser deposition (PLD) technique. The growth conditions of the GBCO film on STO substrates, summarized in Table 4.1, were used for the growth of thin films ranging from 10 to 100 nm in thickness.

Table 4.1 Growth conditions of GBCO films by PLD technique.

Growth conditions of GBCO thin films on STO (001) substrates	
pO_2	60 mTorr
Temperature	850 °C
Laser fluency	1.5 J/cm^2
Laser frequency	10 Hz
Heating/cooling rate	10 °C/minute

Standard 2θ-ω XRD patterns of GBCO thin film grown on STO (001) substrate are shown in Figure 4.2a. As can be seen, all reflections from the film can be indexed to (00*l*) planes, indicating that GBCO films on STO (001) substrates are highly c-axis oriented. Furthermore, the presence of both odd and even (00*l*) reflections indicates the double perovskite nature of the thin film i.e. GdO_x and BaO layers are stacked alternatingly along the crystallographic c-axis. Figure 4.2b shows the high resolution 2θ-ω patterns of 10 to 100 nm GBCO thin films around (002) STO and (004) GBCO reflections. Clear Kiessig fringes were observed at both sides of the film peaks. This indicates the presence of smooth interfaces and a definite thickness of the films. A systematic left shift of (004) reflection in 2θ with decreasing film thickness indicates the systematic increase of the c/2-parameter of the films. The thickness of the films was determined by X-ray reflectivity (XRR) measurements (Figure 4.3a). The gap between the two maxima or minima of the fringes appearing in the XRR patterns decreases as the thickness of the films decreases. The slope of the XRR patterns increases with increasing thickness which indicates that the roughness of the film surface increases with increasing thickness. Scanning electron microscopic (SEM) images of the surface of GBCO films are compared in Figure 4.3b and c. Small grain size precipitates are visible on the surface of the 100 nm films while the surface of the 25 nm GBCO film is flat.

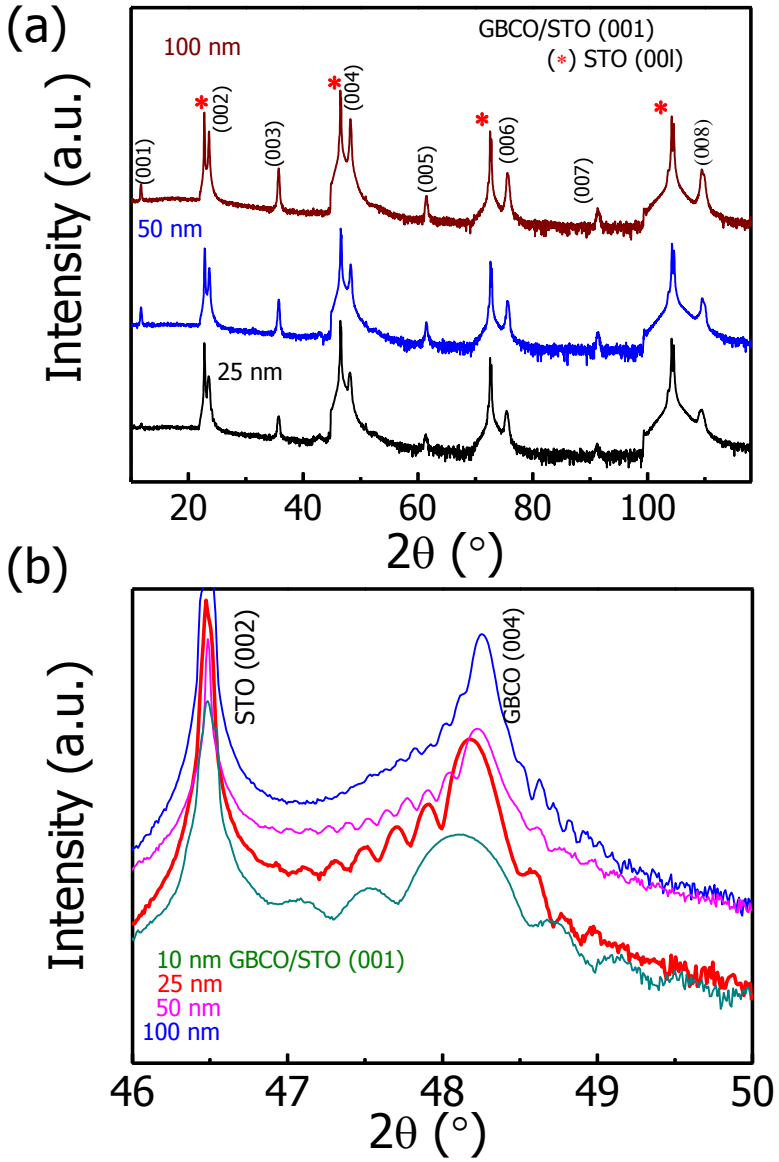

Figure 4.2 X-ray diffraction of GBCO thin film. a) Standard 2θ-ω pattern of GBCO film grown on $SrTiO_3$ (001) substrate. Odd and even reflections from GBCO film indicates the double perovskite nature with alternating BaO and GdO layers along c-axis. b) High resolution XRD around (002) reflections of STO (001). Left shift of the (004) reflection of GBCO film with increasing thickness indicates the increase of c/2-parameters.

In-plane cell parameters of GBCO films on STO (001) substrate were extracted from reciprocal space maps (RSMs) (depicted in Figure 4.4). RSMs were performed around (-303) reflections of the STO substrate and GBCO film. As can be observed, the in-plane lattice parameters of 10 nm GBCO film and STO substrate match perfectly (same Q_x coordinates and therefore a = b tetragonal). This indicates that the film is fully strained with the STO substrate.

With increasing thickness, c-parameter decreases while the in-plane parameters are fully strained with the substrate and then an intense spot splits into two different spots of the same Q_y (i.e., c-parameters do not change) but a different Q_x for the 100 nm film. It is likely that the in-plane parameter splits into b/2- and a-parameters with increasing thickness. The change of the lattice parameters of the GBCO films is presented in Figure 4.5 as a function of increasing thicknesses. The graph combines measurements of in-plane and out-of-plane cell parameters obtained from reciprocal space maps as well as parameters obtained from linear scans. This indicates that the thicker films release their strain to achieve bulk lattice parameters while thinner films are fully strained.

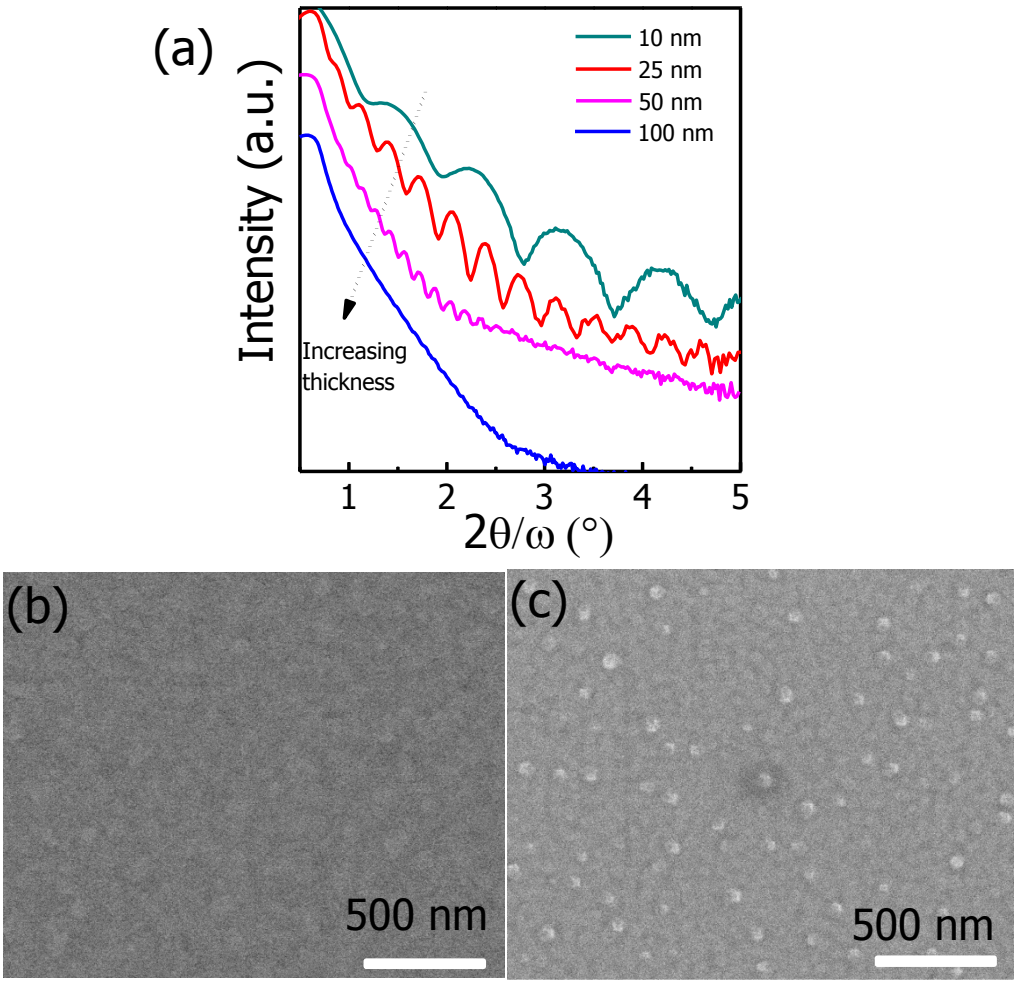

Figure 4.3 Quantitative thickness determination and qualitative comparison of surface roughness of GBCO films: (a) X-ray reflectivity (XRR) of GBCO films. Curves are shift in intensity for clarity; (b) and, (c) SEM images of the surface of 25 nm and 100 nm GBCO film grown on STO (001).

.

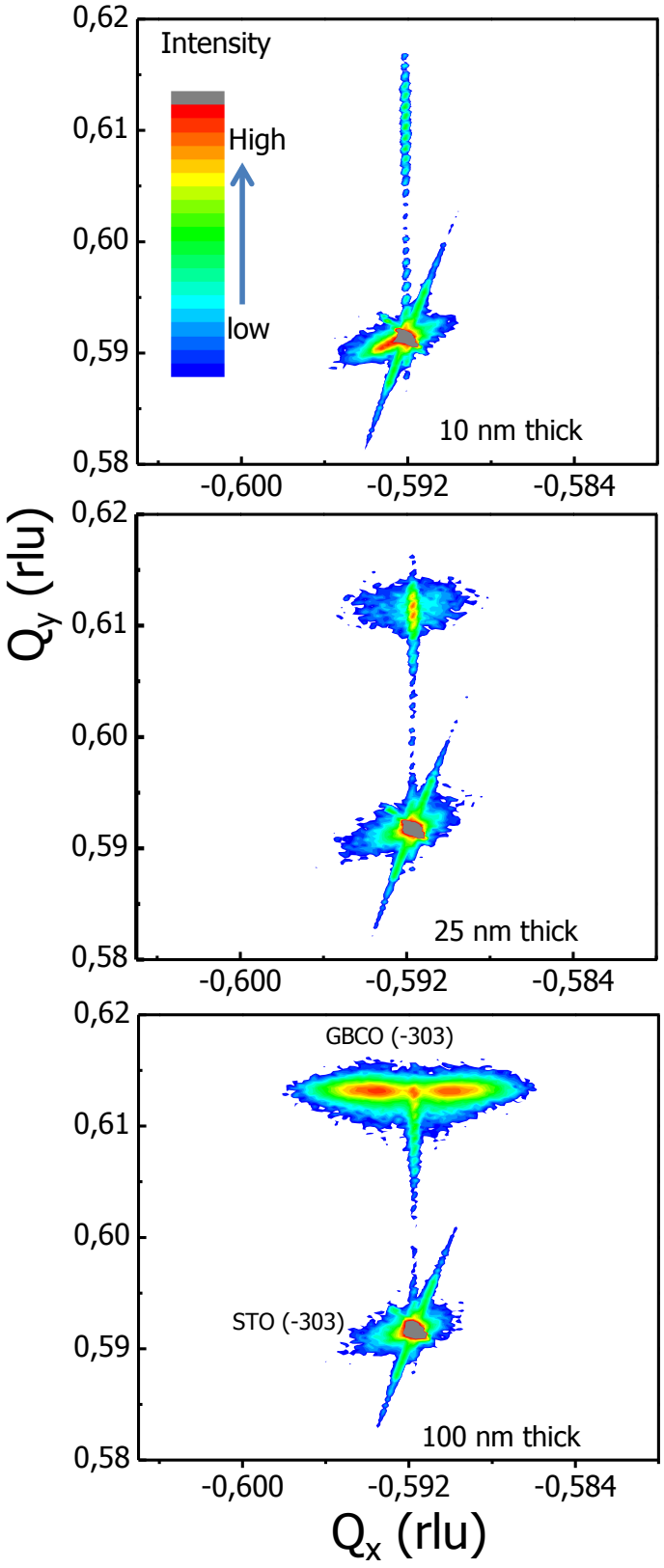

Figure 4.4 Reciprocal space maps (RSMs) of GBCO films around (-303) reflections of STO and GBCO respectively

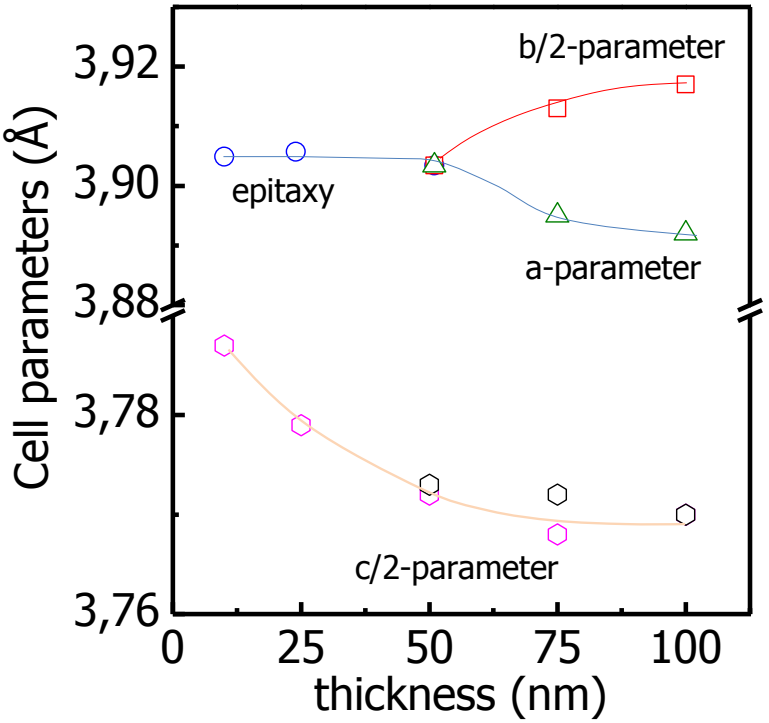

Figure 4.5 Calculated lattice parameters from X-ray diffraction measurements. Blue sphere are in plane parameters of strained 10 nm and 25 nm films. Red empty squares are splitted a-parameters. Green empty triangles are splitted b/2-parameters. All in-plane parameters were calculated from RSM maps. Purple empty hexagons are calculated c/2-parameters from HR 2θ/ω measurements. Black empty hexagons are calculated c/2-parameters from RSMs. All solid lines are guide to eyes.

Elemental scan by X-ray photoelectron spectroscopy (XPS) reveals the presence of Gd, Ba, Co and O atoms. The presence of a small amount of carbon was also detected indicating the formation of carbonates on the surface of GBCO film.The core level XPS spectrum Ba-3d and Co-2p is presented in Figure 4.6a. As the binding energy (BE) of Ba-3d and Co-2p are very close, the peaks overlap. Valence band-XPS of the 100 nm GBCO film reveals similar characteristics to GBCO stoichiometric crystal[8] as depicted in Figure 4.6b which also proves the high crystalline quality of the GBCO film. Furthermore, Ba-5p and Co-3d spectrum can be distinguished in the valence band spectrum. This is likely due to the fact that CoO_2 layers control the electronic transport properties and so the density of states near Fermi energy is dominated by Co (3d)–O(2p) overlapped molecular orbitals.

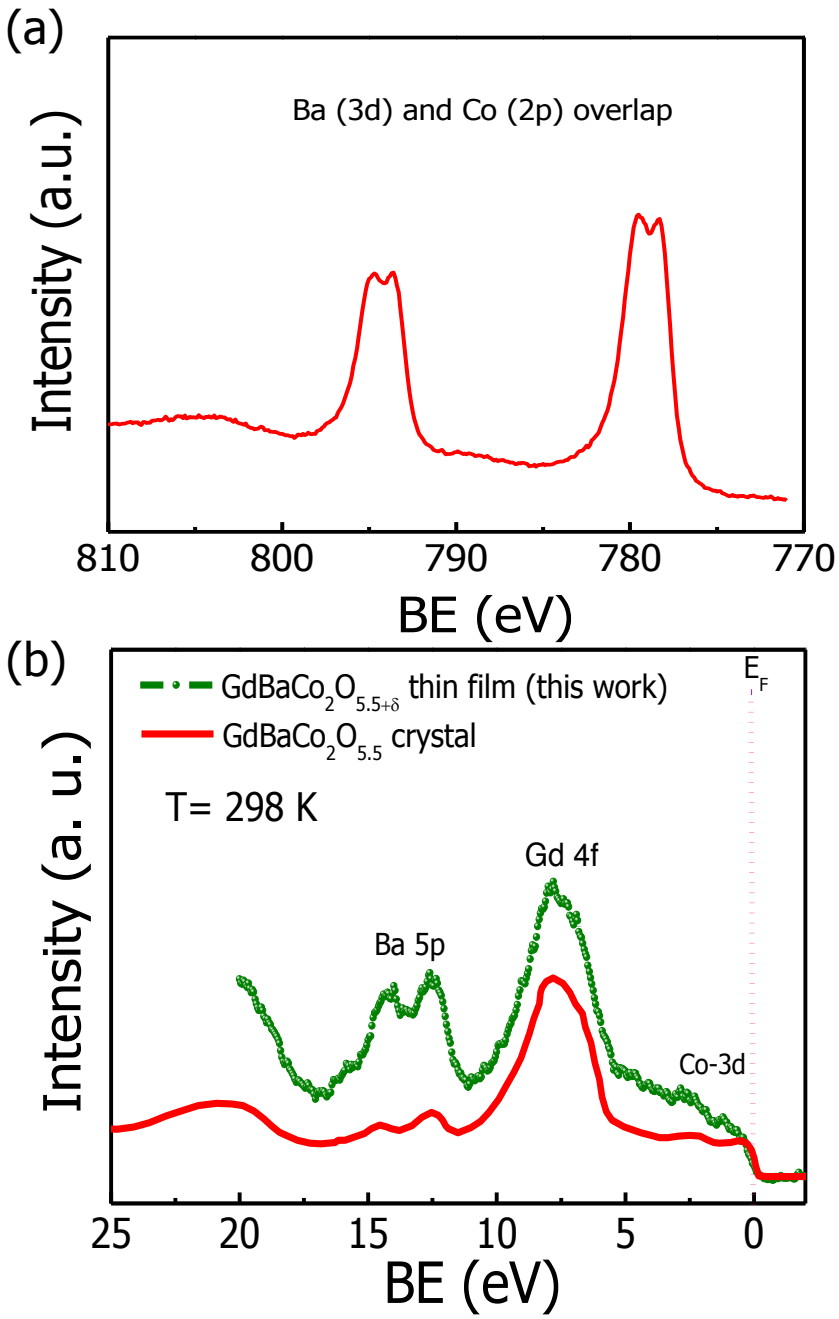

Figure 4.6 X-photoelectron spectroscopy of 100 nm GBCO film. (a) High resolution core level XPS spectrum of Ba and Co atoms and, (b) valence band-XPS of GBCO film compared with stoichiometric GBCO bulk crystal. VB-XPS of GBCO crystal is digitized from literature.[8]

4.3 Electronic and thermoelectric transport properties

Electrical resistivity and Hall effect measurements were performed by the Van der Pauw method as described in Chapter 2. Seebeck effect measurements (the same as described in chapter 2 and 3) of GBCO films on STO (001) are depicted in Figure 4.7. Two Pt resistors were

deposited on the surface of the GBCO films which acts as thermometers and a ceramic heater (100 ohm resistance) was placed on one side of the surface which was electrically isolated from the film by an electrically insulating but thermally conducting polymer coating. As depicted in Figure 4.7b, thermoelectric voltage difference of the GBCO film scales linearly with the applied power to the heater. This indicates that the measured voltage difference originates from the thermoelectric effect. The Seebeck effect measurements above 330 K is done by a standard 4-prove method in a LINSEIS instrument (shown in Figure 3.9b in chapter 3).

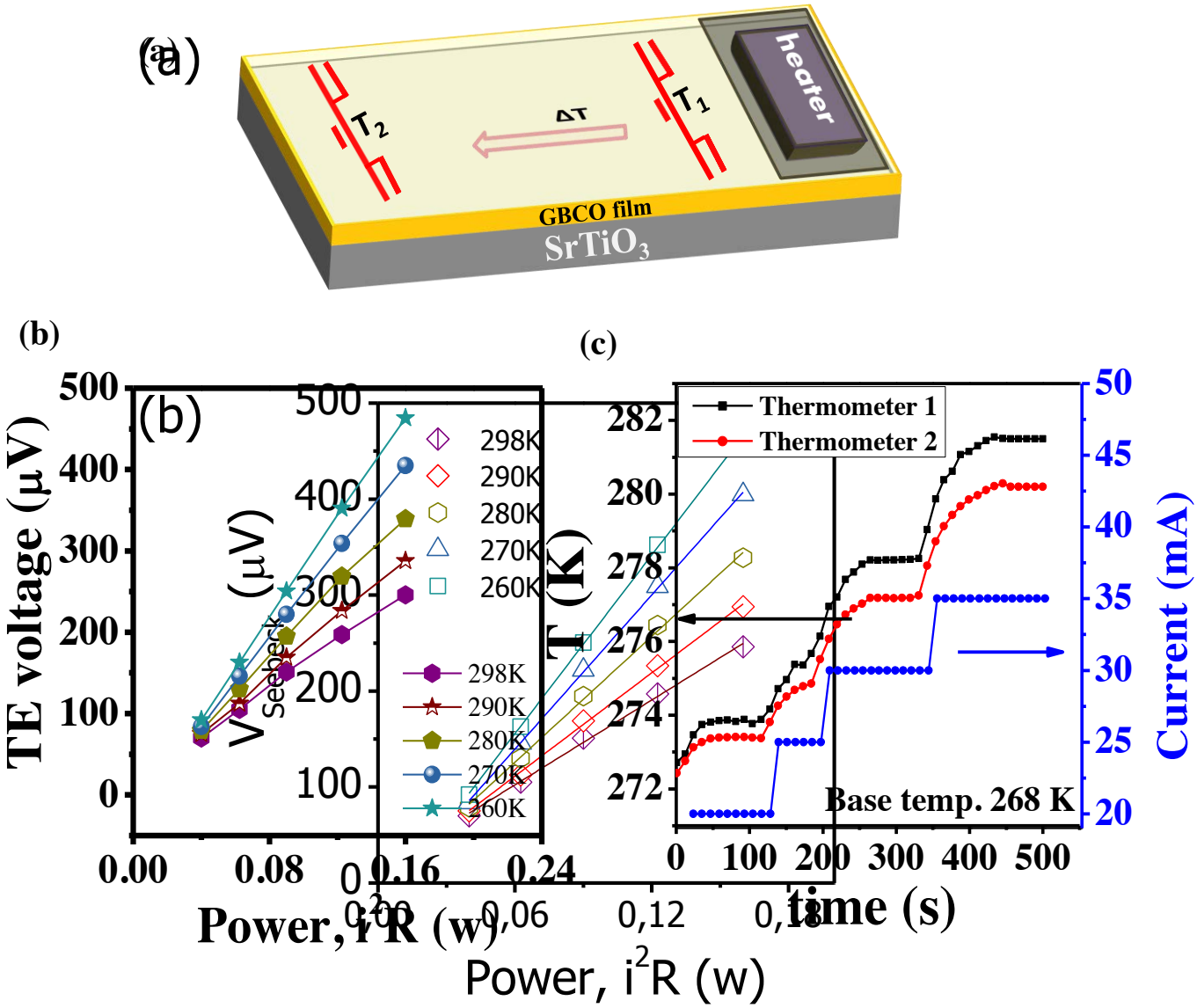

Figure 4.7 Seebeck effect measurements. (a) Schematic illustration of the set up used for Seebeck effect measurement of GBCO thin film on STO (001) substrate and, (b) thermoelectric voltage as a function of power at a fixed base temperature.

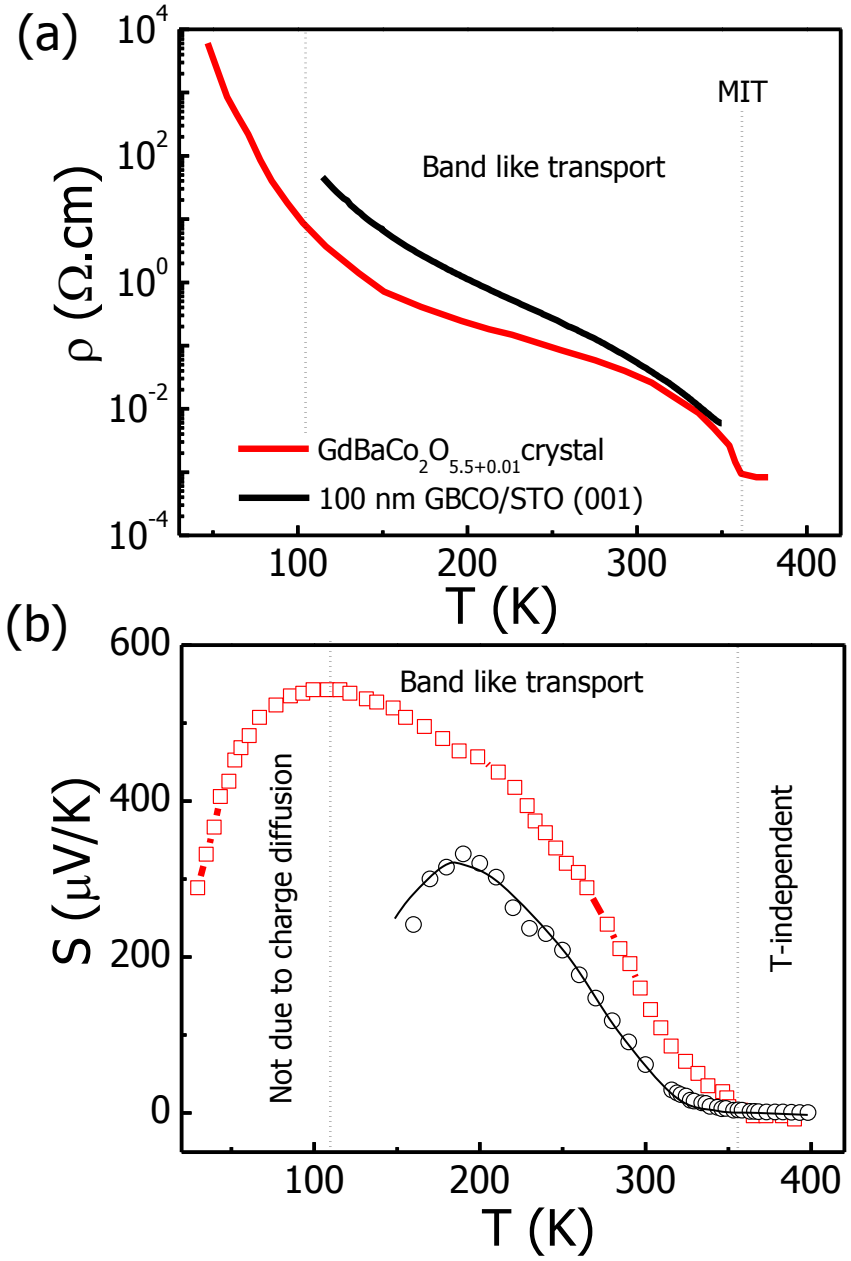

Figure 4.8 a) Comparison of resistivity of 100 nm GBCO thin film with bulk crystal of composition $GdBaCo_2O_{5.51}$, b) Comparison of Seebeck coefficient of 100 nm GBCO film (blue) with GBCO crystal of composition $GdBaCo_2O_{5.507}$. Crystal data were digitized from literature.[3]

Temperature dependent ρ (T) and S (T) of 100 nm GBCO film on STO (001) substrate is presented in Figure 4.8. The measured data is comparable with the reported data in the literature for GBCO crystals. ρ shows metallic behaviour above 360 K and it increases with decreasing

temperature down to 30 K for bulk crystal i.e. it shows a band-like transport. There is a metal to insulator transition (MIT) at 360 K in the bulk stoichiometric crystal. ρ of 100 nm GBCO film shows similar trend to the bulk crystals. ρ increases with decreasing temperature but MIT was not observed for the GBCO thin film within the measured range of temperature from 100 to 350 K.

From the literature, S (T) of the bulk crystal $GdBaCo_2O_{5.5+\delta}$ ($\delta > 0$) can be divided into 3 different regions as depicted in the red curve in Figure 4.8b (also comparable with thin film data): i) above MIT, S is negative and becomes temperature independent up to 400 K, ii) S becomes positive and increases sharply with decreasing temperature below 350 K, achieving maxima at around 100 K. S (T) from 250 to 100 K shows a band like behaviour and, iii) S decreases with further decreasing temperature below 100 down to 30 K.

In a band-like transport, ρ and S follow thermal activation behaviour and thus shows similar temperature dependence. Therefore, unlike semiconductors, both ρ and S are expected to follow a similar trend as it is observed in between 350 to 100 K. But, below 100 K, the trend is reserve i.e. ρ increases with decreasing temperature from 100 to 30 K but S decreases. Therefore, it can be said that S below 100 K is not due to charge carrier diffusion and is more likely governed by different mechanisms.

The high value of S at 100 K in GBCO crystals and its doping dependence (with variable δ content) have been explained in terms of spin-orbit degeneracy in addition to the Heike's formula as described below[3];

$$S_{T\to\infty} = -\frac{\kappa_B}{e}\ln\left[\beta.\frac{x}{1-x}\right] \qquad (1.21)$$

where, x is the number of electrons per unit cell, κ_B is Boltzmann constant, e is elementary charge and β represents the ratio of spin-orbit degeneracy of Co^{+3} and Co^{+4} ions. β=1, renders classical Heike's formula.[9] In general, a modified Heike's formula introduced by Koshibae et. al.[10], [11] is only applicable when S is temperature independent (in this case above 300 K). In the case of GBCO crystals, S around 100 K are not T-independent rather it shows strong temperature dependence up to 300 K. Furthermore, calculation of β in the case of GBCO crystals is complicated without the accurate knowledge of spin-states of cobalt ions present in the crystals which is discussed later.

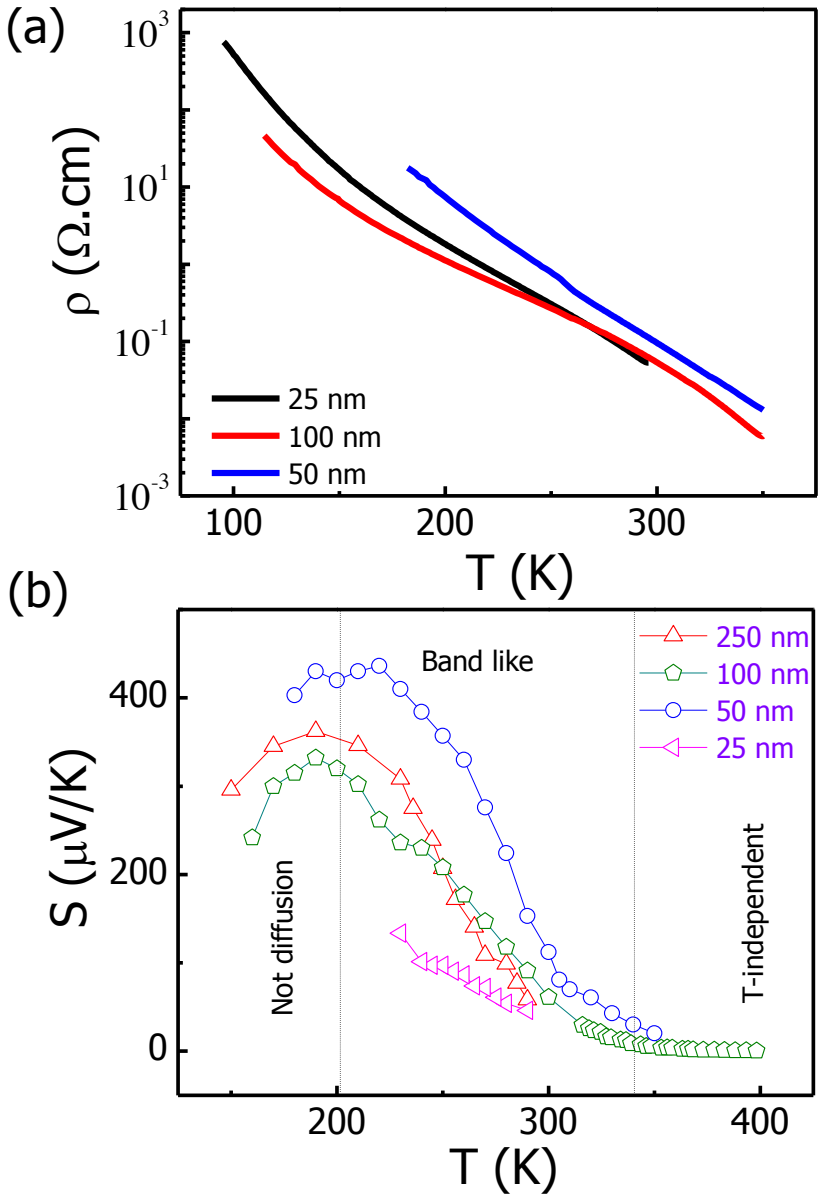

Figure 4.9 Thermoelectric transport properties of GBCO/STO films: (a) temperature dependent electrical resistivity and, (b) Seebeck coefficient of 25 to 100 nm films

Measurements as depicted in Figure 4.9 for GBCO films, show similar trends in ρ (T) and S (T) which are comparable to bulk crystals. ρ and S of 25 to 100 nm GBCO films are presented in Figure 4.9 and all films show similar temperature dependence of S and ϱ. S of all the films at 300 K is positive and acquires a small positive (+5 μV/K) value above 350 K. This indicates the presence of Co^{+3}/Co^{+4} ion pairs. S increases steeply with decreasing temperature from 300 to 200 K and achieves a maximum value of 450 and 300 μV/K for 50 and 100 nm films,

respectively. At 200 K. S decreases with further decreasing temperature showing a similar characteristics to bulk.

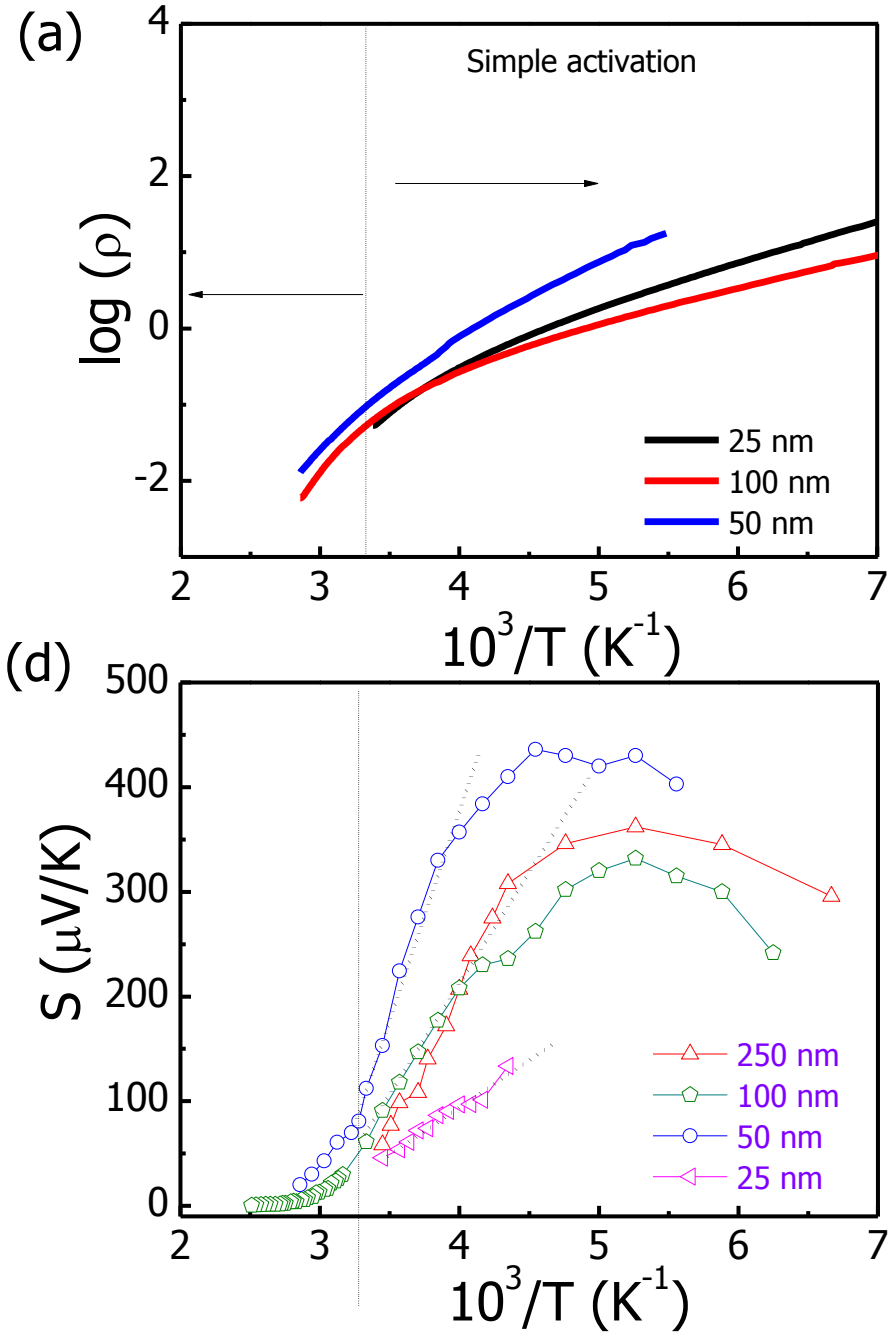

Figure 4.10 Thermal activation behavior of electrical resistivity and Seebeck coefficient of GBCO/STO films.

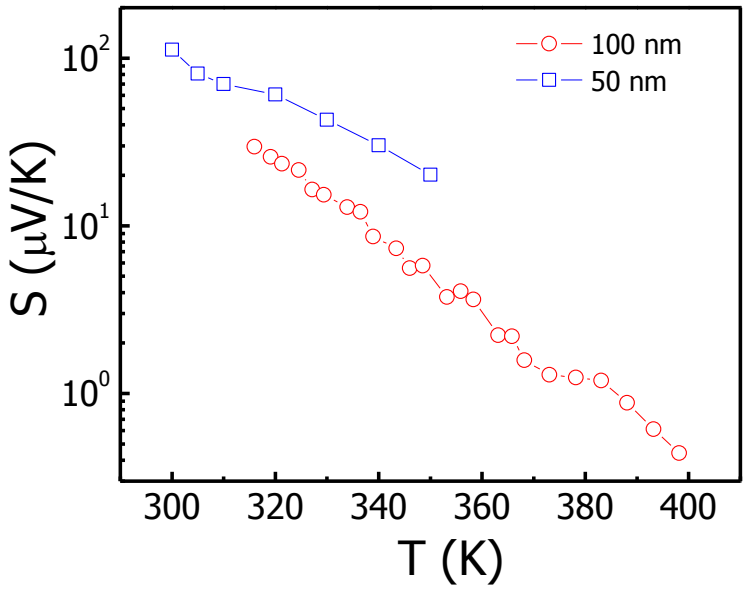

Figure 4.11 Temperature dependent Seebeck coefficient of 50 and 100 nm films within 300 K to 400 K.

In order to check the band-like transport of GBCO films between 350 to 200 K, *S* and log (ρ) were plotted against the reciprocal of temperature, as depicted in panels a and b in Figure 4.10. Clearly, resistivity and *S* do not show simple thermal activation behaviour within the temperature range measured. It is likely that different competing mechanisms are present depending of the temperature range as depicted in Figure 4.10b. It would be interesting to study this kind of competing scattering processes which might influence the thermoelectric response by means of Nernst effect as recently pointed out by Peijie Sun and Frank Steglich.[12], [13] However, this is beyond the scope of this chapter.

In the following paragraphs, temperature independent *S* of GBCO films above 300 K are discussed. *S* of thin film acquires a small positive (+5 μV/K) value above 350 K while bulk crystals acquires a small negative value (-4 μV/K) and it is temperature and doping independent. So, in thin film, holes are dominant carriers throughout the range of temperatures measured.

In a normal metal, one would expect a linear increase in the *S* with temperature.[13] However, in this study, *S* in the GBCO film is almost temperature independent in the metallic phase. A closer view of the *S* within 300 to 400 K shows that *S* deceases exponentially and it approaches zero as depicted in Figure 4.11. This is a clear indication of saturation of *S* and therefore, we assign this as the high temperature limit of thermopower of GBCO thin films.

High temperature S is given by modified Heike's formula as shown in equation 1.21.[11] As discussed in chapter 3, the high temperature limit of S can be calculated if β and *x* are known independently. Calculation of β for GBCO films is difficult for two different reasons. First, two different types of cobalt oxide coordination geometries exist in the CoO_2 layer of GBCO; CoO_5 pyramid and CoO_6 octahedral. For stoichiometric GBCO (where only Co^{+3} ions exist) these two coordination geometries are equal in number. However, whenever oxygen stoichiometry diverge from $\delta = 0.5$, the CoO_5 pyramid and CoO_6 octahedral form an equilibrium and the introduced holes (Co^{+4}) or electrons (Co^{+2}) in the CoO_2 layer will be distributed in the equilibrium which depends on the equilibrium constant (*K*) as shown in equation 4.2 and 4.3. Therefore, the degeneracy should be calculated as a combination of those octahedral and pyramidal sites as recently have shown by Taskin et. al.[3] as follows;

$$\beta = \frac{(g_{Oct}^{Co^{+2}})^m (g_{Py}^{Co^{+2}})^{1-m}}{(g_{Oct}^{Co^{+3}})^{1+m} (g_{Py}^{Co^{+3}})^{-m}} \qquad (4.2)$$

$$m = p + \left(y - \frac{1}{2}\right)\frac{dp}{dy}$$

$$p = \frac{\left\{\left(\sqrt{\left(\frac{K+1}{2}\right)^2 + 4(K-1)\left(\frac{1}{2} - y\right)y}\right) - \frac{K+1}{2}\right\}}{2(K-1)\left(\frac{1}{2} - y\right)}$$

$$K\,(T) = \frac{N_{Py}^{Co^{+2}} N_{Oct}^{Co^{+3}}}{N_{Oct}^{Co^{+2}} N_{Py}^{Co^{+3}}} \qquad (4.3)$$

where, '*m*' is a function of the probability, *p*, of finding electron in the equilibrium (*K* is the equilibrium constant depends on temperature governed by law of mass action). Assuming there are y numbers of octahedrons and $(1-y)$ numbers of pyramids, the expressions of β for Co^{+2}/Co^{+3} mixed states will be. $N_{Py}^{Co^{+2}}$, $N_{Oct}^{Co^{+3}}$, $N_{Oct}^{Co^{+2}}$ *and* $N_{Py}^{Co^{+3}}$ are number of ions concentrations in the corresponding crystal sites in equilibrium, respectively. Similar expressions can be calculated for Co^{+3}/Co^{+4} mixed valence. Therefore, without knowing the exact oxygen stoichiometry of the GBCO thin films, this calculation cannot be performed in the case of the GBCO film.

Secondly, octahedral and pyramid co-ordinations geometry offer different spin states of cobalt ions, as shown in Figure 4.12. At low temperatures, it is believed that Co^{+3} ions have a low spin (LS) state in octahedrals and an intermediate state (IS) in pyramids for stoichiometric

crystals. At increasing temperatures, around the MIT, Co ions in octahedral sites undergo a selective spin state transition from LS to high spin (HS) states.[1] Interestingly, the IS state in pyramids does not change. However, there are other reports showing that the existence of LS, HS and IS Co^{+3} is possible in GBCO crystal.[14] For electron or hole doped systems, it would be even more complicated to determine the spin states of Co^{+4}, Co^{+2} and Co^{+3} ions before and after MIT. Thus, the insufficient knowledge of the spin states of cobalt ions will provide unphysical values of the spin-orbit degeneracy.

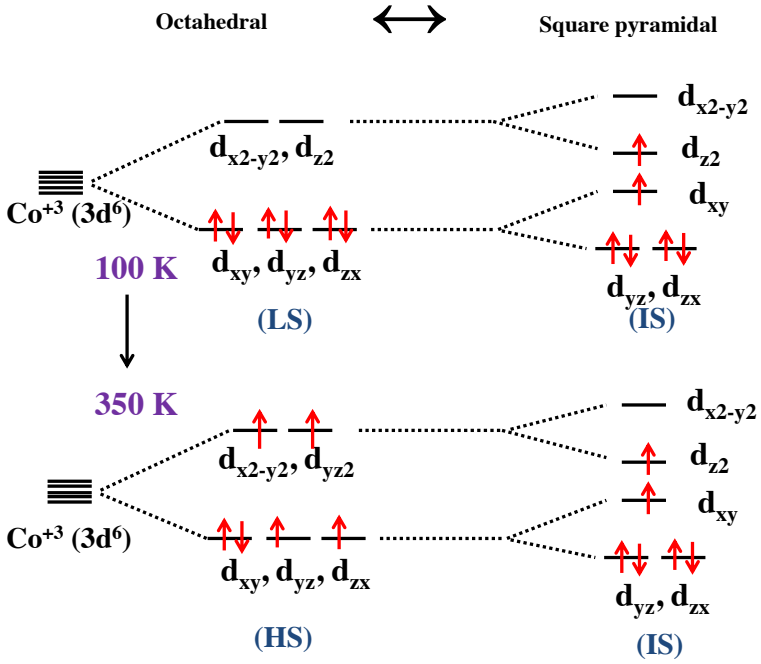

Figure 4.12 Schematic illustrations of the selective spin-state transition of Co^{+3} ions in GBCO crystal.

It is reported in the literature[15] and was shown in Chapter 3 that the room temperature S of misfit cobaltates can be better understood without the spin-orbit degeneracy, β factor at 300 K. Therefore, for the calculation of S of GBCO films we assume a similar behaviour neglecting the β factor and at the same time the above mentioned complications are avoided. Thus, we stick to the classical Heike's formula for the high temperature limit of S, assuming β = 1 as shown below where the only variable is *x*;

$$S_{T\to\infty} = -\frac{\kappa_B}{e}\ln\left[\frac{x}{1-x}\right] \qquad (1.18)$$

It was shown in Figure 4.11 that S acquired very small values between 300 to 400 K and it approached almost zero at 400 K. Equation 1.18 shows that approaching zero S means '*x*' should approach to its limit, which is ~0.5, unless it shows crossover ($x > 0.5$) and thus change the sign of S. For clarity, see the Figure 2.11 in chapter 2, where a variation of S with *x* was plotted for both electron and hole doped samples. But, the sign of S for GBCO films is positive throughout the range of temperature we measured (See Figure 4.9b and 11). Therefore, we eliminated the possibility of exceeding *x* over 0.5.

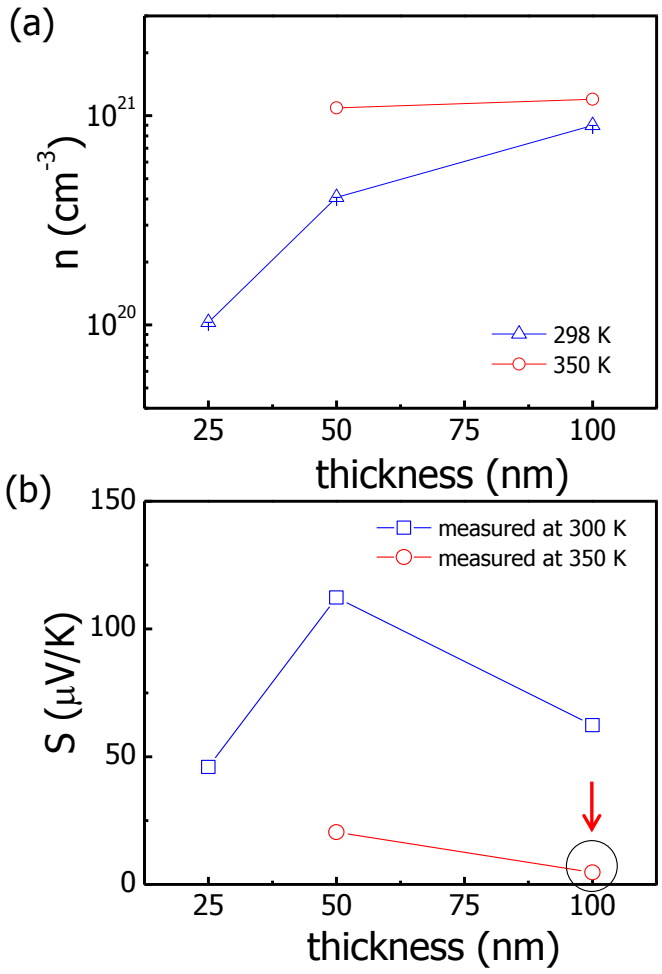

Figure 4.13 Seebeck and Hall effect measurements: (a) measured Hall electron density and, (b) measured Seebeck coefficients of the GBCO thin films at 300 K and 350 K. Data point indicated by circle and arrow is approaching to zero.

Heike's formula is based on the assumption that two particles cannot occupy the same available state and therefore in equation 1.18, *x* represents the number of electrons per unit cell. Therefore, *x* can be calculated, via equation 1.18, from the measured S within the temperature

range from 300 to 400 K where a high temperature limit of *S* is considered. Interestingly, number of electrons per unit cell can also be calculated from electron density measured by Hall effect. It would be interesting to check whether calculated *x* from Hall effect and Seebeck effect coincide or not which would further validate the true high temperature limit in the case of GBCO films. Figure 4.13 depicts the measured Hall electron density and *S* at 300 and 350 K. In addition, Figures 4.14 depicts the variation of *S* as a function of filling control at a fixed size of polarons obtained from Heike's formula. Therefore, the validity of Heike's formula in the case of GBCO films can be tested.

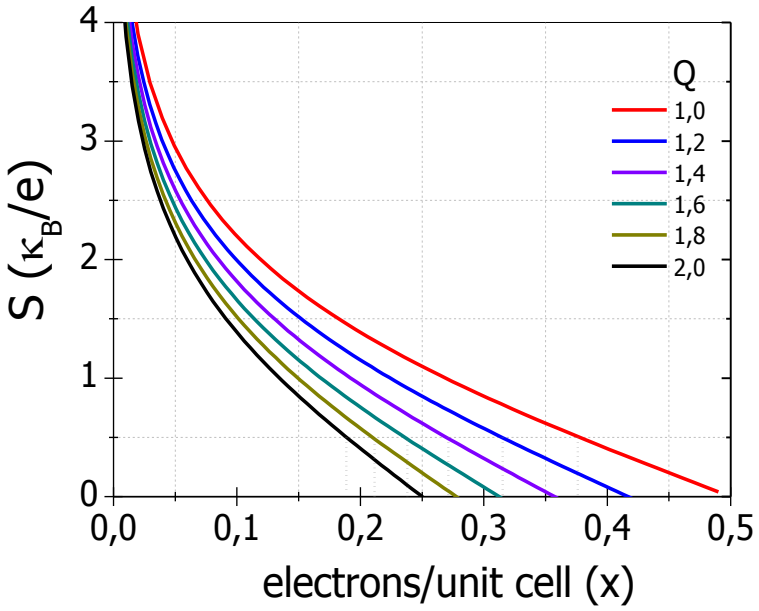

Figure 4.14 Seebeck coefficient as a function of filling control with variable size of polarons obtained from Heike's formula.

Figure 4.13 depicts the Hall electron density (*n*) and *S* of the thin films measured at 300 K and 350 K. the number of electrons per unit cell (*x*) in GBCO films was calculated from the Hall electron density (*n*) by multiplying it with the unit cell volume (unit cell volume of GBCO is 229.8 $Å^3$) while *x* was calculated from *S* by using equation 1.18. Calculated *x* for all the films at 300 and 350 K is summarized in Figure 4.15a. At first, the calculated *x* for 100 nm film at 350 K is very close to 0.5 (highlighted by red circle and arrow). As described before (and also highlighted in Figure 4.13b by the red circle and an arrow), classical Heike's formula shows that if *S*

approaches to zero then *x* approaches to 0.5. This is exactly what can be observed. Therefore, Heike's formula is valid at 350 K for the GBCO films. But, the calculated *x* from S and *n* do not coincide for any of the film thickness except for the 50 nm thick film at 300 K, where the value are very close to each other. This observation indicates some hidden characteristics that we have not yet considered.

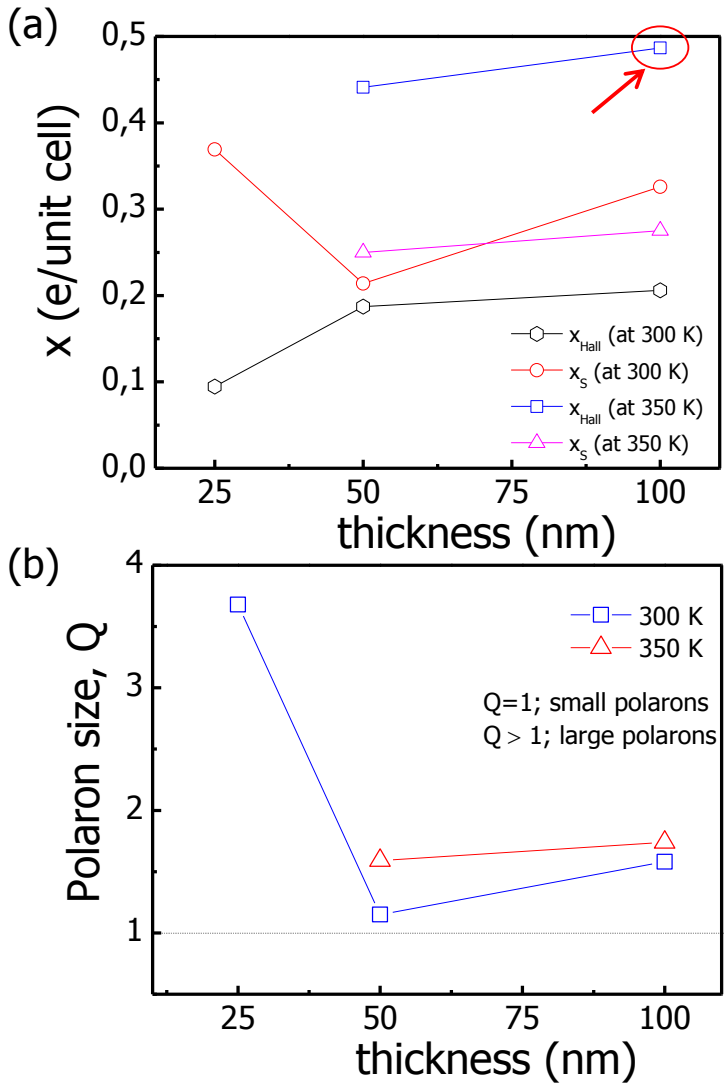

Figure 4.15 Calculation of the number of electrons per unit cell (*x*): (a) calculated x from Hall electron density and Seebeck coefficient and (b) calculated polaron size at 300 K and 350 K for GBCO thin films.

More accurately, *x* in Heike's formula represents the ratio of the particle to the available sites. As described before, Heike's assumption was that two particles cannot occupy the same available sites. Thus *x* can be represented as the number of particles (electrons in this case) per

unit cell. However, if the situation deviates from this scenario i.e., if electrons share different available sites, then Heike's formula can be written in the form below, as shown in detail in chapter 1;

$$S_{T\to\infty} = -\frac{\kappa_B}{e}\ln\left[\frac{Q.x}{1-Q.x}\right] \qquad (1.19)$$

where the parameter Q is the description of polaron size (see chapter 1 for details).[16] Recently, this has been pointed out by P. L Bach et al[17] in case of $La_2NiO_{4-\delta}$ films. However, if we incorporate the possibility of diffusion through largely interacting localized states (polarons) and use equation 1.19 which defines Q as measure of the polaron size and calculate the corresponding Q values that matches the experimental values obtained from S and *n*, one obtain Q values of ~ 1.5 for 50 and 100 nm films at 300 and 350 K, respectively. These calculations provide information about the existence of large polarons. However, Q value obtained for 25 nm film is ~ 3.8. Such a high Q for 25 nm film might indicate that S has not reached yet the limit for this film.

4.4 High temperature thermopower measurements

Simultaneous thermopower and electrical resistivity measurements were performed at high temperatures by a standard four probe method in a LINSEIS instrument which is originally intended for bulk samples. Large substrate dimensions were used (shown in chapter 3, Figure 3.9b) to grown thin film (10×5 mm^2×250 nm). Two copper clips were used to hold the films vertically necessary for the electrical contacts. Measurements were performed from 350 to 757 K in a helium atmosphere. This set up could have been adapted to measure in an O_2-atmosphere[18] but this would have implied replacing the ceramic pieces and heating elements which we did not do it. Still, if there had been any irreversible loss of oxygen in the sample after heating in helium atmosphere we would have readily observed it in the resistivity. The heating and cooling data is not reversible for the 250 nm thick GBCO film grown on STO (001) as shown in Figure 4.16. Therefore, we will not discuss high temperature thermoelectric properties of the GBCO films grown on STO (001).

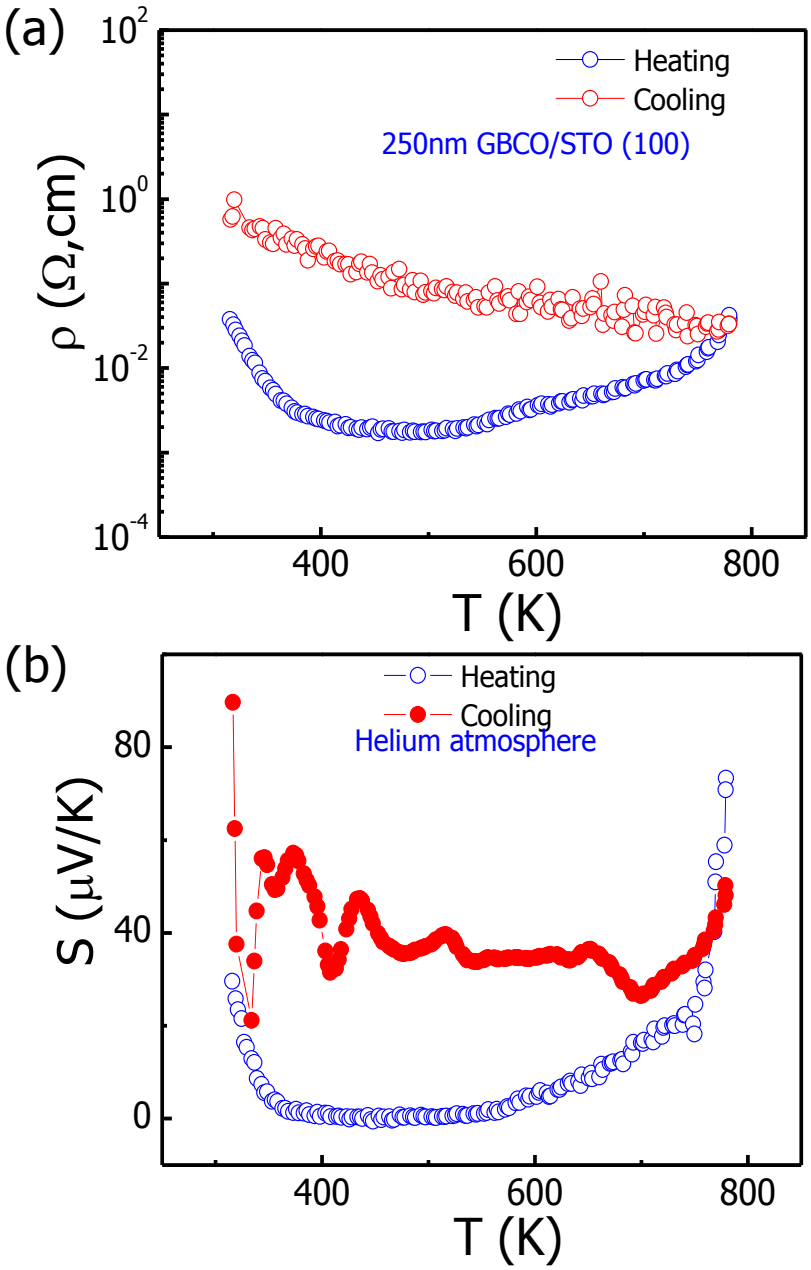

Figure 4.16 Simultaneous high temperature electrical resistivity and thermopower measurements of GBCO/STO (001) film of dimension 250 nm×5mm×10 mm in LINSEIS instrument.

4.5 Summary:

In summary, we have grown high quality epitaxial GBCO films on STO (001) by PLD technique. The GBCO films grow coherently with STO (001) substrates and the films are highly c-axis oriented. The in-plane thermopower measurements near the metal-insulator transition show the existence of large polarons. Therefore, we conclude that thermopower of GBCO film at 300K or above is governed by the incoherent motion of electrons.

Bibliography:

[1] C. Frontera, J. L. García-Muñoz, A. Llobet, M. A. G. Aranda, *Phys. Rev. B* **2002**, *65*, 180405.

[2] N. Ishizawa, T. Asaka, T. Kudo, K. Fukuda, A. Yasuhara, N. Abe, T. Arima, *Chem. Mater.* **2014**, *26*, 6503–6517.

[3] A. A. Taskin, A. N. Lavrov, Y. Ando, *Phys. Rev. B* **2006**, *73*, 121101.

[4] A. A. Taskin, Y. Ando, *Phys. Rev. Lett.* **2005**, *95*, 176603.

[5] V. Pardo, D. Baldomir, *Phys. Rev. B* **2006**, *73*, 165117.

[6] A. Maignan, V. Caignaert, B. Raveau, D. Khomskii, G. Sawatzky, *Phys. Rev. Lett.* **2004**, *93*, 26401–1.

[7] R. Seikh, Motin and Bernard, *B. Chapter*, *Cobalt Oxides From Cryst. Chem. to Phys.* **2012**, *Chapter 3*, 129.

[8] T. C. Koethe, *PhD ThesisUniversitat zu Koln* **2007**, 1–97.

[9] P. M. Chaikin and G.Beni, *Phys. Rev. B* **1976**, *13*, 647.

[10] W. Koshibae, S. Maekawa, *Phys. Rev. Lett.* **2001**, *87*, 236603.

[11] W. Koshibae, K. Tsutsui, S. Maekawa, *Phys. Rev. B* **2000**, *62*, 6869–6872.

[12] P. Sun, F. Steglich, *Phys. Rev. Lett.* **2013**, *110*, 1–5.

[13] P. Sun, B. Wei, J. Zhang, J. M. Tomczak, A. M. Strydom, M. Søndergaard, B. B. Iversen, F. Steglich, *Nat. Commun.* **2015**, *6*, 1–5.

[14] N. A. S. Roy, M. Khan, Y. Q. Guo, J. Craig, *Phys. Rev. B* **2002**, *66*, 220405.

[15] B. Rivas-murias, J. M. Vila-fungueiriño, F. Rivadulla, *Sci. Rep.* **2015**, DOI: 10.1038/srep11889.

[16] E. Winkler, F. Rivadulla, J. S. Zhou, J. B. Goodenough, *Phys. Rev. B - Condens. Matter Mater. Phys.* **2002**, *66*, 944181–944184.

[17] P. L. Bach, V. Leborán, E. Ferreiro-vila, B. Rodríguez-gonzález, *APL Mater.* **2013**, *1*, 21101.

[18] P. Brinks, N. Van Nong, N. Pryds, G. Rijnders, M. Huijben, *Appl. Phys. Lett.* **2015**, *106*, 143903.

Chapter 5: Effect of the epitaxial strain on the thermoelectric properties of $GdBaCo_2O_{5.5\pm\delta}$ thin films

Epitaxial strain plays an important role in tuning electronic structure and hence the physical properties of the thin films. The effect of substrate induced epitaxial strain on the thermoelectric properties of $GdBaCo_2O_{5.5\pm\delta}$ thin films is presented in this chapter. Films under compressive strain provide evidence of the incoherent motion of charge carriers, which is reflected in their temperature dependent thermopower from 200 to 300 K.

5.1 Introduction

The interplay between spin, charge, lattice symmetry and orbital degrees of freedom are the heart of many fascinating properties observed in transition metal oxides such as multiferroicity,[1],[2] superconductivity,[3] and colossal magnetoresistance.[4] The implementation of many devices often requires the deposition of thin films of these materials. The lattice parameters and the symmetry of a substrate (which is required to deposit the films) do not always match with the lattice parameter of the film. However, strain engineering (or lattice mismatch) is often used to tune and/or explore unexpected physical properties. This strategy can be used in different possible ways. For example, i) the use of strain, induced by different single crystal substrates, provides access to a new rich phase diagram of transition metal oxides,[5] ii) the use of a buffer layer at the interface of two different films having different physical properties;[6] iii) the growth of thin film superstructures (or heterostructure) in which the interface between the two layers plays an important role, for instance, the lowering of thermal conductivity, which is useful to generate highly efficient thermoelectric materials.[7]

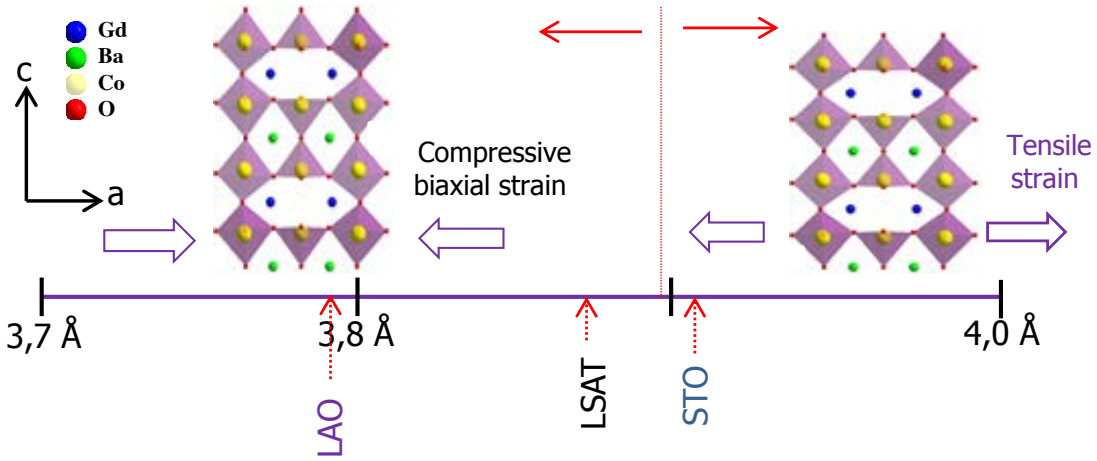

Figure 5.1. Schematics illustration of the expected deformation of the crystal structure of GBCO film under tensile and compressive strain if c-axis oriented films grow coherently on STO (001), LSAT (001) and LAO (001) substrates.

For this reason, we chose three substrates with different cell parameters where GBCO is expected to grow coherently with the aim of exploring the effect of stress on the thermoelectric properties.

Figure 5.1 depicts schematically the expected effect of epitaxial stress on the crystal structure of GBCO thin films. The growth of GBCO thin films on STO (001) substrates is presented in Chapter 4 where it was observed that thicker films release their strain to achieve the bulk lattice parameters. In order to introduce substrate induced epitaxial strain on the thin film lattice, the film is expected to grow coherently i.e., fully strained with the substrate. It was observed before that 10 to 25 nm GBCO films were fully strained with STO (001) substrate. Above the thickness of 50 nm, relaxation started to appear (see for instance Figure 4.4 in chapter 4).

Table 5.1 Calculation of the expected in-plane strain of c-axis oriented GBCO film if they grow coherently with the substrates.

Film/substrate	In-plane area (Å^2)	Effective in-plane (Å)	Mismatch (%)
GBCO/STO (001)	15.249	3.905	+0.20
GBCO/LSAT (001)	14.796	3.870	−0.69
GBCO/LAO (001)	14.250	3.790	−2.74 (ab_LAO)
GBCO crystal	15.193 (ab-plane)	3.897	−1.78 (bc_LAO)
	14.894 (bc-plane)	3.859	−0.86 (ac_LAO)
	14.621 (ac-plane)	3.823	

The bulk lattice parameters of the stoichiometric GBCO crystal are $a = 3.862$ Å, $b/2 = 3.934$ Å and $c/2 = 3.786$ Å. The effective in-plane parameter was calculated from the square root of the in-plane area. The in-plane parameter of STO (001) substrate is 3.905 Å.

$$\text{Mismatch (\%)} = \frac{\left(a_{film}^{epitaxy} - a_{bulk}^{effective}\right)}{a_{bulk}^{effective}} \times 100 \qquad (5.1)$$

Calculation of the in-plane area mismatch of the films and bulk GBCO crystals in Table 5.1 shows that GBCO/STO (001) film expands in the in-plane direction and thus the out-of-plane shrinks. Therefore, the 25 nm GBCO film on STO (001), presented in chapter 4, is under effective tensile strain (+0.20 %). Two other single crystal substrates with perovskite structure were chosen namely LSAT (001) and LAO (001) whose in-plane lattice parameters are 3.87 Å and 3.790 Å, respectively. If the GBCO were to grow coherently along the c-axis in LSAT and LAO

substrate, it would be subject to a compressive strain of −0.69% and −2.74%, respectively. Interestingly, the c-parameter of GBCO and a-parameter of LAO are very close to each other. Therefore, if GBCO film grows along b-axis (or a-axis) on LAO (001), it will be subject to a compressive strain of −0.86 % (or −1.78%).

5.2 X-ray diffraction

25 nm GBCO films were grown on LAO (001), LSAT (001) and STO (001) substrates by the PLD technique following the same conditions as those described in chapter 4. Figure 5.2 depicts the standard 2θ/ω patterns of the GBCO films grown on the above mentioned substrates. All three films show half-order reflections. A systematic left shift in 2θ of the (001) and (002) reflection indicates that the out-of-plane parameters of the films increases while moving from STO → LSAT → LAO (001). Furthermore, the relative intensities of (001) → (002) reflections decreases (shown in Table 5.2) from STO → LSAT → LAO (100). The intensity of the half-order reflections along the c-axis is generally related to the contrast in the Gd/Ba ratio, while along the b-axis, the half-order reflections correspond mostly to the oxygen vacancy arrangements. Therefore, it is likely that either the films under tensile or compressive strains deviate from the stoichiometry or it shows mixed c/a-or b-axis orientation. For GBCO/LAO, the half-order reflection will be (0k0) in the case if it grows along b-axis.

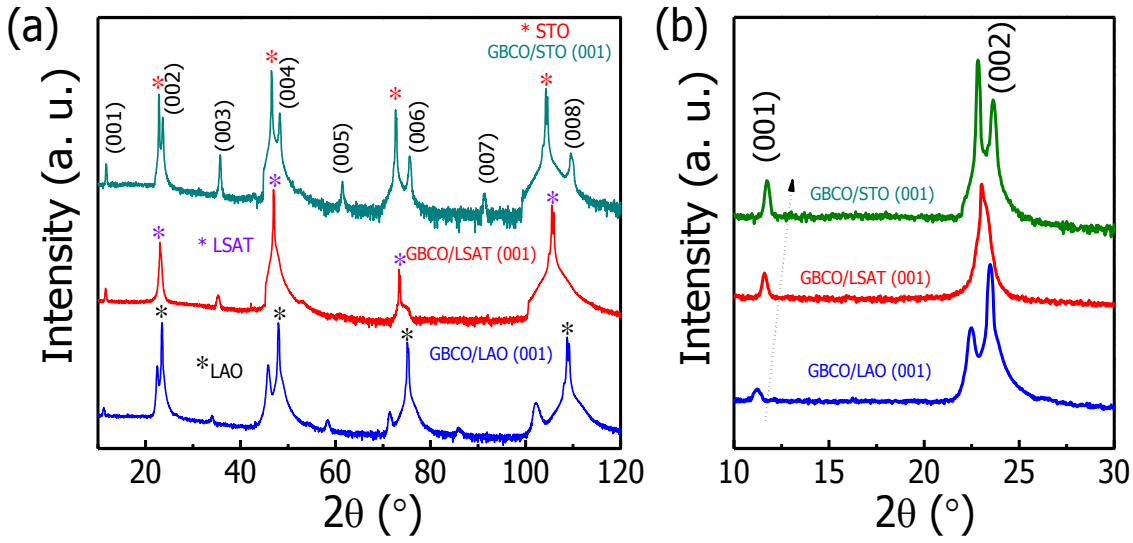

Figure 5.2 X-ray diffraction (XRD) patterns: (a) Standard 2θ/ω patterns of GBCO film grown on STO (001), LSAT (001) and LAO (001). (b) Zoomed XRD patterns from 10° to 30° in 2θ.

Table 5.2 Relative intensities of the (001) reflection to (002) reflection of the GBCO films grown on STO (001), LSAT (001) and, LAO (001) substrates.

Film/substrate	$I_{relative} = \frac{I_{001} - I_{base}}{I_{002} - I_{base}}$
GBCO/STO (001)	0.0125
GBCO/LSAT (001)	0.016
GBCO/LAO (001)	0.008

The in-plane cell parameters of GBCO films grown on different substrates can be inferred from reciprocal space maps (RSMs) performed around (−303), (−303) and (−103) reflections of STO, LSAT and LAO substrates, respectively, as depicted in Figure 5.3. Indexing the GBCO reflection for GBCO/LAO as (−103) is an over simplification. For c-axis orientation, −103 reflection is infact (−106)/(0−26) while for b-axis orientation, it would be (302).

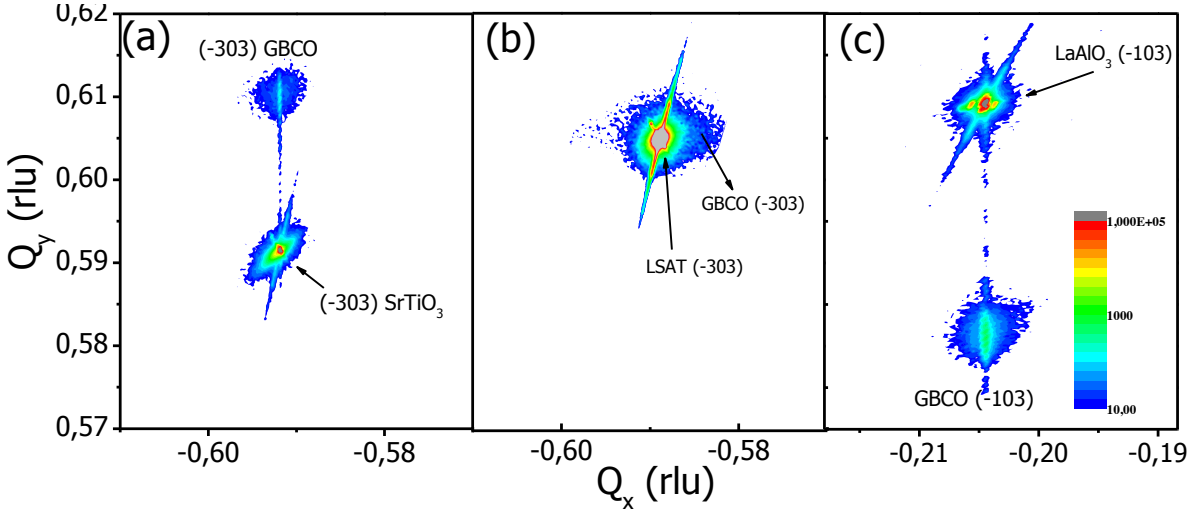

Figure 5.3 RSMs of GBCO film grown on STO (001), LSAT (001) and LAO (001) substrates. GBCO films are fully strained with all the substrates.

As can be observed in Figure 5.3, all the films are perfectly epitaxial with the substrates as the in-plane parameters of the thin films match perfectly with the substrates. The Q_y parameter is inversely related to the out-of-plane parameter and it decreases from

STO→LSAT→LAO meaning that the out-of-plane parameter increases, which is consistent with the standard 2θ/ω measurements.

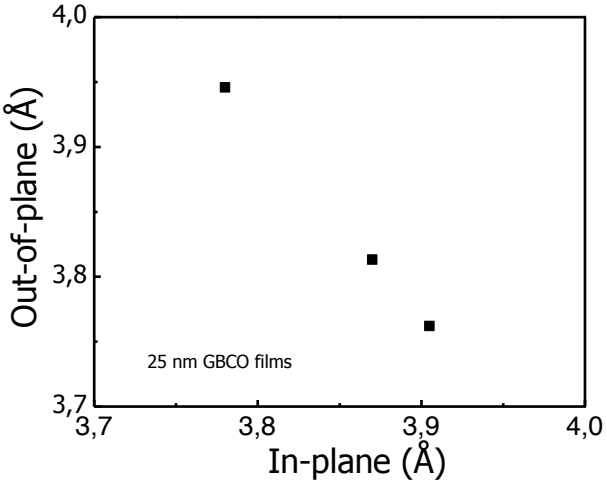

Figure 5.4 Lattice parameters of GBCO thin film grown on STO (001), LSAT (001) and LAO (001) substrate.

Interestingly, none of the GBCO films released their strain to achieve bulk parameters. This is an indication that the chosen thickness of ~25 nm is below the critical thickness for strain relaxation for all substrates. If the films released their strain to achieve bulk lattice parameters, one would expect a clear splitting of the in-plane parameters. (as was observed for 100 nm GBCO film on STO (001), Figure 4.4), especially in case of GBCO grown on LAO (001). Although, it is more probable to have a-(or b/2-) axis oriented GBCO film on LAO (001), but surprisingly the films shows intense half-order reflections (odd 00*l* reflections) which led us to consider it first as a c-axis oriented film. In this case, the odd reflections (00*l*) obtained in the 2θ/ω patterns would be related to the oxygen vacancy ordering along the a-axis or mixed domains of c- and b-axis orientations. It will be surprising to achieve reflections from oxygen vacancy ordering of 25 nm thin GBCO films from a standard X-ray diffractometer, since, the X-ray scattering factor of oxygen atom is very weak, unless the oxygen vacancy arrangement also changes the position of the large cations producing a subsequence b-axis doubling. High resolution cross section transmission electron microscopy (TEM) analysis will provide more insights of the film microstructure and orientations. RSM of (-303) reflections of GBCO and LSAT overlap with each other. This indicates that the in-plane and out-of-plane parameters of GBCO on LSAT are close to those of the LSAT substrate. GBCO film on LSAT substrate is almost a cubic crystal. Information about the structure of GBCO film on different substrates, obtained from X-ray

diffraction analysis is summarized in Figure 5.4. From XRD data, it can be stated that GBCO film is under tensile strain (+0.18 %) on the STO (001), while it is under compressive strain (-0.71 %) on the LSAT.

5.3 Transmission electron microscopy (TEM) results

Detailed transmission electron microscopic (TEM) observations of the 40 nm thick GBCO film grown on STO (001), LSAT (001) and LAO (001) are depicted in Figure 5.5, 5.6 and 5.7. The main part of the GBCO/STO (100) film is free from defects (Figure5.5a). There is a clear contrast between horizontal rows with high and low brightness dots forming a sequence every two perovskite blocks along the vertical direction. This is an indication of the perovskite doubling along the c-axis. Therefore, the GBCO film is perfectly epitaxial and c-axis oriented. Some inclusions were observed at the interface which is not shown here.

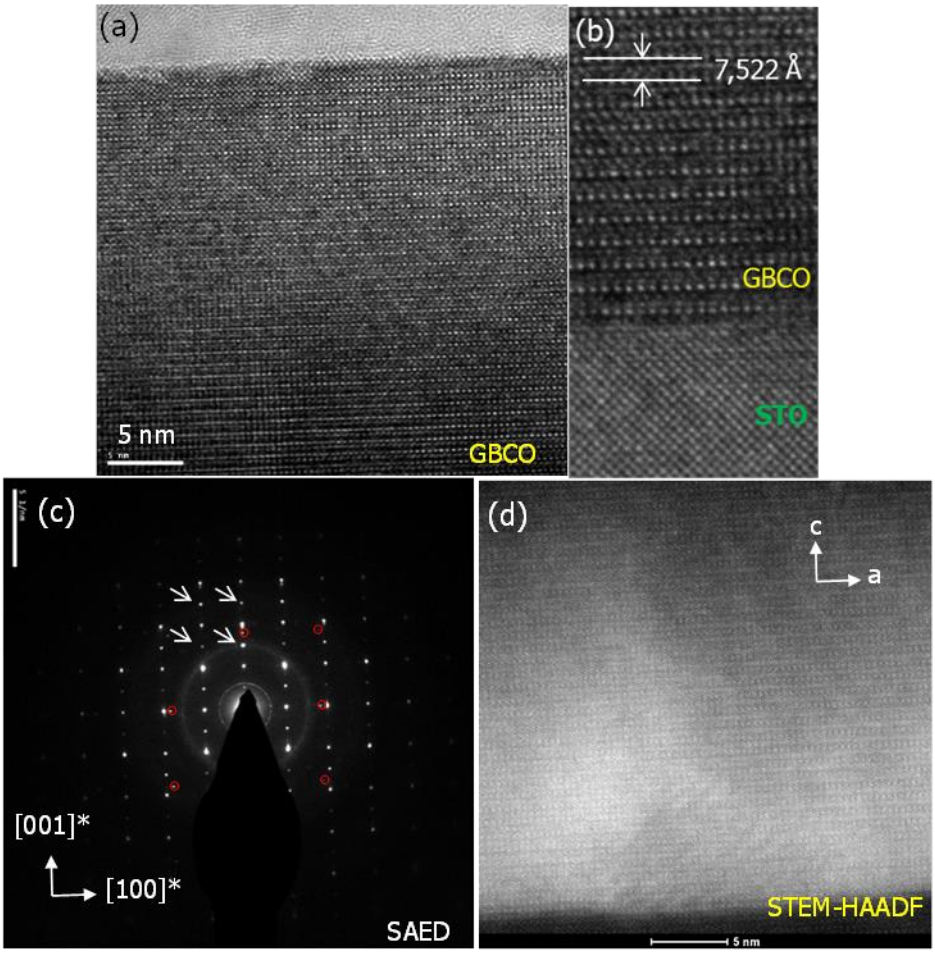

Figure 5.5 TEM observations of ~40 nm thick GBCO film grown on STO (001) substrate. (a) HRTEM, (b) HRTEM of GBCO-STO interface, (c) SAED patterns and, (d) STEM-HAADF image. All images shows cation ordering perpendicular to the surface of the substrate.

The pure c-axis orientation of the film is further demonstrated by the appearance of the half-order peaks (marked by white arrows in the SAED in Figure 5.5c), characteristics of c-axis doubling which means the ordering of Gd and Ba cations along the c-axis parallel to the growth direction. Some other peaks of relatively large cell parameters can be observed (marked in red circles) and they might originate from the inclusions. The sequence of the cations ordering along c-axis is also apparent from STEM-HAADF image (Figure 5.5d).

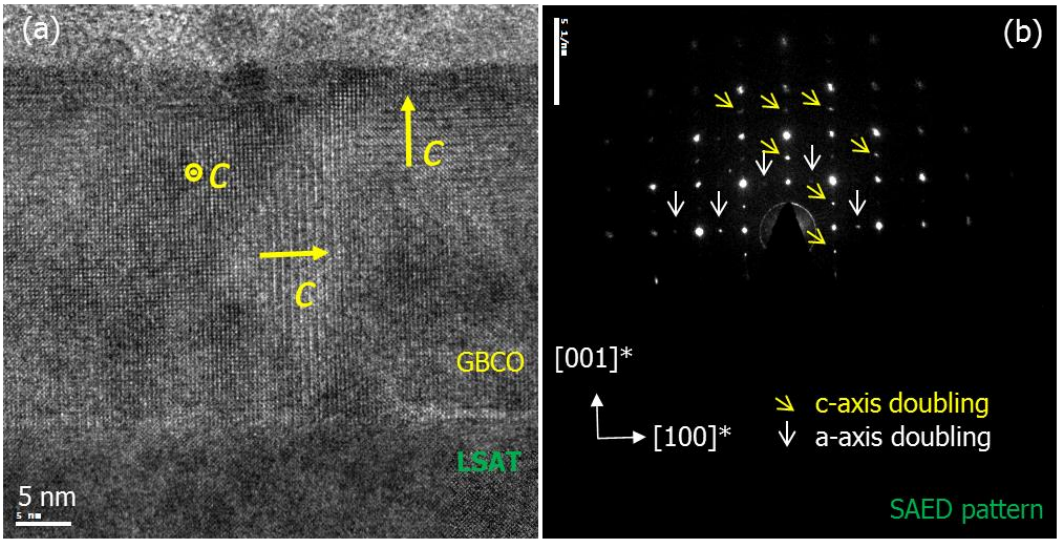

Figure 5.6 TEM observations of ~40 nm thick GBCO film grown on LSAT (001) substrate: (a) HRTEM image and, (b) SAED pattern. All images shows cation ordering perpendicular and parallel to the surface of the substrate. GBCO/LSAT (001) film is mixed c- and a-axis oriented.

Figure 5.6 shows the cross section of the GBCO/LSAT film also in [100] zone axis. A contrast of bright and dark dots evidences the doubling of perovskite along c-axis. In this case, regions with horizontal and vertical alignments are clearly visible. This has been attributed to the coexistence of mixed c- and a-axis oriented domains. The image also shows some regions where no doubling is observed, which either can correspond to single perovskite (no doubling) or more likely to double perovskite domains with c-axis orientation perpendicular to the image, thus showing an a-b plane. The main part of the GBCO/LSAT (001) film consists of mixed c- and a-axis oriented domains (Figure 5.6a). The compact arrangement of $c_{\parallel}$ (c-parallel) and $c_{\perp}$ (c-perpendicular) oriented domains of a few nanometre size without substantial perturbation at the boundaries is an indication that a, b and c/2 are very close to each other. This result is consistent

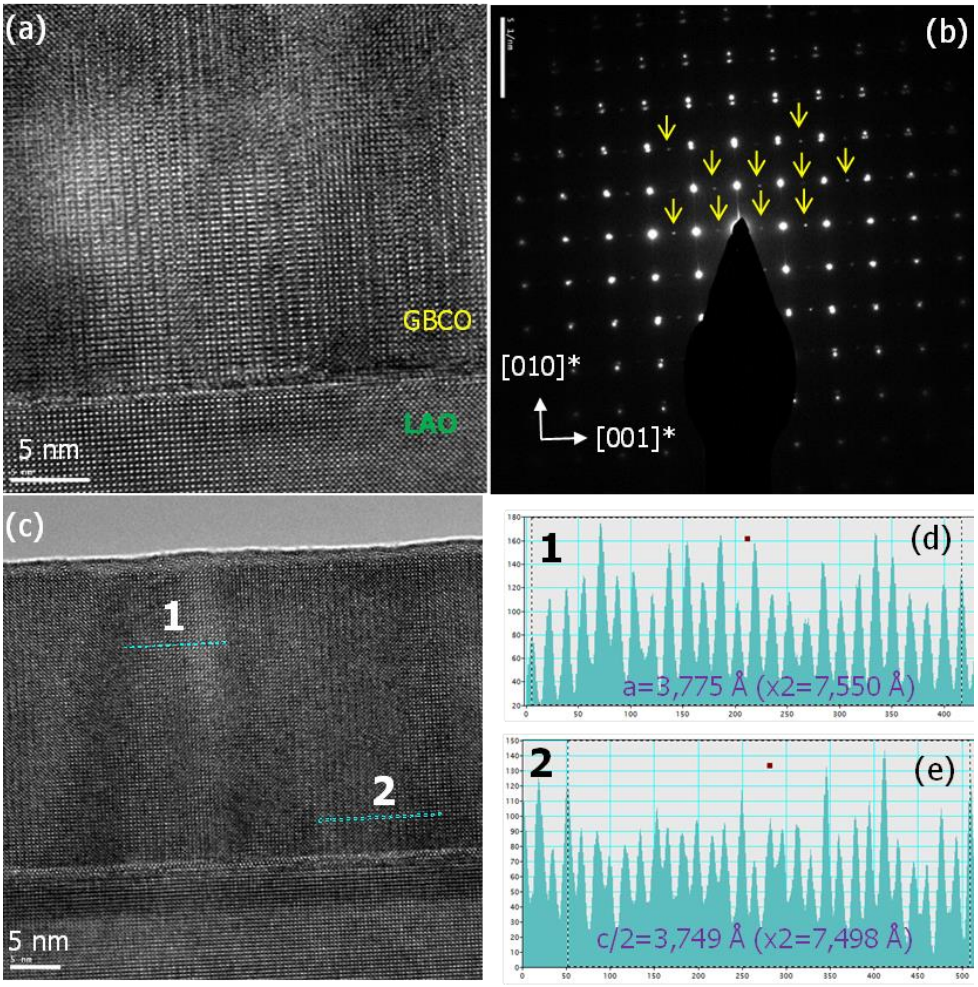

Figure 5.7 TEM observation of 40 nm thick GBCO film grown on LAO (001) substrate: (a) HRTEM at the interface of Lao and GBCO, (b) SAED. The line profile (d) and (e) taken from HRTEM image in panel c. Some domain shows cation ordering parallel to the surface of the substrate bot others do not show.

with the previous XRD measurements of the same sample where no evidence of GBCO film reflection splitting was observed in RSMs (see Figure 5.3). The SAED pattern of the same region (Figure 5.6b) shows half-order reflections corresponding to c-axis doubling in both vertical (yellow arrows) and horizontal (white arrows) directions.

The GBCO/LAO (001) film shows a perfect epitaxial arrangement, also free of defects (Figure 5.7a). Regions with clear doubling alternate with regions without doubling. In this case, the regions with double periodicity evidence $c_{\parallel}$ (or a/b-axis perpendicular orientation). No trace of domain with $c_{\perp}$ was observed in this case. The regions with no periodicity are attributed to $c_{\parallel}$

domains with c-axis pointing perpendicular to the image, as in the previous film of GBCO/LSAT. The SAED in Figure 5.7b shows half-order reflections. Lattice parameters were extracted from the mean distance of the intensity profile periodicity of the image along a line scan. A reference line scan was taken at the LAO substrate with a = 3.790 A periodicity (see Figure 5.7b and c). The periodicity in line scan 1 and 2 could then be measured to be 3.775 Å and 3.749 Å, respectively, corresponding to a- and c/2-parameters close to the bulk GBCO. It is noticeable that despite the line scan 2, taken at a very close distance to the film-substrate interface it already shows non-strained values of a-axis (substrate $a_{LAO} = 3.790$ Å). It is very likely that in this case the film strain is released by the formation of large density of defects at the interface (misfit dislocations) which may correspond to the contrast in Figure 5.7a.

Although no trace of the c-axis oriented domains was found in 40 nm thick GBCO/LAO (001) film, relatively intense (001, 003, etc) odd symmetric reflection in 25 nm thick films were observed in standard XRD measurements (Figure 5.2) which might be an indication of Gd/Ba ordering along the c-axis. In order to explain this discrepancy, we can assume that a relatively smaller fraction of volume is still c-axis oriented atleast in case of the 25 nm thick GBCO film on the LAO (001).

5.4 Electronic transport properties

The electrical resistivity of the films were measured by the Van der Pauw method, as described in chapter 2. Figure 5.8 depicts the temperature dependent electrical resistivity (ϱ) of the selected samples. As shown, resistivity, ϱ, increases exponentially with decreasing temperature from 300 to 80 K. The temperature dependent resistivity is very similar for all the films on the three different substrates.

An analysis of the low temperature behaviour of resistivity might provide some insights into the transport mechanism ongoing in the GBCO films. In order to check whether the temperature dependent electrical resistivity followed a thermal activation, the logarithm of resistivity was plotted against the reciprocal of temperature as depicted in Figure 5.8b. Apparently, it does not follow a simple thermal activation behaviour and is more likely that more than one conduction mechanisms are involved depending on the temperature range. Data fitting in Figure 5.8c shows that the low temperature resistivity of GBCO film fits well with the variable hopping (VRH) model showing a characteristics temperature dependent resistivity according to equation 5.2[8] where, ρ is resistivity, ρ_0 is the preexponential factor, T is absolute temperature and, T_0 is Mott temperature (related to disorder).

$$\rho = \rho_0 \exp\left(\frac{T_0}{T}\right)^{\frac{1}{d}} \qquad (5.2)$$

This type of conduction is typically exhibited by disordered systems where charge carriers move by hopping between localized electronic states (phonon assisted hopping). The disorder in the GBCO system might generate either from the deviation of oxygen stoichiometry or from cation disorder (and/or cation vacancies).

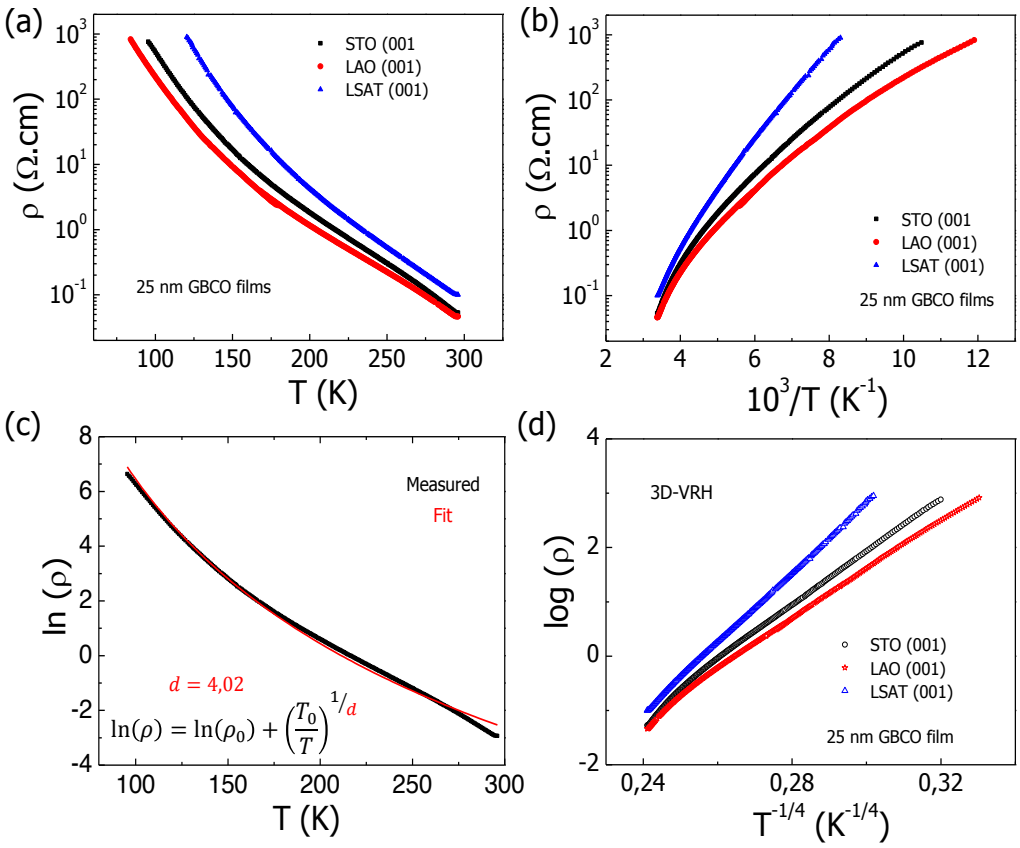

Figure 5.8 Electronic transport properties. (a)Temperature dependent electrical resistivity of 25 nm GBCO films grown on STO (001), LAO (001) and LSAT (001) substrates, (b) Resistivity fitting in a simple thermal activation model, (c) Fitting the temperature dependent resistivity of GBCO/STO film in a variable range hopping model, keeping dimension (d) as a free parameter and, (d) Plot of the temperature dependent resistivity of all the GBCO films in a 3D-VRH model.

Despite of the different cell parameters and domain orientations of the GBCO films on different substrates, temperature dependent resistivity does not show any significant difference. This indicates that transport anisotropy is not very important and grain boundaries do not introduce substantial barriers to electronic transport.

5.5 Thermoelectric transport properties

Pt metal electrodes were deposited via optical lithography for Seebeck effect measurements as described previously. Figure 5.9 depicts the real time thermoelectric response of GBCO/LSAT film at two different base temperatures. $V_{Seebeck}$ represents the voltage difference $(-\Delta V)$ when a certain temperature gradients were maintained. A series of temperature gradients were created by applying variable current on the heater as depicted in Figure 5.9 at a fixed base temperature (often called slope method) of 280 and 220 K, respectively. At the same time, $V_{Seebeck}$ were collected (blue data points).

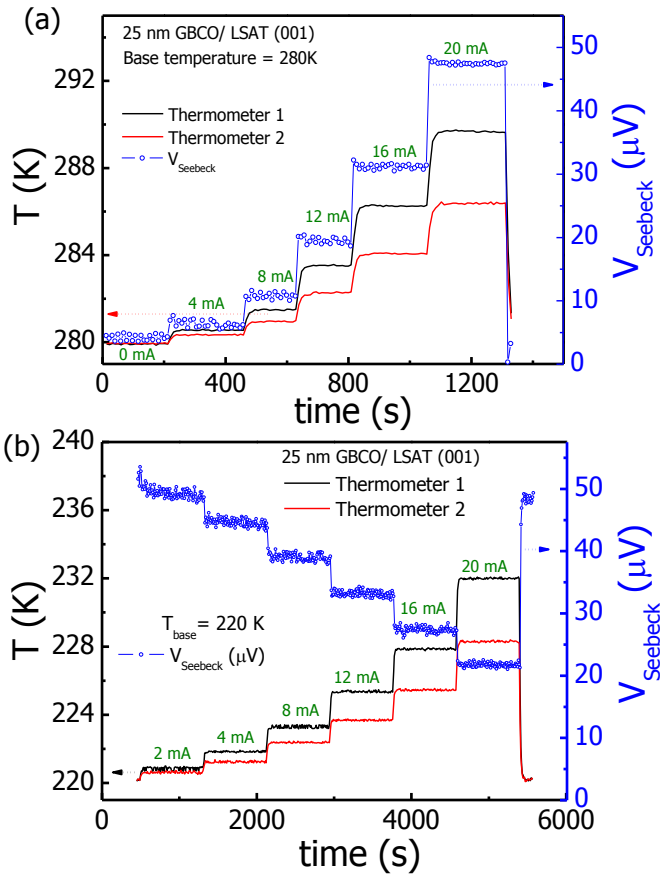

Figure 5.9 Real time Seebeck effect measurement of GBCO/LSAT (001) film: (a) real time temperature gradients and Seebeck voltage at (a) 280 K and, (b) 220 K respectively.

$V_{Seebeck}$ increases with increasing temperature gradient at 280 K base temperature while, $V_{Seebeck}$ decreases with increasing temperature difference at base temperature 220 K. This essentially indicates that $V_{Seebeck}$ changes its sign at 220 K relative to $V_{Seebeck}$ at 280 K.

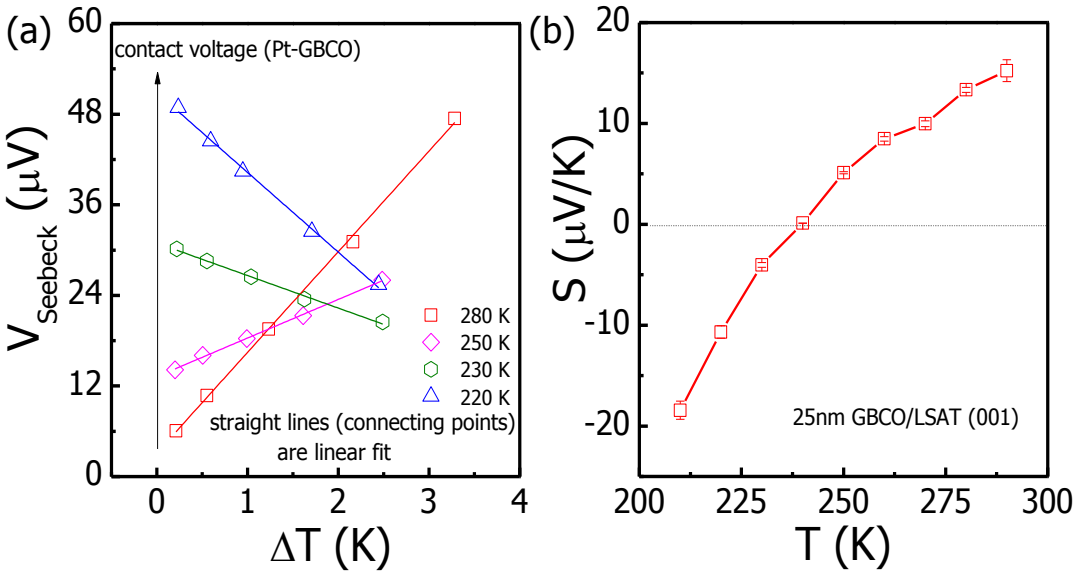

Figure 5.10 Estimation of Seebeck coefficient from slope method. (a) $V_{Seebeck}$ vs ΔT curve at different base temperature and, (b) Seebeck coefficient of GBCO/LSAT (001) as a function of temperature.

The measured Seebeck voltage was plotted against the temperature difference (ΔT) at several base temperatures as depicted in Figure 5.10a. Figure 5.10 shows the advantages of the slope method for measuring Seebeck coefficient. First, it can be seen that the slopes turns from positive to negative as temperature decreases from 280 to 220 K for the GBCO/LSAT (001) film. This means that the Seebeck coefficient i.e., the individual slopes, changed their sign from positive to negative. Since, $\Delta T = 0$, then $V_{Seebeck}$ should be zero for the intrinsic thermoelectric contribution of GBCO. The observed voltage differences at $\Delta T = 0$ were attributed to the barrier potential between the metal contact (Pt) with the GBCO film surface. It increases with decreasing temperature, as shown by the arrow in Figure 6.10a. This is likely due to large difference in charge carrier density between Pt and the GBCO surface at low temperatures. However, this method allows for separation of such contribution and it does not affect the measurement of the intrinsic Seebeck coefficient (S) of GBCO, as S depends only on the slopes of $V_{Seebeck}$ vs ΔT curve but not on the intercepts.

Thermopower of the thin films and oxygen stoichiometry

Temperature dependent S measured for GBCO/STO (001), GBCO/LSAT (001) and, GBCO/LAO (001) films are summarized in Figure 5.11a. For 25 nm thick GBCO/STO film, S is positive and acquires a value ~46 μV/K at 296 K. S increases almost linearly with further decreasing temperature from 300 to 230K and acquires a value of ~142 μV/K at 230 K. Below 230 K, the measured Seebeck voltage was noisy. S (T) of 25 nm GBCO/STO (001) film is very similar to that of GBCO single crystals of composition $GdBaCo_2O_{5.5+\delta}$ ($\delta > 0$) i. e. of Co^{+4}/Co^{+3} mixed valence, which is considered as hole doped as also evident from the positive sign of S (Ref 9 and 10).

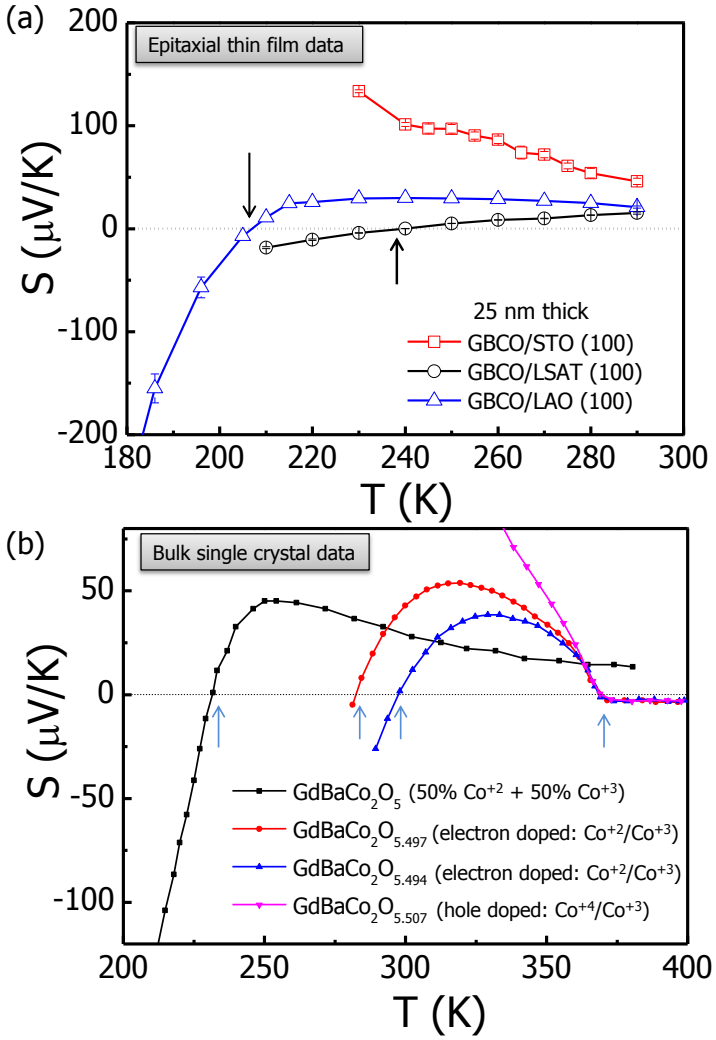

Figure 5.11 Thermoelectric Seebeck effect. (a) Temperature dependent Seebeck coefficient of the 25 nm GBCO films grown on STO (001), LAO (001) and LSAT (001) substrates. (b) Temperature dependent Seebeck coefficient of $GdBaCo_2O_{5.5+\delta}$ single crystals of variable oxygen stoichiometry. All data points of single crystals were digitized from the literature.[9], [10]

As can be seen in Figure 5.11a, the measured S of 25 nm thick GBCO/LSAT is +14 μV/K at 285 K. S decreases with decreasing temperature from 285 to 240 K showing a weak temperature dependence. It acquires a value of S close to zero at 240 K and then shows a crossover from positive to negative values. S decreases with further decreasing temperature from 240 to 210 K and acquires a value of -18 V/K at 210 K. In contrast, the measured S of 25 nm GBCO/LAO(001) is +21 μV/K at 296 K. S is almost temperature independent from 296 K to 215 K. This is an indication that the S reached it high temperature limit, which is discussed later. At T~210 K, S shows a crossover in sign from a positive value to a negative one and it decreases steeply with further decreasing temperature and acquires a value of -150 μV/K at 175 K. This temperature dependence of S is very similar to that of $GdBaCo_2O_5$ where the ratio of Co^{+2}/Co^{+3} is 1.

A qualitative comparison of the S (T) of the films and single crystals is presented in Table 5.3. Figure 5.11b represents the bulk single crystal data of variable oxygen stoichiometry (taken from the literature). Although, the films have different crystallographic orientations (pure or mixed), it is likely that the films hold different amounts of oxygen stoichiometry in order to accommodate the epitaxial strain induced by the single crystal perovskite substrates. The larger the compressive mismatch, the lower the apparent oxygen stoichiometry of the as deposited films.

Table 5.3 Comparison of the temperature dependent thermopower data of epitaxial GBCO films and bulk crystals.

Epitaxial films	Single crystals	Similarities
GBCO/STO (001) c-axis oriented	$GdBaCo_2O_{5.5+\delta}$ $0 < \delta < 0.2$	• $S > 0$ between 220 to 300 K • S increases with decreasing temperature
GBCO/LSAT (001) Mixed c-/a-axis oriented	$GdBaCo_2O_{5.5-\delta}$ $0.5 < \delta \leq 0$	• S shows crossover in sign between 240 to 300 K • S decreases steeply with decreases temperature below the crossover
GBCO/LAO (001) b-axis (and small vol. c-axis) oriented	$GdBaCo_2O_{5.5-\delta}$ $\delta = 0.5$	• S is T-independent from 250 to 300 K • S shows crossover in sign around 215 to 235 K

Crossover in sign of the thermopower: Bulk crystals vs thin films

From the measured S (T) of the epitaxial GBCO films and the reported S (T) of GBCO bulk single crystals of variable oxygen stoichiometries, it is clear that S shows non-monotonic change in the sign of S between 200 to 300 K, even though a single type of major charge carriers (either Co^{+2} or Co^{+4}) are present in the systems. For example, all hole doped $GdBaCo_2O_{5.5+\delta}$ (for $\delta > 0$) crystals and GBCO/STO films show positive S at 300 K and they show no crossover from 200 to 300 K. On the other hand, all electron doped $GdBaCo_2O_{5.5-\delta}$ (for $0 < \delta < 0.5$) crystals and GBCO/LSAT film show positive S at 300 K crossovers between 250 to 300 K from negative to positive (See Figure 5.11b for bulk and thin films). Therefore, even though GBCO/LSAT is an electron doped film, still it shows positive S at 300 K. $GdBaCo_2O_5$ crystal and GBCO/LAO film show a crossover from negative to positive with increasing temperature from 215 to 235 K. Therefore, even though the ratio of Co^{+2}/Co^{+3} ions is 50% : 50%, they show positive S at 300 K. Hence, in general, it can be said that all electron doped and hole doped GBCO films shows positive thermopower at 300 K. Therefore, the two important questions are the following;

i) Why do electron doped GBCO films show positive S at 300 K?; and;,

ii) Does the crossover in the sign of S as a function of temperature correspond to a *p*- to *n*-type transition?

The following paragraphs describe the possible reasons for the positive S of electron doped films.

Statistical distribution of charge carriers over available sites ?

It is important to recall the high temperature limit of thermopower which turns into a temperature independent solution as discussed in detail in chapter 1. In this case, S is governed by the statistical distribution of charge carriers (x) over available sites ($1-x$), generally expressed by Heike's formula as follows,[11]

$$S_{T\to\infty} = -\frac{\kappa_B}{e}\ln\left(\frac{1-x}{x}\right) \qquad (1.17)$$

Equation 1.17 is applicable for electron doped systems near correlated hopping regime. It turns out that at high temperature limit, enhancement (or optimization) of S is independent of electronic band structure.

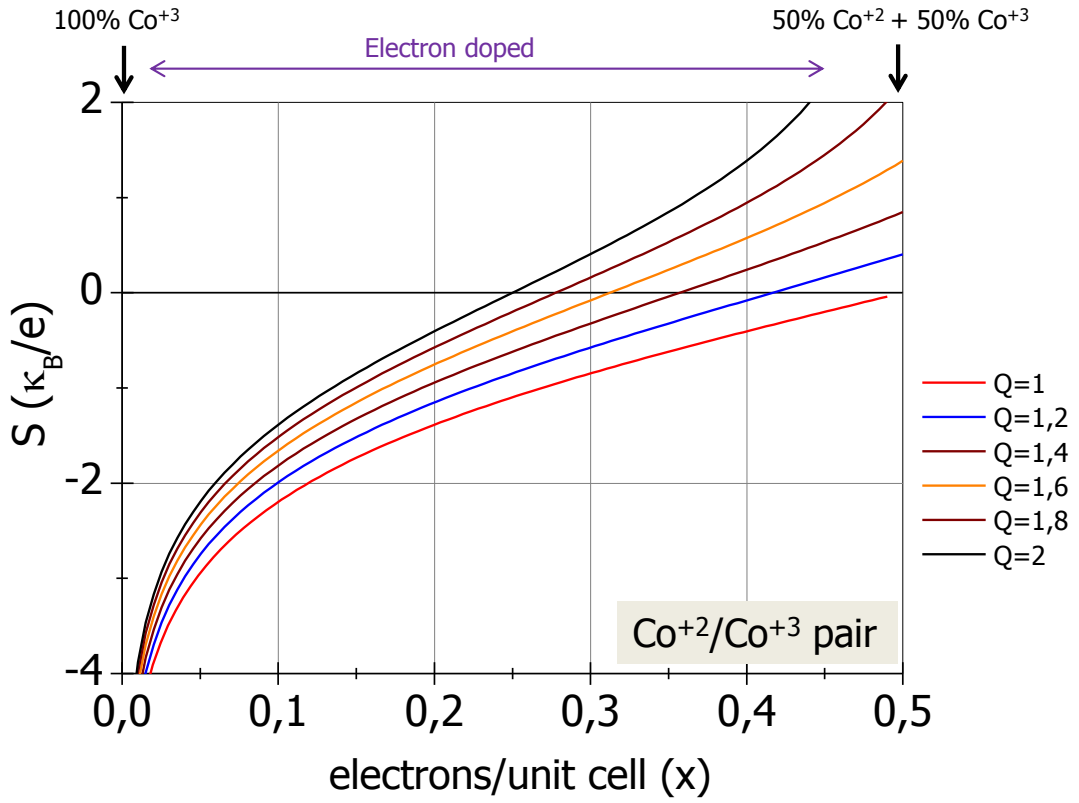

Figure 5.12 Distribution of the Seebeck coefficient according to the Heike's formula in the electron doped regime with variable size of polarons. Unit of *S* is represented in (κ_B/e) unit which is approximately ~86.14 μV/K.

Modification of Heike's formula provides information about polaron size (Q)[12] if it is derived as follows:

$$S_{T\to\infty} = -\frac{\kappa_B}{e}\ln\left(\frac{1-Q.x}{Q.x}\right) \qquad (5.4)$$

$Q = 1$ represents formation of small polarons which renders the classical Heike's formula. It is clear from the above equation that the sign of *S* at the high temperature limit is determined by the ratio of filled to vacant sites (for example, the ratio is always less than zero for a positive Seebeck coefficient, observed for misfit cobaltates at 300 K)[13]. Classical Heike's formula is based on the assumption that two charge particles can not occupy the same available sites.[11] Here, Q plays an important role. It actually represents the number of available sites shared by a single charged particle. Interestingly, if Q acquires such a value (for example, the formation of large polarons, $Q > 1$) which turns the filled to vacant ratio more than unity, it will

result in a negative S even if the same type of charged carriers are present in the system. This effect is illustrated in Figure 5.12 where the distribution of S according to Heike's formula in an electron doped regime is shown with variable polaron size (Q). S is represented in a standard unit, κ_B/e, which is ~86.14 μV/K. Interestingly, electron doped samples might show positive thermopower in the high temperature limit if the polaron size is large (Q>1).

From the experimental results presented in chapter 4, the existence of large polarons ($Q = 1.07 \rightarrow 1.5$) is realized from the thermopower data analysis in the vicinity of the metallic phase of GBCO films grown on STO (001) substrates. It was concluded therefore, that the thermopwer of GBCO films is governed by the incoherent transport near the metallic phase. S of GBCO films grown on different substrates presented in this chapter also show typical behavior of polarons, displaying temperature independent S from 220 to 296 K particularly evident in the case of GBCO/LAO (001). Therefore, we assign the formation of large polarons in order to explain the positive S of electron doped films.

Theoretical calculation of doping dependent thermopower near Mott transition, using dynamic mean field theory (DMFT) by Pálsson and Kotliar,[14], shows a crossover in the sign of S as a function of doping concentration. An experimental study in $La_{1-x}Sr_xVO_3$ by Uchida *et. al.*[15] reveals similar characteristics of the crossover of sign of S near Mott transition. Therefore, sign of S might be governed by the statistical distribution of the charge carriers over vacant sites.

Here we conclude that both the temperature independent S and crossover in the sign of the S at 300 K of GBCO/LSAT and GBCO/LAO films are the signature of the presence of incoherent charge carriers.

The following paragraphs describe the possible reasons for the temperature dependent crossover of the sign of S of the GBCO/LSAT and GBCO/LAO films.

Shift of Fermi energy and DOS ?

In conventional metal or semiconductors, the sign of S changes with the sign of charge carriers. For example, many authors have reported a *p*-type to *n*-type (or reverse in order) switching, which are associated with structural phase transitions.[16], [17], [18] As the magnitude of the Seebeck coefficient is determined by average energy transported in the Fermi window (first derivative of the Fermi function with respect to energy) where conduction takes place and the sign of S is determined by the position of Fermi energy with respect to the average transported

energy. Such a kind of structural phase transition brings changes in the electronic band structure and thus the position of the Fermi energy which eventually determines the sign of the charge carriers and the Seebeck coefficient. This phenomena is well understood for the for metals and semiconductors where diffusive transport of chage carriers dominates the conduction.

In GBCO bulk crystals and epitaxial thin films, there is only one type of major charge carrier (either holes or electrons) is present as described before. GBCO bulk crystals show structural phase transition from rhombohedral to orthorhombic and again to rhombohedral depending on the concentration of oxygen vacancies they hold except at 300 K (shown in Figure 6.1 in chapter 6).[10] Interestingly, a second order structural phase transition has been observed for $GdBaCo_2O_{5.5}$ due to charge ordering from disordered to ordered Co^{+2}/Co^{+3} (1:1) mixed valence.[19] To the best of our knowledge, there is no report yet which describes the variation of density of states (DOS) near Fermi energy due to charge ordering. From the resistivity data fitting, we saw the resistivity below 250 K follow Mott's VRH mechanism. The fundamental assumption of the Mott's variable range hopping mechanism is that the density of states (DOS) near the Fermi energy is constant (Ref: Book, N. F. Mott, Electrons in disordered structures, page 49-144, https://doi.org/10.1080/00018736700101265). It is also evident from the spectroscopy data that $RBaCo_2O_{5.5\pm\delta}$ (R= Nd, Gd etc) compounds are narrow band gap insulators.[20], [21], [22] The DOS near E_F does not vary much with decreasing temperature. Therefore, we assume the charge ordering will affect the scattering time dominantly.

Strongly energy dependent scattering time?

One possibility for the sign change of *S*, even though the Hall resistance does not change sign, might be due to the sharp change of mobility with temperature as recently pointed out in a heavy Fermion system in the Kondo scattering regime.[23], [24] In this case, scattering time is strongly energy dependent. As a consequence, the Seebeck coefficient is largely influenced by the Nernst coefficient. This was observed for the metallic systems (where Mott's equation is valid) and at low temperature (below 20 K) where resistance increases exponentially due to scattering in presence of magnetic impurities. GBCO films shows hopping character of the charge carriers below 250 K where Mott's formula cannot be applied to estimate thermopower. However, in order to verify this possibility in case of GBCO films, accurate Hall effect measurement as well as simultaneous Seebeck effect and Nernst effect measurements are necessary to perform, which is beyond the scope of this thesis.

Spin-blockade effect ?

A different and unusual reasoning, called spin-blockade phenomena, was used to explain the temperature dependent thermopower of a similar compund $HoBaCo_2O_{5.5}$ (HBCO),[25] which is associated with the spin-state transition of Co^{+3} ions (discussed in chapter 1, Figure 1.17). Spin-blockade means that the Co^{+2} (HS) ions are restricted to hop in the back ground of Co^{+3} (LS) ions due to unfavourable spin states. Therefore, Co^{+4} ions (holes) conduct but, not the Co^{+3} ions and, as a consequence, it shows positive S. Above MIT, Co^{+3} ions acuire HS state (after LS to HS state transition of Co^{+3} ions in octahedral coordination) and thus Co^{+2} (HS) are allowed to hop. As a result, HBCO shows negative S above the MIT. In general, the spin-blockade phenomena describes a completition between Co^{+2} and Co^{+4} ions in HBCO due to spin-state transition. Therefore, due to the spin-state transition, Co^{+2} (HS) ions should dominate the conduction mechanism over Co^{+4} ions in the Co^{+3} (LS to HS transition) background. This effect will be reflected in the temperature dependent S i.e. in magnitude and sign of S accordingly.

Interestingly, a similar spin-blockade phenomena is used to explain the asymmetry in resistivity of electron doped GBCO crystals at 100 K.[9] Therefore, a similar hopping conduction of cobalt ions is expected in electron doped GBCO crystals. But, the electron doped GBCO crystals show negative to positive thermopower with increasing temperature from 200 to 300 K. Therefore, this crossover in S cannot be explained by the spin-blocked effect.

Spin-state transition ?

The spin-state transition associated with metal to insulator transition in GBCO crystals might influence temperature dependent S behaviour and also the crossover in the sign of S of bulk crystals and for the films (although no experiment has been performed yet to check the spin states of cobalt ions of GBCO films). In the spin-state transition of Co^{+3} ion from LS to HS in a closely related compound, $LaCoO_3$ does not exhibit a first order transition (i.e., 100% LS to 100 % HS conversion) rather, it shows ≈ 50% LS + ≈ 50% HS mixed states. At any definite temperature, the spin state of Co^{+3} ion in $LaCoO_3$ was described as a mixed LS and HS states.[26] Given that S is determined by statistical distribution of the charge carriers over available sites, temperature dependent (more accurately, spin-state transition dependent) S in GBCO crystals and films might follow a mechanism which controls the parameter Q (and thus ratio of filled to vacant sites), and therefore the sign of S. This mechanism might be reflected in the S (T) behaviour with multiple crossovers in the sign of S near the metallic phase.

A first principle study in $GdBaCo_2O_{5.5}$ by Pardo et al[27] shows that the electronic structure changes due to the spin state transition of Co^{+3} in the octahedral coordination. In this regard, it is important to notice that the metallic phase of GBCO crystals (GBCO films were not measured above 300 K) is found ~360 K, where *S* changes its sign from positive to negative. Thereofre, crossover of the sign of *S* at 360 K can be explained by the change of electronic structure but, the crossover observed between 200 to 300 K of the GBCO films can not be explained in this way.

Therefore, the sign change of the *S* in the GBCO films as a function temperature can not be assigned to a *p*- to *n*-type transition.

- Cation vacancies in GBCO/LSAT film?

From the above description, we assign the formation of large polarons in order to explain the positive *S* in an electron doped sample as in the GBCO/LSAT film. Any further electron doping in GBCO/LSAT film should cause an enhancement of the magnitude of positive S near 296 K as shown in Figure 5.12 for a particular Q>1.

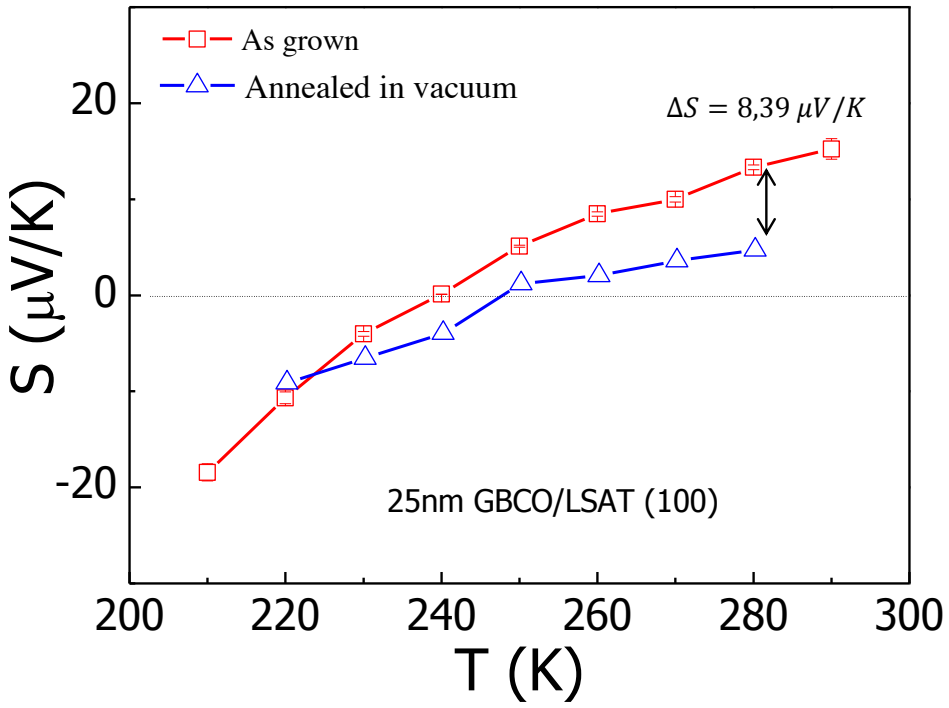

Figure 5.13 Annealing effect on the thermopower of 25 nm GBCO/LSAT (001) film. Crossover temperature (~242 K) in the sign of thermopower shifts at relatively higher temperature (~250K) after annealing in vacuum.

In order to investigate further the role of electron doping via the creation of oxygen vacancies in the thin film, GBCO/LSAT was annealed (same sample, without removing the electrical contacts) at 400°C for 2 hours in vacuum (10^{-3} mTorr) followed by a fast cooling. The Seebeck effect was measured for the cooled film. The measured S and its temperature dependence of the as grown GBCO/LSAT (001) and after annealing in a vacuum are depicted in Figure 5.13. Some significant changes in S (T) behaviour are observed after annealing. Although the temperature dependence of S remains very similar before and after annealing, the magnitude of S at 285 K is decreased after annealing ($\Delta S = -8.3$ μV/K). Extra electrons are expected to be introduced in the film due to the creation of oxygen vacancies after annealing in vacuum, and hence the magnitude of S should increase. The decrease of S at 280 K, points towards the presence of some electron acceptors such as the presence of cation vacancies (Gd^{+3}/Ba^{+2}) in the GBCO film. An alternative explanation of the decrease of S could be related to the change in the polarons size after annealing. However, a further study is needed to understand the defect chemistry.

5.5 Summary

In this chapter, we have studied the effect of epitaxial strain on the thin film orientation, microstructure and the thermoelectric properties of GBCO films. The GBCO film is highly c-axis oriented under tensile strain on STO (001) substrate while mixed c-/a-axis oriented domains were observed under slight compressive strain on LSAT (001) and a b-axis domain (90 rotated in-plane c-axis) was obtained on a large compressive mismatch on LAO. Thermopower around room temperature was dominated by the incoherent motion of charge carriers. Comparison of the temperature dependent thermopower of bulk single crystals and epitaxial thin films indicates that the thin films accomodate oxygen vacancies in order to sustain the tensile or compressive strain. The non-monotonic sign change of Seebeck coefficient of GBCO/LSAT and GBCO/LAO below 296 K is attributed to the change in the statistical distribution of charge carriers over available sites rather than to a shift of Fermi energy in the electronic band structure.

Bibliography

[1] J. H. Lee, L. Fang, E. Vlahos, X. Ke, Y. W. Jung, L. F. Kourkoutis, J. W. Kim, P. J. Ryan, T. Heeg, M. Roeckerath, et al., *Nature* **2010**, *466*, 954–958.

[2] X. Z. Lu, J. M. Rondinelli, *Nat. Mater.* **2016**, *15*, 951–955.

[3] I. Bozovic, G. Logvenov, I. Belca, B. Narimbetov, I. Sveklo, *Phys. Rev. Lett.* **2002**, *89*, 107001.

[4] E. Rauwel-Buzin, W. Prellier, C. Simon, S. Mercone, B. Mercey, B. Raveau, J. Sebek, J. Hejtmanek, *Appl. Phys. Lett.* **2001**, *79*, 647.

[5] F. Tsui, M. C. Smoak, T. K. Nath, C. B. Eom, *Appl. Phys. Lett.* **2000**, *76*, 2421–2423.

[6] B. Rivas-Murias, I. Lucas, P. Jiménez-Cavero, C. Magén, L. Morellón, F. Rivadulla, *Nano Lett.* **2016**, *16*, 1736–1740.

[7] H. Beyer, J. Nurnus, H. B. Ottner, A. Lambrecht, E. Wagner, G. Bauer, *Phys. E* **2002**, *13*, 965–968.

[8] Y. Machida, X. Lin, W. Kang, K. Izawa, K. Behnia, *Phys. Rev. Lett.* **2016**, *116*, 87003.

[9] A. A. Taskin, Y. Ando, *Phys. Rev. Lett.* **2005**, *95*, 176603.

[10] A. A. Taskin, A. N. Lavrov, Y. Ando, *Phys. Rev. B - Condens. Matter Mater. Phys.* **2005**, *71*, 134414.

[11] P. M. Chaikin and G.Beni, *Phys. Rev. B* **1976**, *13*, 647.

[12] E. Winkler, F. Rivadulla, J. S. Zhou, J. B. Goodenough, *Phys. Rev. B - Condens. Matter Mater. Phys.* **2002**, *66*, 944181–944184.

[13] T. Yamamoto, I. T. Uchinokura, K, *Phys. Rev. B* **2002**, *65*, 184434.

[14] G. Palsson, G. Kotliar, *Phys. Rev. Lett.* **1999**, *80*, 4775.

[15] M. Uchida, K. Oishi, M. Matsuo, W. Koshibae, Y. Onose, M. Mori, J. Fujioka, S. Miyasaka, S. Maekawa, Y. Tokura, *Phys. Rev. B - Condens. Matter Mater. Phys.* **2011**, *83*, 165127.

[16] S. N. Guin, K. Biswas, *Phys. Chem. Chem. Phys.* **2015**, *17*, 10316–10325.

[17] S. N. Guin, J. Pan, A. Bhowmik, D. Sanyal, U. V. Waghmare, K. Biswas, *J. Am. Chem. Soc.* **2014**, *136*, 12712–12720.

[18] C. Han, Q. Sun, Z. X. Cheng, J. L. Wang, Z. Li, G. Q. Lu, S. X. Dou, *J. Am. Chem. Soc.* **2014**, *136*, 17626–17633.

[19] M. Allieta, M. Scavini, L. Lo Presti, M. Coduri, L. Loconte, S. Cappelli, C. Oliva, P. Ghigna, P. Pattison, V. Scagnoli, *Phys. Rev. B - Condens. Matter Mater. Phys.* **2013**, *88*, 1–10.

[20] T. C. Koethe, *PhD ThesisUniversitat zu Koln* **2007**, 1–97.

[21] W. R. Flavell, A. G. Thomas, D. Tsoutsou, A. K. Mallick, M. North, E. A. Seddon, C. Cacho, A. E. R. Malins, S. Patel, R. L. Stockbauer, et al., *Phys. Rev. B - Condens. Matter Mater. Phys.* **2004**, *70*, 224427.

[22] K. Takubo, J.-Y. Son, T. Mizokawa, M. Soda, M. Sato, *Phys. Rev. B* **2006**, *73*, 75102.

[23] P. Sun, B. Wei, J. Zhang, J. M. Tomczak, A. M. Strydom, M. Søndergaard, B. B. Iversen, F. Steglich, *Nat. Commun.* **2015**, *6*, 1–5 (DOI: 10.1038/ncomms8475).

[24] P. Sun, F. Steglich, *Phys. Rev. Lett.* **2013**, *110*, 216408.

[25] A. Maignan, V. Caignaert, B. Raveau, D. Khomskii, G. Sawatzky, *Phys. Rev. Lett.* **2004**, *93*, 26401–1.

[26] M. W. Haverkort, Z. Hu, J. C. Cezar, T. Burnus, H. Hartmann, M. Reuther, C. Zobel, T. Lorenz, A. Tanaka, N. B. Brookes, et al., *Phys. Rev. Lett.* **2006**, *97*, 176405.

[27] V. Pardo, D. Baldomir, *Phys. Rev. B* **2006**, *73*, 165117.

Chapter 6: Control of oxygen stoichiometry in $GdBaCo_2O_{5.5\pm\delta}$ thin film by electrochemical potential

In previous chapters, it was shown that the oxygen stoichiometry of the thin films can be stabilized either by chemical stimulus (by changing pO_2) or by manipulating epitaxial strain. However, the oxygen stoichiometry cannot be accurately controlled by these processes.

This chapter shows the control of oxygen stoichiometry in $GdBaCo_2O_{5.5+\delta}$ thin film by applying electrochemical bias voltage across the GBCO/YSZ heterostructure.

6.1 Introduction

Perovskite compounds of transition metal oxides are an attractive class of compounds because of their tunable mixed electronic and ionic transport properties.[1] These compounds are useful in energy storage and conversion devices, such as solid oxide fuel cells,[2] information storage and, processing applications.[3] Generally, oxygen non-stoichiometry is associated with these types of compounds,[4] which has a strong influence on their chemical (e.g., catalytic), structural (e.g., structural phase transition) and electronic transport properties. Therefore, it is desirable to precisely control the oxygen vacancies (or stoichiometry) in order to tune the chemical and physical properties reversibly. It has been reported that a large oxygen non-stoichiometry can be accommodated in perovskite related oxides by forming ordered oxygen vacancy channels in $ABO_x (x = 2.5)$ compounds such as $CaFeO_{2.5}$,[5] $SrFeO_{2.5}$ [6] and $ScCoO_{2.5}$.[7]

A-site double perovskites such as the $LnBaCo_2O_{5.5\pm\delta}$ $(Ln = Pr, Gd, Tb, Ho, Eu, Nd, Sm)$ family of compounds, exhibit ordered oxygen vacancy channels along the crystallographic a-axis within a certain oxygen nonstoichiometry that enhances oxygen transport.[8], [9] Therefore, these compounds are mixed electronic and ionic conductors. A structural phase transition is also associated with the δ content in $GdBaCo_2O_{5.5\pm\delta}$ (GBCO) at room temperature in bulk crystals,[10] as depicted in Figure 6.1a.

Stoichiometric GBCO crystal $(\delta = 0)$ is an *n*-type conductor. Although the average oxidation state of Co at $\delta = 0$ is +3, a competition between Co^{+2} (electrons) and Co^{+4} (holes) ions was observed near room temperature both in bulk crystals and thin films (see the discussion in chapter 5). At low temperature, it is apparent that Seebeck coefficient is negative.[11] As mentioned previously, a slight deviation of the oxygen stoichiometry from δ=0, brings significant changes in the transport properties. For example, GBCO crystal becomes *p*−type conductor at $\delta > 0$ and *n*-type at $\delta \leq 0$, as depicted in Figure 6.1b. Therefore, *p*−type to *n*−type switching along with doping in the CoO_2 layer can be achieved in GBCO if oxygen nonstoichiometry is controlled precisely.

Recently, it has been shown by Jeen *et. al*. that a variable amount of nonstoichiometry can be stabilized in $SrCoO_x$ thin films (of distinct electronic and magnetic properties) either by epitaxial strain[12] or by chemical stimuli. For example, by controlling the oxygen partial pressure (p^{O_2})[13] and, it can also be reversibly oxidized and reduced. Moreover, the kinetics of the phase transformation was found to be fast due to extremely small diffusion length of oxygen incorporated in the thin film. Just recently, Lu et al[14] have shown that the phase transition in

$SrCoO_x$ thin film can also be triggered by applying an electrochemical stimulus and thus overcoming the difficulties in switching a p^{O_2} environment from high (5 atms) to low (10^{-6} atms) pressure.

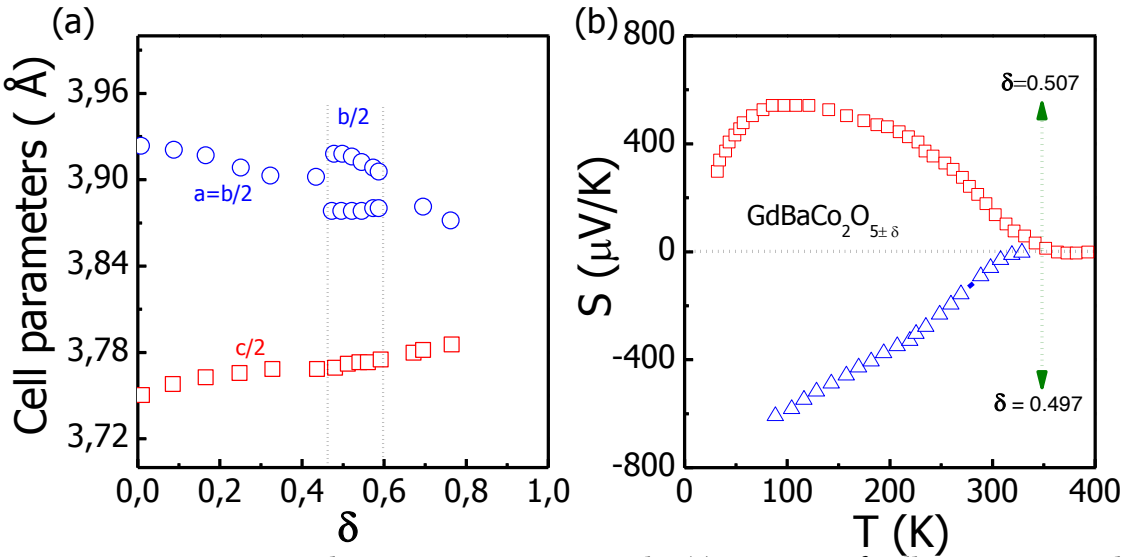

Figure 6.1 Oxygen non stoichiometry in GBCO crystals: (a) variation of cell parameters with oxygen nonstoichiometry and (b) temperature dependent Seebeck coefficient of electron and hole doped GBCO crystals by means of controlling oxygen nonstoichiometry. All the data in this figure were digitized from the literature.[15]

In a solid state electrochemical cell, the oxidation state of the electrode can be changed by chemical stimuli (change in p^{O_2}) or by varying the electrochemical potential. By applying an electrochemical potential (φ) between the electrodes, the flow of ionic charge establishes the equilibrium at an effective pO_2, according to Nernst equation;[14]

$$\varphi = -\frac{RT}{nF} ln\left(\frac{p^{O_2}}{p^{O_2^{eff}}}\right) \qquad (6.1)$$

where φ, R, n, F, T, p^{O_2} and, $p^{O_2^{eff}}$ represent the effective applied electrochemical potential, ideal gas constant, number of electrons involved in the electrochemical redox reaction, Faraday constant, oxygen partial pressure and effective oxygen partial pressure respectively. If one of the electrodes is an oxide with variable oxygen nonstoichiometry, the effective oxygen partial pressure induces the oxidation or reduction of the electrode material, without changing the pO^2 of the gas atmosphere. Many experiments have been recently performed to control oxygen nonstoichiometry by electrical (and/or ionic) gating[16], [17] and thus, to control electronic

properties. For example, suppression of metal-insulator transition in VO_2 thin film was achieved via ionic gating using ionic liquid at room temperature,[18] whereas the use of oxide ionic electrolyte needs sufficient temperature (T> 300°C) for an effective oxygen diffusion. Kawada et al[19] and Chen et al[20] validated this approach by controlling oxygen non stoichiometry in $(La, Sr)CoO_{3-\delta}$ and $(Pr, Ce)O_{2-\delta}$ thin films, respectively.

In this chapter, the control over oxygen stoichiometry in GBCO film by applying electrochemical potential is presented. A solid state electrochemical cell (more precisely a half-cell) with YSZ electrolyte was considered as a means to control the oxygen stoichiometry in the oxide electrode without varying the atmospheric pressure. The aim of this chapter is to verify the concept of the Nernst principle for an electrochemical cell in a GBCO film/YSZ heterostructure. The effect of oxidation and reduction of the GBCO film is reflected in its cell parameter (or in cell volume) change. The change in oxygen stoichiometry produces not only the variation of oxygen site occupancy but also in the transition metal cations oxidation state, to compensate the charge and remain neutral. The changes in oxygen concentration along with the change in the effective cation radius produce a change in the unit cell volume, the so-called chemical strain. Thus, voltage controlled chemical strain was monitored by in-situ X-ray diffraction throughout the experiment.

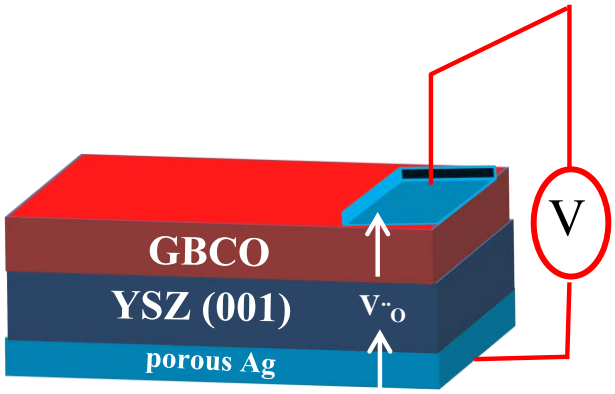

Figure 6.2 Schematic illustration of the electrochemical device. A 200 nm GBCO thin film is grown on a YSZ (001) substrate (5×5×0.5 mm). Porous Ag film at the bottom of YSZ substrate acts as a counter electrode. 50 nm thin Pt metal counter electrode was deposited on the top of GBCO film surface. When an electrochemical bias is applied, oxygen vacancies flow through the heterostructure, shown by the arrow. Pt electrode covers only one part of the surface and the other part of the GBCO film surface remains exposed to air atmosphere.

6.2 Sample preparation and characterization

In this experiment, a 200 nm thick GBCO film acts as the working electrode, Y_2O_3 substituted ZrO_2 (YSZ) acts as the electrolyte (pure ionic conductor, used as a substrate to grow the GBCO film) and a porous Ag film at the bottom of YSZ acts as the counter electrode. The GBCO thin film heterostructure and the structure of electrochemical device are depicted schematically in Figure 6.2.

GBCO film was grown on yittria-stabilized zirconia (YSZ-001) substrate by the pulsed laser deposition (PLD) technique at 850°C. The film was grown with a laser energy fluency of 1.5 J/cm^2 at 60 mTorr pO^2 at a repetition rate of 10 Hz, as described in previous chapters. In order to avoid any chemical reaction at the interface, a thin buffer layer of 20% at Gd doped Ceria (CGO) was grown between the GBCO film and YSZ substrate which will be discussed later. Consequently, the cell structure can be described as GBCO/CGO/YSZ.

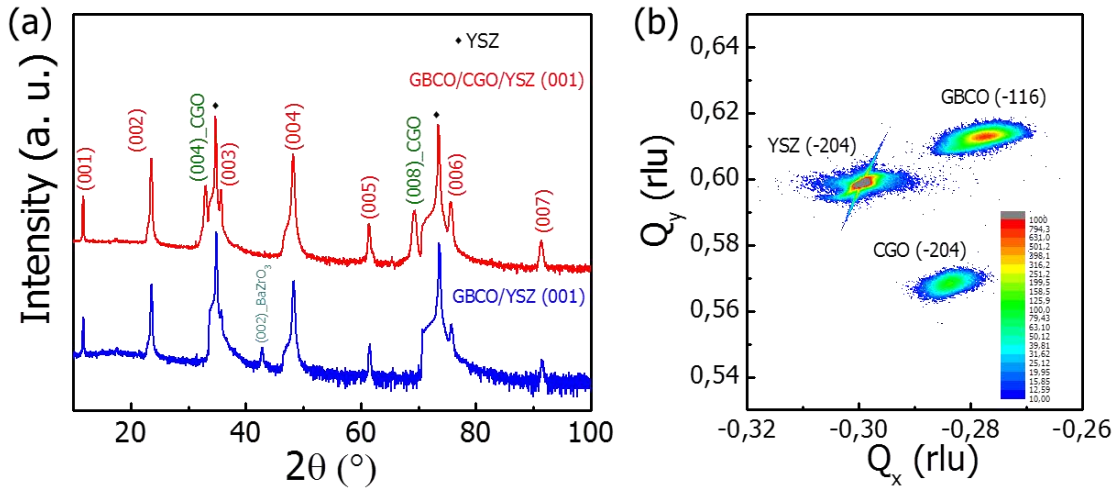

Figure 6.3 X-ray diffraction of GBCO/CGO/YSZ thin film hetero structure: (a) standard 2θ/ω pattern of GBCO/YSZ (blue pattern) and GBCO/CGO/YSZ (red pattern) and (b) RSM around (-204) of YSZ, (-116) around GBCO and (-204) around CGO layer.

Figure 6.3a depicts the standard 2θ-ω XRD pattern of GBCO film grown on the top of (001) YSZ (blue coloured pattern) and CGO/(001) YSZ (red coloured pattern). Highly c-axis oriented GBCO film with the appearance of both odd and even symmetric 00*l* reflections was grown indicating the double perovskite nature of the GBCO film with alternating BaO and GdO layers along the crystallographic c-axis. High temperature growth of GBCO on YSZ (001) results in a secondary phase of non-conducting $BaZrO_3$ layers between YSZ substrate and GBCO film interface due to the chemical reaction of BaO (from GBCO film) with ZrO_2 (from substrate YSZ)

which prevents oxygen transport at the interface. XRD pattern (blue) shows the appearance of (002) $BaZrO_3$ reflection. CeO_2 does react neither with GBCO nor with YSZ, therefore preventing the chemical reaction. Gd substituted CeO_2 (CGO) is also an ionic conductor. Therefore, use of CGO layer has the double purpose of preventing the reaction while maintaining sufficient oxide ion exchange at the GBCO/CGO interface. A thin (~15 nm) CGO buffer layer was deposited between YSZ and the GBCO film to prevent the chemical reaction. The XRD pattern (red colored pattern) of GBCO film grown on CGO/YSZ shows the absence of reflections from $BaZrO_3$. The pattern shows intense (00*l*) reflections from the CGO layer. We performed reciprocal space maps (RSMs) by XRD around the (-204) reflection of the YSZ substrate to investigate the in-plane orientation of the film, which covers the (-116) reflection of the GBCO film and the (-204) reflection of the CGO layer. The out-of-plane and the in-plane lattice parameters of GBCO calculated from RSM is ~3.773 Å and 3.928 Å , respectively.

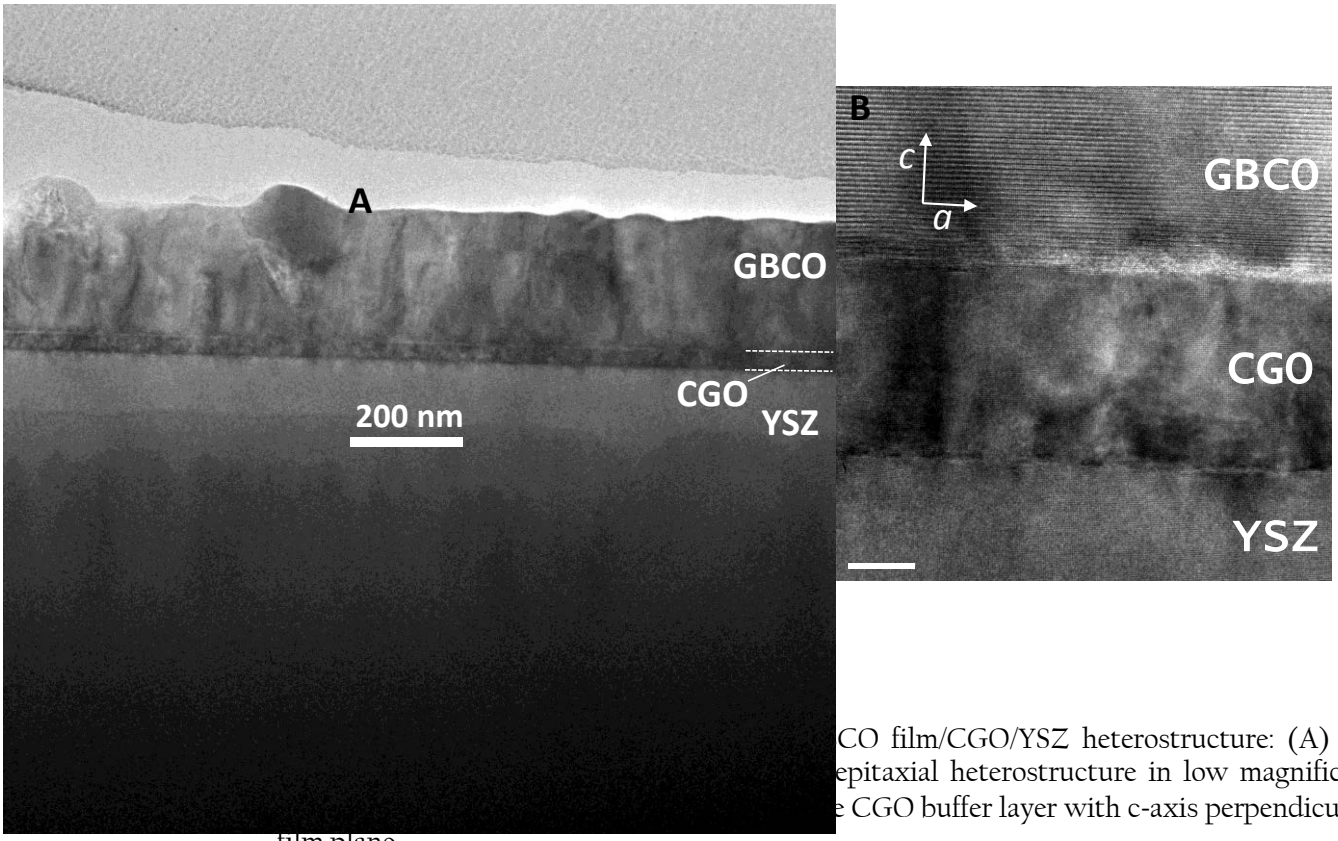

CO film/CGO/YSZ heterostructure: (A) cross epitaxial heterostructure in low magnification e CGO buffer layer with c-axis perpendicular to film plane.

Figure 6.4 depicts the cross section TEM image of GBCO/CGO/YSZ heterostructure. The presence of the CGO buffer layer on top of YSZ and the GBCO layer on top of CGO layer of definite thicknesses is apparent in Figure 6.4a. As can be observed, the interface between the CGO/GBCO and CGO/YSZ are very sharp, which is an indication of the absence of any chemical reaction and interdiffusion. In the higher magnification TEM image of the GBCO film, there is a clear contrast between the horizontal rows with high and low brightness dots forming a sequence every two perovskite blocks along the vertical direction as depicted in Figure 6.4B. This is an indication of perovskite doubling along the c-axis in the GBCO layer.

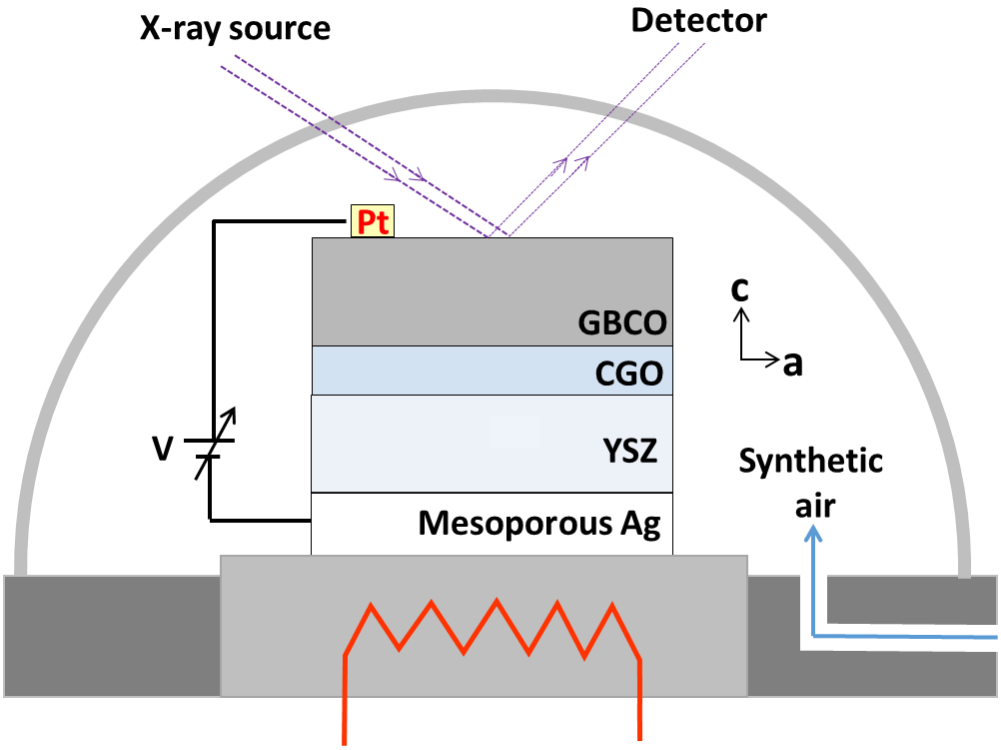

Figure 6.5 Experimental set up inside the X-ray diffractometer. The semicircle arc is a graphite dome which allows transmission of X-ray beam and at the same time it seals the chamber to achieve a stable oxygen partial pressure inside.

6.3 Experimental set up

A Pt electrode (top electrode) was deposited on the GBCO film surface over 0.4 mm×0.5 mm area by using the PLD technique, as depicted in Figure 6.5. Special care was taken to avoid deposition of Pt on the sides of the GBCO/CGO/YSZ cell in order to prevent current leakage during the electrical measurements. Ag paste was used to make contact with the Pt electrode and Ag wire. The bottom part of the YSZ substrate was coated with silver paste to make a

mesoporous silver layer and a spiral shaped Ag wire was connected with the silver paste. The complete experimental set up is depicted in Figure 6.5. An Anton Paar DHS 900 domed chamber from PANalytical was used to heat the sample at 350°C in the X-ray diffractometer. In order to have sufficient oxide ion conductivity in the YSZ electrolyte, high temperatures are needed. This also guaranties the achievement of sufficient oxygen exchange at the interface between the top GBCO and bottom Ag electrodes and the gas atmosphere, which is also necessary for the oxygen ion supply.

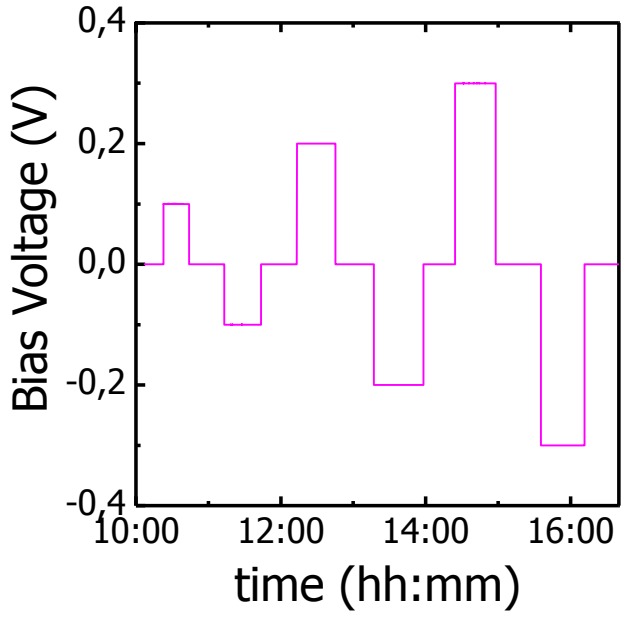

Figure 6.6 Plan of the experiment. Applied cathodic and anodic potential (bias voltage) throughout the experiment.

6.4 Plan of the experiment

The experiment was performed at 350°C. The plan of the experiment was to continuously collect the 2θ angular position by X-ray diffraction of a GBCO reflection at 10 second time intervals when a particular bias voltage was kept ON and OFF, respectively. (004) A continuous flow of synthetic air (a mixture of 21% oxygen and 79% nitrogen) was maintained throughout the experiment. The (004) symmetric reflection of GBCO film was chosen for this experiment. This is the highest intensity (00*l*) GBCO reflection and it is far from any YSZ reflection. The Out-of-plane cell parameters were extracted by fitting the (004) reflection to a single Gaussian curve using Matlab software. In the condition, this method allowed the

determination of c-parameters of GBCO film with an accuracy of 10^{-4}Å. Both positive and negative bias from 0 volt to ±0.1 V, ±0.2 V and ±0.3 V were applied as depicted in Figure 6.6. The bias voltage was kept ON (constant value) until the chemical expansion or contraction saturated and then the bias was switched OFF until it returned to the ground state. In this way, we were able to check the reversibility of the chemical processes involved. At the same time, in-situ cross plane current transients (I-t curves) were collected. Bias voltage was controlled via Lab Window software.

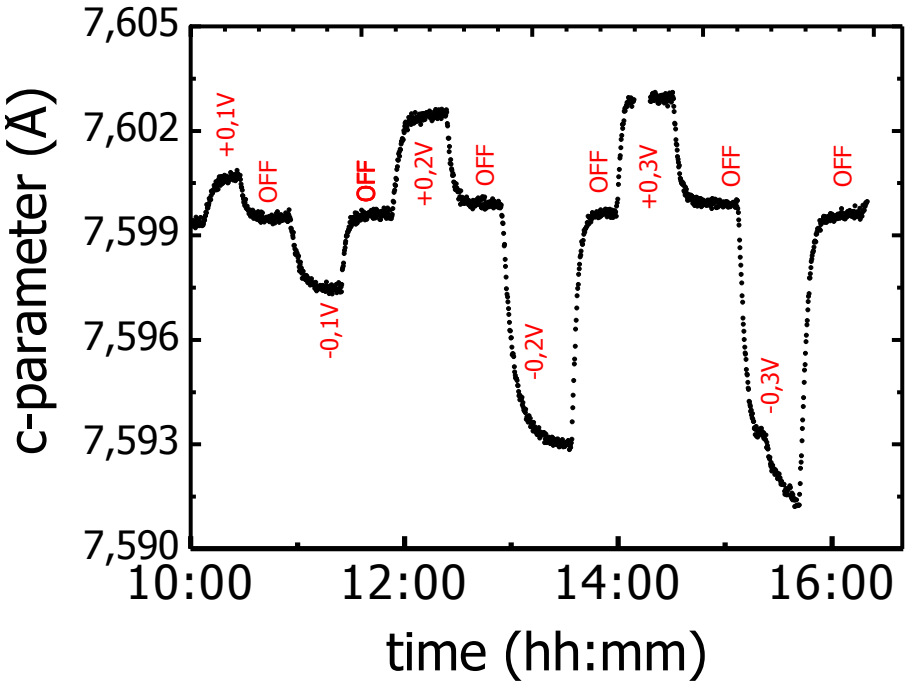

Figure 6.7 Variation of the c-parameter throughout the experiment (as planned in Figure 6.6) monitored by in-situ X-ray diffraction.

6.5 Results and discussion

The variation of the cell parameters as a function of applied electrochemical potential is shown in Figure 6.7. Here after we describe positive bias as anodic potential and negative bias as cathodic potential. As can be observed, the c-parameter of the GBCO film increases exponentially when an anodic potential is applied until it reaches a stationary value. For instance, the c-parameter increases from 7.5992 (base value) to 7.6008 Å when $+0.1\,V$ anodic potential is applied ($\frac{\Delta c}{c_{base}} \times 100$ =0.021% stain in along c-axis). The exponential shape of the c-t

curve means that it obeys a kinetic response with a particular time response. The increase in c-parameter in GBCO is explained by an increase in oxygen stoichiometry (see Figure 6.1a). Therefore, anodic potential increases the oxygen content in GBCO film i.e., anodic potential causes an oxidation reaction. When the potential was switched OFF from +0.1 V to 0 V, the c-parameters decreased exponentially and reached to the base value (from 7.6008 to 7.5992 Å) meaning that oxygen was released from the GBCO film lattice (reduction process). This implies that the process of oxidation-reduction under anodic potential is reversible (similar XRD measurements can be found in the literature[21]). The c-parameter increases to 7.6024 Å with increasing anodic potential from 0 V to +0.2 V. Switching OFF the potential from +0.2 V to 0 V results in the decrease of c-parameter to the base value. c-parameters tend to saturate at +0.3 V where c-parameter increases to 7.6030 Å with +0.014% expansion in the out-of-plane direction. In all the above cases, the redox reactions are fully reversible.

When a cathodic potential was applied from 0 V to -0.1 V, the c-parameter decreased exponentially from 7.5992 (the base value) to a stationary value of 7.5974Å, with -0.023 % contraction in the out-of-plane direction. When the potential was switched OFF, then c-parameter started increasing and recovered the base value. This implies that cathodic potential causes reduction and when the potential is switched OFF, oxidation reaction brings back the base value of c-parameter. When -0.3 V is applied, the c-parameter decreases to 7.5918 Å (-0.102% strain) In this case, oxidation-reductions are fully reversible.

Stabilization of any oxygen content under an electrochemical potential is governed by two electrochemical reactions; i) oxygen exchange at GBCO/air interface and ii) oxide ionic transport across the GBCO/CGO/YSZ/Ag/air heterostructure interface. For example, when an anodic potential is applied, an oxidation reaction happens (Eq 6.2) at the Pt/GBCO interface. Co(III) gets oxidized to Co(IV) and releases 2 electrons. Oxygen vacancies of the GBCO film ($V_{\ddot{O}}$) are transported to the GBCO/air surface to enable reduction and thus incorporate oxygen at the lattice sites. Oxygen ion transport across the GBCO/CGO/YSZ can be described by equation 6.3 where oxygen vacancies are carried by CGO/YSZ heterostructure from the bottom electrode. Oxygen at the lattice (O^x) gets oxidized at the YSZ/Ag interface to complete the circuit. In order to stabilize any particular oxygen stoichiometry under an applied anodic (or cathodic) potential, these two reactions (Eq 6.3 and 6.5) must forma steady state equilibrium.[22]

$$2Co(III)^x \rightarrow 2Co(IV)^{\cdot} + 2e \qquad (6.2)$$

$$\frac{1}{2}O_2(g) + V_{\ddot{O}} + 2e \rightarrow O_O^x \qquad (6.3)$$

$$O^x_{GBCO} + O^{\cdot\cdot}_{CGO} \rightarrow O^{\cdot\cdot}_{GBCO} + O^x_{CGO} \qquad (6.4)$$

$$O^x_O \rightarrow \frac{1}{2}O_2(g) + V^{\cdot\cdot}_O + 2e \qquad (6.5)$$

These equations are expressed in Kröger-Vink notation where an oxygen ion in the YSZ lattice is the ground state so it is considered neutral (with a '*x* 'superscript), while the oxygen vacancy in the YSZ is positively charged (two charges) $V_O^{\cdot\cdot}$ (one dot superscript means one positive charge). In the same way Co(III) ions are considered as the ground state in GBCO and therefore it is considered neutral, while Co(IV) is positively charged. Mention must be made that these equations should fulfill charge neutrality. The explanation of incorporation of oxygen into GBCO from the atmosphere could have been expressed in terms of oxygen interstitials instead of oxygen vacancies (the same could have occurred with holes instead of electrons) but, for simplicity, we have chosen the oxygen vacancies.

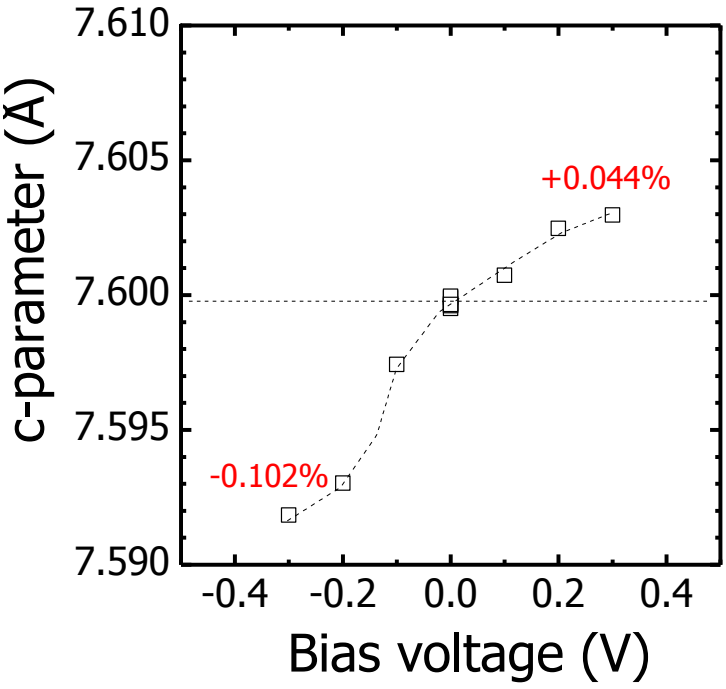

Figure 6.8 Variation of the saturated (or final) c-parameter when cathodic and anodic bias is applied. Strain in c-parameter is highly asymmetric when cathodic and anodic bias is applied.

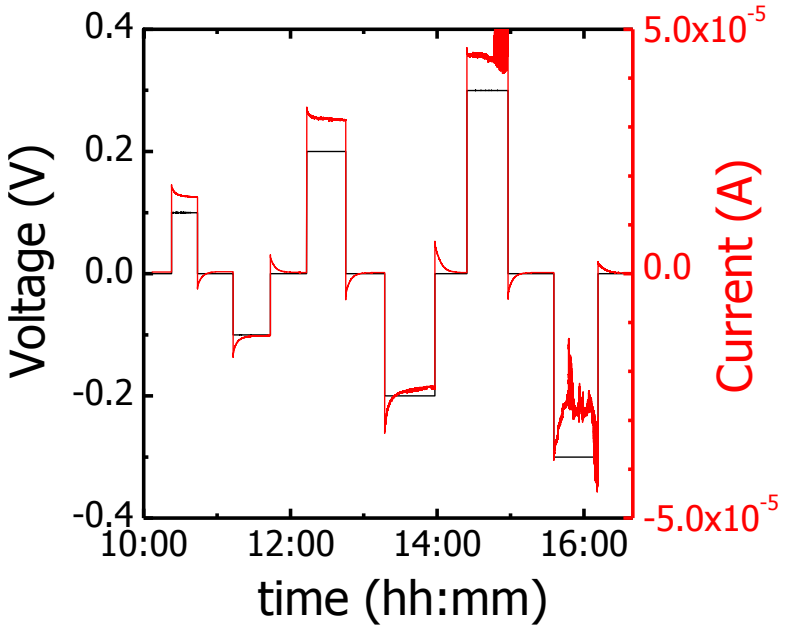

Figure 6.9 Chronoamperometry curves (I-t transients) measured during the oxidation-reduction reactions in presence or absence of cathodic and anodic potential.

The variation of the final c-parameters against applied cathodic and anodic potential is depicted in Figure 6.8. Clearly, the cell parameter increases monotonically with positive bias achieving an expansion of about $\Delta c/c$= +0.044 % at V= +0.3 V. However, for the negative bias, there is a much steeper reduction of the cell parameter reaching $\Delta c/c$= -0.102 % at V= -0.3V, which is more than twice the cell parameter change at a positive bias of the same magnitude.

The asymmetry in the chemical strain could be related to two different possibilities. First, the change in oxygen nonstoichiometry for a given cathodic potential might be larger than the anodic potential (discussed later). Secondly, for a similar oxygen stoichiometry change, the chemical strain in GBCO might not be exactly symmetric as it might correspond to a different mechanism for oxidation and reduction. In order to differentiate these two possibilities, the chronoamperometry result was analyzed in order to understand the oxygen stoichiometry changes.

In chronoamperometric titration in an electrochemical cell, the potential between electrodes is kept constant and I-t curves are measured. In this experiment, I-t transient curves were measured while a certain potential difference was maintained during the in-situ X-ray diffraction measurements, as depicted in Figure 6.9. Current displays transient behaviors during stabilization. Chronoamperometric titration is very similar to potentiostatic coulometric

titration regarding the chemical process (or reactions) taking place in an electrochemical cell. Therefore, one would expect an exponential-like decay in current in I-t curves. When changing from 0 → V (V< ±0.3V), at lower voltages, the current transient shows a clear exponential decay for both positive and negative bias, while at V= ± 0.3 V the current shows fluctuations of a large magnitude that precluded extracting any reliable current value. However, the corresponding transient current values, when switching off the voltage to V=0, show perfect exponential decays in the full voltage range from 0.1 to 0.3 V.

Any process that perturbs the system might affect the shape of the I-t curves.[14] For example, the presence of any capacitive current (which generally decays faster than the redox reaction) or any coupled chemical reactions (or secondary reactions) taking place at the electrochemical cell might affect the shape of the I-t curve. The decay of current with time for cathodic and anodic potentials (both in ON and OFF condition) is presented in Figure 6.10. The current values were normalized according to equation 6.6 and plotted in log scale.

$$I_{Normalized} = \frac{I\,(t) - I_{final}}{I_{initial} - I_{final}} \qquad (6.6)$$

Figure 6.10a shows current decay curves when cathodic and anodic bias was switched on. Clearly, the curve indicates the presence of two different decays meaning that two different chemical reactions are competing with each other. On the other hand, when the potential was switched OFF (shown in Figure 6.10b), the current decay curve shows the presence of only one exponential in every case at least the 1st 1000 sec. This implies that when the potential was switched OFF, the charge relaxation process is governed by only one reaction. For the sake of clarity, a comparison of current decays is plotted in Figure 6.10c when anodic potential was switched ON and OFF (from 0 V to +0.1 V or from +0.1 V to 0 V), respectively.

Interestingly, this observation is consistent with the reaction mechanism previously proposed (equation 6.2 to 6.5) for the stabilization of certain amounts of oxygen stoichiometry by applying electrochemical potential. When potential is switched ON, two reactions occur; one at the GBCO film-air interface and another one are at the GBCO/CGO/YSZ−Ag/air interface (which act as a pump). On the other hand, when the potential is switched OFF, only the reaction at the GBCO film-air interface controls the stoichiometry. Nevertheless, I-t transient curves allow the extraction one more important quantity; the number of transported charge (Q_e) by integrating the area under the curve in chronoamperometry using equation 7.7 as also depicted in Figure 6.11a.

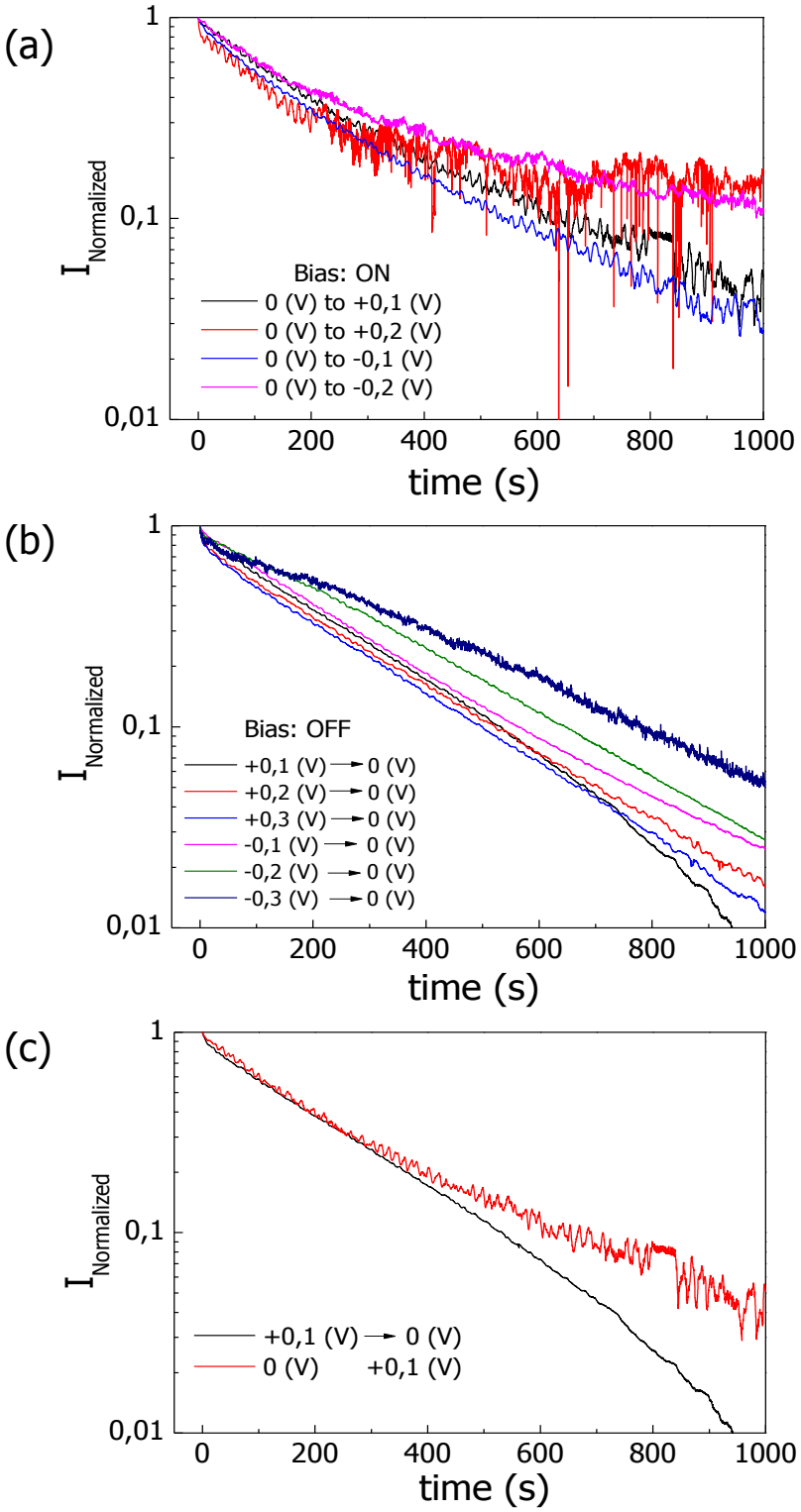

Figure 6.10 Plot of the current decay with time for variable anodic and cathodic potential applied: (a) log plot of the normalized current with time when potential is switched OFF, (b) when potential is switched ON and, (c) when anodic potential (+0.1 V) is switched OFF and ON, respectively.

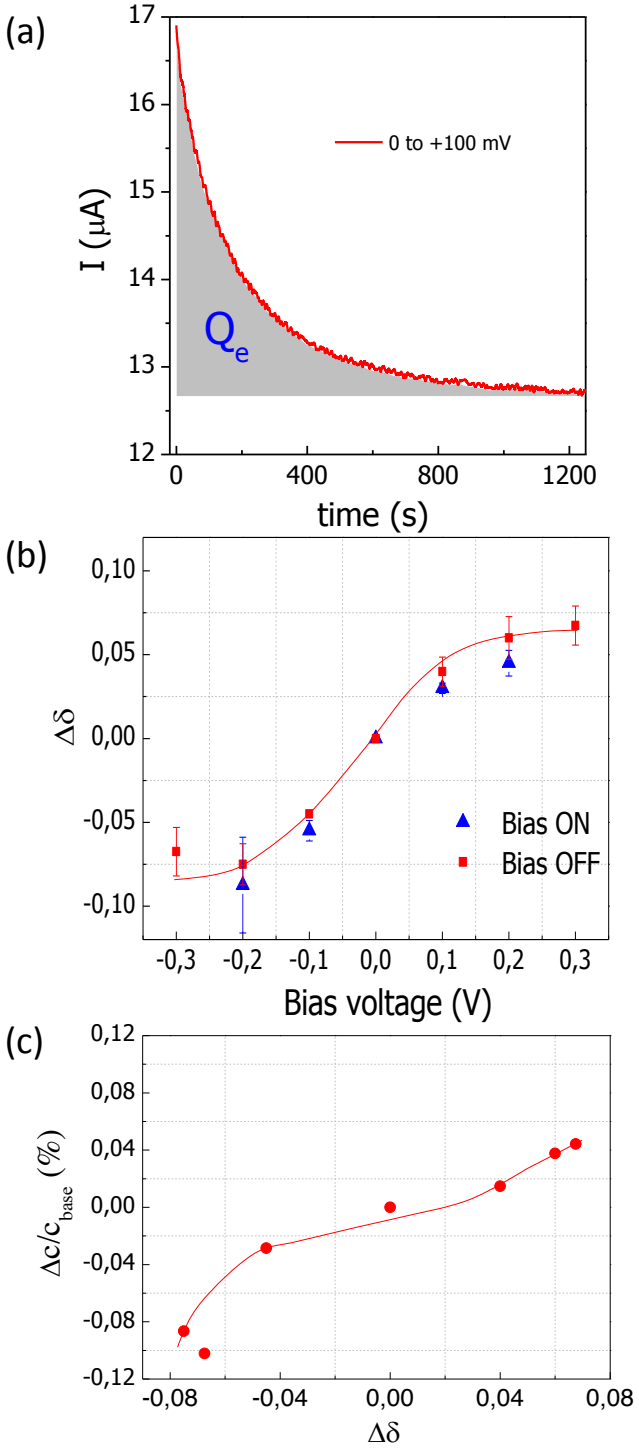

Figure 6.11 Chronoamperometry results: (a) calculated of the number of transported charge (864 μC) by integrating the area under the curve when +0.1 V potential applied, (b) calculation of the estimated oxygen nonstoichiometry from the number of the transported charge using equation 6.9. Error bars were obtained from the uncertainty in the extracting area under the I-t curve and (c) Semi quantitative comparison of the chemical strain relative to the change in oxygen nonstoichiometry (solid and dotted lines in panel_b & c are guide to the eyes).

The number of transported charge (Q_e) was calculated from the area under the I-t curves, as shown by equation 6.7. On the other hand, the change of the unit cell volume of thin film is subtle compared to the number of transported charge. Therefore, the change in oxygen nonstoichiometry ($\Delta\delta$) can be estimated from the equation 6.8 as the number of transported charge (Q_e), the number of electrons involved in the redox reaction ($n = 2$ for O^{-2} ion) and number of the unit cell present in the thin film are known parameters (e represents the charge of electrons).

$$Q_e = \int_{t=0}^{t=\infty} I(t)dt \qquad (6.7)$$

$$\Delta\delta = \frac{Q_e}{n.e}\left(\frac{V_{unit\ cell}}{V_{thin\ film}}\right) \qquad (6.8)$$

Figure 6.11 depicts the estimated relative change in oxygen stoichiometry, $\Delta\delta$. Calculated stoichiometry were different when certain potential were switched ON and OFF, respectively. As the fluctuation in current increased at higher potential, a large error appears in the integrated area (for example, in -0.2 V). Moreover, at ±0.3 V, the number of transported charge was not extracted due to large noise in the current. On the other hand, when potential was switched OFF in each step, the I-t transients were very smooth. Therefore, the integrated areas under the I-t curves are more reliable. Nonstoichiometry was calculated assuming that there was no capacitance at the GBCO-Pt interface. This result indicates that the change in nonstoichiometry was almost symmetric when an equal magnitude of cathodic and anodic potential was applied, as those depicted in Figure 7.11b and c. This is an interesting observation because the observed asymmetry in the chemical strain can now be referred to as the change in the chemical expansion mechanism.

The asymmetry in the chemical strain might be related to the fact that the change in ionic radii of Co ion from Co^{+3} to Co^{+4} is different from Co^{+3} to Co^{+2} transformations. In addition, the layered structure of the $GdBaCo_2O_{5.5}$ presents a particular chemical strain mechanism different to that of standard single perovskite. As reported in Ref 23 (at least in the range $GdBaCo_2O_{5.5+\delta}$, $\delta < 0$) the particular behavior of the c-axis expansion upon increasing the oxygen composition in GBCO can be regarded as a competition between the [GdO_δ] expansion and [BaCoO] compression.[23] The incorporation of oxygen fills in the oxygen vacancy sites in the [GdO_δ] slabs causes its expansion due to Coulomb repulsion. The oxygen sites in the [BaCoO] slabs are fully

occupied, and therefore no oxygen stoichiometry variations are expected in this slab. However, the charge generated by the incorporation of oxygen in the [GdO_δ] slabs should be compensated by transferring two electrons per O coming from the mixed valence Co ions. Therefore, the oxidation state of Co increases which implies a reduction of its ionic radius. This produces a compression of the [BaCoO] layer that opposes to the [GdO_δ] slab expansion although the material still shows an overall expansion. The opposite reasoning can be used for the reduction of the oxygen stoichiometry. The overall c-parameters variation is a balance between the change in both the slabs and it seems to be dominated by the [GdO_δ] expansion making the GBCO behave in opposition to typical oxygen vacancy disordered perovskites where an increase in the oxygen composition increase results in a reduction of the overall cell volume.

6.6 Conclusion

In summary, we have grown highly c-axis oriented GBCO film on a YSZ substrate. A thin buffer layer of CGO was deposited to avoid any secondary phase formation at the interface of GBCO film and YSZ substrate. We can confidently conclude that oxygen stoichiometry of the GBCO thin film can be controlled by applying an anodic or cathodic electrochemical potential. Anodic potential allows the increase of the oxygen stoichiometry inside the film lattice and, thus increases the c-parameter while a cathodic potential allows the removal of the oxygen from the GBCO film lattice. Chemical strain is highly asymmetric due to different compensations between [GdO] and [BaCoO] slab expansions. Current transient across the heterostructure interface allows calculation of the number of transported charge at a given electrochemical potential. The estimated $\Delta\delta$ was significant even when a small (±100 mV) potential was applied. Finally, we can conclude that the electrochemical method allows continuous control of the oxygen stoichiometry in a wide range of values, which may serve as a powerful tool for exploring the physical properties of the oxide materials with mixed valence transition metal ions.

Bibliography:

[1] J. Suntivich, H. A. Gasteiger, N. Yabuuchi, H. Nakanishi, J. B. Goodenough, Y. Shao-Horn, *Nat. Chem.* **2011**, *3*, 546–550.

[2] H. L. Tuller, S. R. Bishop, *Annu. Rev. Mater. Res.* **2011**, *41*, 369–398.

[3] R. Waser, R. Dittmann, C. Staikov, K. Szot, *Adv. Mater.* **2009**, *21*, 2632–2663.

[4] E. Boehm, J. M. Bassat, P. Dordor, F. Mauvy, J. C. Grenier, P. Stevens, *Solid State Ionics* **2005**, *176*, 2717–2725.

[5] S. Inoue, M. Kawai, N. Ichikawa, H. Kageyama, W. Paulus, Y. Shimakawa, *Nat. Chem.* **2010**, *2*, 213–217.

[6] V. L. Kozhevnikov, I. A. Leonidov, M. V. Patrakeev, E. B. Mitberg, K. R. Poeppelmeier, *J. Solid State Chem.* **2001**, *158*, 320–326.

[7] Z. Cai, Y. Kuru, J. W. Han, Y. Chen, B. Yildiz, *J. Am. Chem. Soc.* **2011**, *133*, 17696–704.

[8] A. Maignan, C. Martin, D. Pelloquin, N. Nguyen, B. Raveau, *J. Solid State Chem.* **1999**, *142*, 247–260.

[9] A. A. Taskin, A. N. Lavrov, Y. Ando, *Appl. Phys. Lett.* **2005**, *86*, 1–3.

[10] A. A. Taskin, A. N. Lavrov, Y. Ando, *Phys. Rev. B - Condens. Matter Mater. Phys.* **2005**, *71*, 134414.

[11] A. A. Taskin, A. N. Lavrov, Y. Ando, *Phys. Rev. B* **2006**, *73*, 121101.

[12] H. Jeen, W. S. Choi, M. D. Biegalski, C. M. Folkman, I. C. Tung, D. D. Fong, J. W. Freeland, D. Shin, H. Ohta, M. F. Chisholm, et al., *Nat. Mater.* **2013**, *12*, 1057–1063.

[13] H. Jeen, W. S. Choi, J. W. Freeland, H. Ohta, C. U. Jung, H. N. Lee, *Adv. Mater.* **2013**, *25*, 3651–3656.

[14] Q. Lu, B. Yildiz, *Nano Lett.* **2016**, *16*, 1186–1193.

[15] A. A. Taskin, A. N. Lavrov, Y. Ando, *Phys. Rev. B - Condens. Matter Mater. Phys.* **2005**, *71*, 1–28.

[16] M. Li, W. Han, X. Jiang, J. Jeong, M. Samant, S. S. P. Parkin, *Nano Lett.* **2013**, *13*, 4675.

[17] A. L. Krick, S. J. May, *APL Mater.* **2017**, *5*, 42504.

[18] D. Passarello, S. G. Altendorf, J. Jeong, M. G. Samant, S. S. P. Parkin, *Nano Lett.* **2016**, *16*, 5475–5481.

[19] T. Kawada, J. Suzuki, M. Sase, A. Kaimai, K. Yashiro, Y. Nigara, J. Mizusaki, K. Kawamura, H. Yugami, *J. Electrochem. Soc.* **2002**, *149*, E252.

[20] D. Chen, H. L. Tuller, *Adv. Funct. Mater.* **2014**, *24*, 7638–7644.

[21] R. Moreno, P. Garc, J. Zapata, J. Roqueta, J. Chaigneau, J. Santiso, *Chem. Mater.* **2013**, *25*, 3640-3647.

[22] M. D. Biegalski, E. Crumlin, A. Belianinov, E. Mutoro, Y. Shao-Horn, S. V. Kalinin, *Appl. Phys. Lett.* **2014**, *104*, 161910.

[23] N. Ishizawa, T. Asaka, T. Kudo, K. Fukuda, A. Yasuhara, N. Abe, T. Arima, *Chem. Mater.* **2014**, *26*, 6503–6517.

Chapter: 7 Conclusions and perspectives

7.1 Conclusion

The work presented in this thesis was devoted to the growth of misfit cobaltates $[Bi_2Sr_2O_{4-\delta}]^{RS}[CoO_2]$ thin films (BSCO) and, mixed ion and electronic conducting $GdBaCo_2O_{5.5\pm\delta}$ (GBCO) thin films via the PLD technique followed by structural characterization using X-ray diffraction and transmission electron microscopy techniques. Thermopower measurements were carried out in order to understand the conduction mechanisms and the focus was to understand thermopower variations in high temperature region (high temperature limit ~ 300 K) where the magnitude of Seebeck coefficient is expected to achieve a constant value presumably determined by the statistical site availability. The high crystal quality of the deposited thin films achieved by controlling crystal orientation, oxygen stoichiometry and epitaxial strain allowed exploration of the fundamental properties of these materials without the influence of possible material anisotropy; grain boundaries. The epitaxial films are close to single crystals, which in many occasions are very challenging to grow in a large size to be able to measure them. The main conclusions of this research work can be summarized as follows:

- Oxidation-reduction processes of BSCO films by chemical stimuli are fully reversible. Therefore, different amount of oxygen stoichiometry can be stabilized in BSCO films via annealing the films in variable oxygen atmospheric pressure.
- GBCO thin films grown on different substrates accommodate oxygen vacancies in order to sustain the epitaxial strain induced by the substrates as evident from the thermopower measurements.
- All solid-state electrochemical approach allows the control of the oxygen stoichiometry of GBCO thin films reversibly at moderately high temperature (~350 K). This method overcomes the difficulties of sudden change of the atmospheric pressure (from 10^{-5} to 1 atm) in order to control the oxygen stoichiometry of the perovskite oxide and related thin films.
- Contrary to the established models on most transition metal oxides involving spin-orbit degeneracy, thermopower of misfit cobaltate thin films in the incoherent transport region can be understood solely in terms of Heike's formula without recourse to the spin-orbit degeneracy factor. This implies that the indirect determination of the spin states of cobalt ions is unreliable unless an independent measurement is carried out to determine the spin-states. More importantly, the search for new materials based on the concept of spin-orbit degeneracy is still questionable.

- The true high temperature limit of thermopower in GBCO thin films is in the metallic phase at around 350 K. Therefore, thermopower is governed by statistical distribution of charged carriers over available sites, which dominates the conduction even in the metallic phase.
- The analysis of thermopower of GBCO films at 350 K allows the extraction of information about polaron formation of variable sizes.
- The positive thermopower of all electron and hole doped GBCO thin films at 300 K are the signature of the incoherent motion of the charge carriers. This observation also indicates the formation of the large polarons.
- The sign of the thermopower in strongly interacting localized charge carriers at high temperature limit is determined by the ratio of filled to vacant sites. Therefore, any crossover of the sign of thermopower as a function of doping concentration or temperature in Heike's limit cannot be directly assigned to the change of the sign of the charge carrier.

7.2 Perspectives

The crystal quality of the deposited films allowed exploration of the more fundamental aspects of the thermopower which are not yet fully understood. However, there are many open questions which need to be addressed and from the work performed in this thesis, it could be fruitful to pursue the following studies:

Thermal conductivity measurements of BSCO and GBCO thin films

Although the low thermal conductivity of LSAT substrates allows the maintenance of a large temperature gradient during Seebeck measurement, thermal conductivity measurements by 3-omega method presents difficulties as the thermal conductivity of GBCO and LSAT is within the same order of magnitude. Nevertheless, it would be interesting to investigate the thermal transport properties of misfit cobaltate films and double perovskite cobaltate films.

Research in last two decades was focused to understand the electronic and magnetic transport properties of misfit cobaltates. Thermal transport properties were not studied in detail. It will be interesting to study the in-plane and cross-plane thermal transport properties of misfit cobaltate thin films by introducing defects in the films and interface between films and substrates.

From the detailed study of the microstructures of GBCO films under defferent amount of in-plane bi-axial compressive and tensile strains, we saw that the films under tensile strain are fully epitaxial and highly c-axis oriented, where as films under compressive strain formed mixed oriened domains of nanometer size without the presence of grain boundaries among them. This kind of nanostructures were observer in PbTe-SrTe system,[1] which exhibited a significant effect in the thermoelectric transport properties by selectively scattering the phonons without affecting the electronic transport Fully strained nanostructured precipitates in bulk matrix did not show the presence of grain boundaries. Such kind of nanostructures are called endotaxial nanostrucrures. Therefore, it will be interesting to study the thermal transport properties of thin GBCO films under compressive and tensile strains.

Nernst effect measurements

It would be interesting to determine the dominant scattering mechanisms in BSCO and GBCO films. The Nernst effect is very sensitive to the charge carrier scattering processes and research in this direction could provide clues as to whether the thermopwer of GBCO is associated with the Nernst coefficient[2] or not.

In the case of BSCO films and other misfit cobaltates, study of Nernst effect will be important within the temperature below 50 K, where the supression of the Seebeck coefficient were observed by applying a magnetic field. Interestingly, the Hall effect shows unusual behaviour within that temperature range,[3] which might be related to the scattering processes.[4]

Solid state electrochemical devices

A solid state electrochemical method has been proven to be a powerful approach in the control of oxygen stoichiometry in oxide thin films and therefore, the control of physical properties. However, this technique works at elevated temperature making use of a YSZ solid electrolyte. It would therefore be interesting to use this technique in experiments at room temperature. Recently, several experiments have been performed using ionic liquid[5] and ionic gels[6] and we consider that it would be worth exploring this possibility in case of GBCO films.

Bibliography

[1] K. Biswas, J. He, Q. Zhang, G. Wang, C. Uher, V. P. Dravid, M. G. Kanatzidis, *Nat. Chem.* **2011**, *3*, 160–166.

[2] P. Sun, F. Steglich, *Phys. Rev. Lett.* **2013**, *110*, 216408.

[3] H. W. Eng, P. Limelette, W. Prellier, C. Simon, R. Frésard, *Phys. Rev. B* **2006**, *73*, 33403.

[4] T. Yamamoto, I. Tsukada, M. Takagi, T. Tsubone, K. Uchinokura, *J. Magn. Magn. Mater.* **2001**, *230*, 2031–2032.

[5] D. Passarello, S. G. Altendorf, J. Jeong, M. G. Samant, S. S. P. Parkin, *Nano Lett.* **2016**, *16*, 5475–5481.

[6] A. L. Krick, S. J. May, *APL Mater.* **2017**, *5*, 42504.

Appendix A: High temperature thermoelectric properties of misfit cobaltate $Ca_3Co_4O_{9\pm\delta}$ ceramics

A.1 Introduction

$Ca_3Co_4O_9$ (CCO) is one of the promising p-type thermoelectric oxides, which shows a figure of merit more than unity at 1000 K.[1] CCO crystal has a monoclinic misfit layered structure of space group C2/m (Z=6).[2],[3],[4] The structure can be represented as $[Ca_2CoO_3]^{RS}[CoO_2]^{Hex}$. An electrically conducting hexagonal CoO_2 layer is incommensurately sandwiched between two electrically insulating rock salt type layers along the crystallographic c-axis as depicted in Figure A.1.

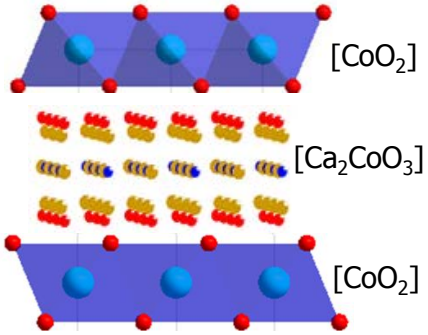

Figure A.1 Crystal structure of misfit $Ca_3Co_4O_9$. Rock salt type layer is sandwiched between CoO_2 layers.

High thermoelectric figure of merit at 1000 K is basically due to two different reasons. First, unique misfit layered crystal structures results in low thermal conductivity.[5] Secondly, the Seebeck coefficient and electrical conductivity are decoupled at high temperature; both quantities increase with increasing temperature.[6] In addition, CCO shows many interesting features at low, room and high temperatures. Experimental and theoretical research has mostly been focused on the low temperature thermoelectric, magnetic properties. For example, an unconventional Hall effect below 20 K,[7] scaling behavior of the magneto resistance,[8] magneto thermopower,[9] charge transfer[10] from localized band to itinerant band by ARPES spectroscopy[11] have been observed in $Ca_3Co_4O_9$ single crystals. An understanding of the theoretical and experimental results provides a general idea about the entropy contribution to thermopower at room temperature. Thermopower saturates before reaching room temperature and it is almost temperature independent from 150 K to 300 K.[12], [13] Thus, room temperature thermopower is considered to be dominated by the statistical distribution of the charge carrier over the available crystal sites given by Heike's formula:[14]

$$S = -\frac{\kappa_B}{e}\ln\left(\frac{x}{1-x}\right) \qquad (1.18)$$

Although the Heike's limit of thermopower has been observed at room temperature, relatively higher temperature measurements reveal that the thermopower increases further with increasing temperature from 380 to 750K.[6] So, the high temperature limit of the thermopower has not been well defined for this compound. Moreover, a decoupling of the resistivity and thermopower is apparent above 380 K. While the calculation of thermopower from electronic band structure by Boltzmann transport theory provides a temperature dependent thermopower the calculated and measured thermopower matches very well when the electrons are itinerant (for example Na_xCoO_2)[15] i.e. when the band width (W) is higher than thermal activation ($\kappa_B T$).

In this appendix, we present the high temperature thermoelectric properties of $Ca_3Co_4O_9$ polycrystalline ceramics. The original idea was to grow highly oriented or epitaxial thin films but this has not yet been achieved. Therefore, the analysis of ceramic polycrystalline pellets has been attempted.

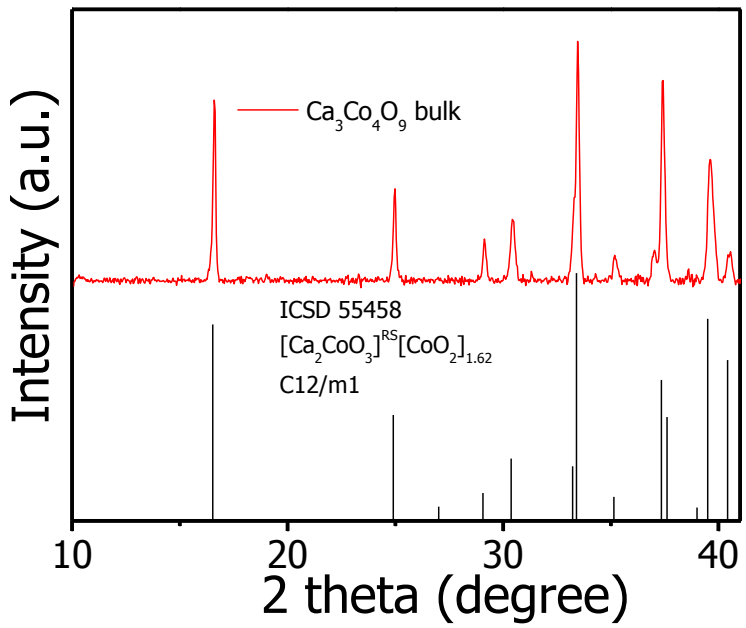

Figure A.2 Powder X-ray diffraction patterns of $Ca_3Co_4O_9$ polycrystalline ceramics.

A.2 Synthesis and characterization

$Ca_3Co_4O_9$ polycrystalline pellets were synthesized by conventional high temperature solid state diffusion reactions. A stoichiometric mixture of Co_3O_4, $CaCO_3$ was mixed in an agate mortar to obtain homogeneous powder. The powder was pressed using a stainless steel die in a pellet under 25 metric ton uniaxial pressure. The heating profile of the synthesis contained two steps. First, calcination followed by sintering in a high O_2 atmosphere. The pellet was slowly heated to 860 °C and calcined for 40 hours at the same temperature and then slowly cooled to

room temperature. The calcined pellet was ground into fine powder and then pressed into a pellet at 30 metric ton uniaxial pressure for 30 minutes to achieve high density. The pellet was then placed in a tubular furnace and sintered it at 900 °C for 20 hours in a 100 sccm flow of oxygen.

X-ray diffraction patterns of $Ca_3Co_4O_9$ polycrystalline pellet are shown in Figure A.2. The atomic reflections can be indexed by comparing the diffraction pattern of $[Ca_2CoO_3]^{RS}[CoO_2]_q$ (C12/m1 space group), where reflections from the rock salt type layer are dominant.

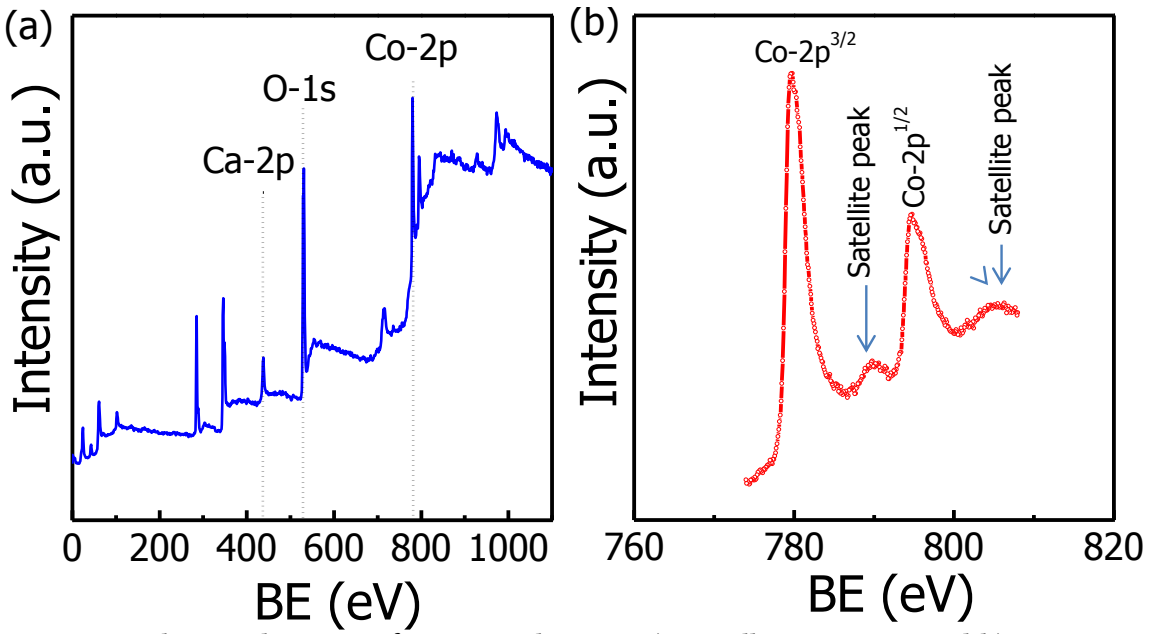

Figure A.3 Element detection of $Ca_3Co_4O_9$ by XPS; a) overall XPS spectra and b) Co-2p XPS spectra of $Ca_3Co_4O_9$ polycrystals. Presence of satellite peaks indicates the presence of mixed valence pair of cobalt ions.

The presence of calcium and cobalt was detected by XPS. The high resolution core level spectrum in Figure A.3, of Co-2p shows a sharp line shape which is ascribed in the literature to the presence of Co^{+3} ions with low spin. Due to spin-orbit coupling, Co-2p spectrum splits into two different peaks, Co-$2p^{3/2}$ (779.51 eV) and Co-$2p^{1/2}$ (794.69) with an intensity ratio of 2:1. Due to the ligand to metal charge transfer, satellite peaks were observed at relatively higher binding energy than the main intense peak s. In general, the appearance of satellite peaks indicates the present of high spin states of Co^{+2} ions. Interestingly, satellite peaks have also been observed for misfit cobaltate $Bi_2Sr_2Co_2O_y$ where Co^{+3}/Co^{+4} mixed valence is present.[16] Thus, it could either be a Co^{+2}/Co^{+3} pair or a Co^{+3}/Co^{+4} pair in case of our polycrystalline samples. In misfit cobaltates, the oxidation state of cobalt ion in CoO_2 layer is expected to be $Co^{3+\delta}$ where Co^{+4} ions are dominant

carriers. However the crystal structure of CCO differs from other misfit cobaltates such as $Bi_2Sr_2Co_2O_y$. The composition of the rock salt type layer in CCO misfit is Ca_2CoO_3 where the valence of the cobalt is +3, [17] or slightly less than 3 i.e. $Ca_2CoO_{3-\delta}$.[10] So the valence of cobalt in the unit cell can be written as follows.

$$[Ca_2Co_{1-x}^{+III}Co_x^{+II}O_3]_q^{RS}[Co_{1-y}^{+III}Co_y^{+IV}O_2]^{Hex}$$

Polycrystalline CCO samples were annealed in different controlled pO_2 atmospheres. The annealing was done for two different reasons. First, to test the stability of the thermoelectric property at high temperature and the second reason was to stabilize different oxygen stoichiometries, which in turn act in the self-doping of the CoO_2 layer.

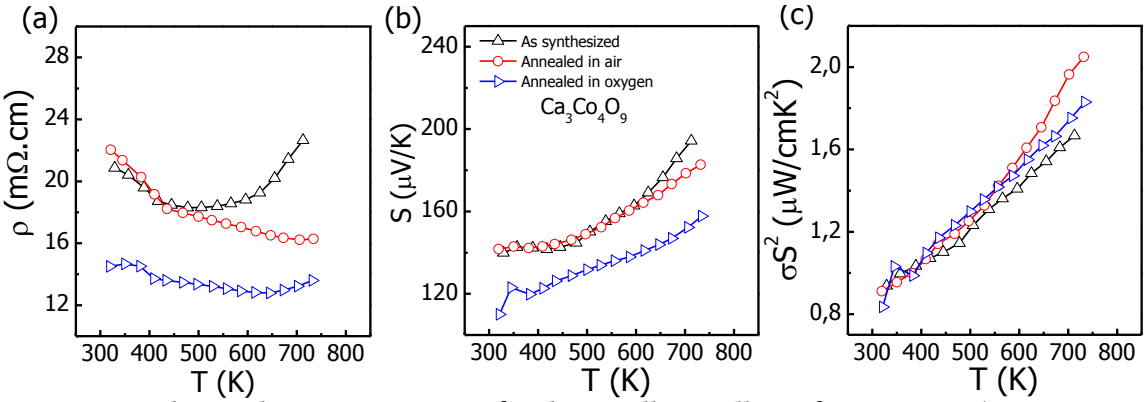

Figure A.4 Thermoelectric properties of polycrystalline pellets of $Ca_3Co_4O_9$; a) temperature dependent electrical resistivity, b) thermopower and c) power factor of as synthesized, oxygen annealed and air annealed samples.

A.3 Thermoelectric properties

Simultaneous measurements of the electrical resistivity and Seebeck coefficient were performed by a standard 4-probe method using a LINSEIS instrument under helium atmosphere from 300 K to 775 K. The polycrystalline pellets were cut into a rectangular bar dimensions 1 cm ×2.5mm×2mm suitable for measurements with the LINSEIS instruments. The thermoelectric properties of annealed and as-synthesized CCO polycrystalline pellets were highly reproducible and stable from 300 K to 775 K, as depicted in Figure A.4. The measured Seebeck coefficient, electrical resistivity and power factors of our samples were consistent with the reports in the literature for polycrystals. Resistivity and thermopower of air annealed (at 800 °C for 20 hours) and as synthesized samples at 350 K were similar to each other while the oxygen annealed (at 800 °C, 1 atm pO_2 for 20 hours) samples differed. The oxygen annealed samples had lower resistivity and thermopower compared to as-synthesized samples at 350 K. This could be

because of the increased Co^{+4}/Co^{+3} ratio due to stabilization of the oxygen stoichiometry in the lattice.

The S value at 340 K of as-synthesized was 140 μV/K and it increased with increasing temperature and acquired a value of ~185 μV/K at 775 K. Temperature dependent ρ and S did not follow a similar trend. At high temperatures, ρ and S decoupled (see Figure A.5b). This indicates that ρ and S followed different conduction mechanisms. The decoupling nature of ρ and S has also been observed in $Bi_2Sr_2Co_2O_y$ thin film at 300 K.[18]

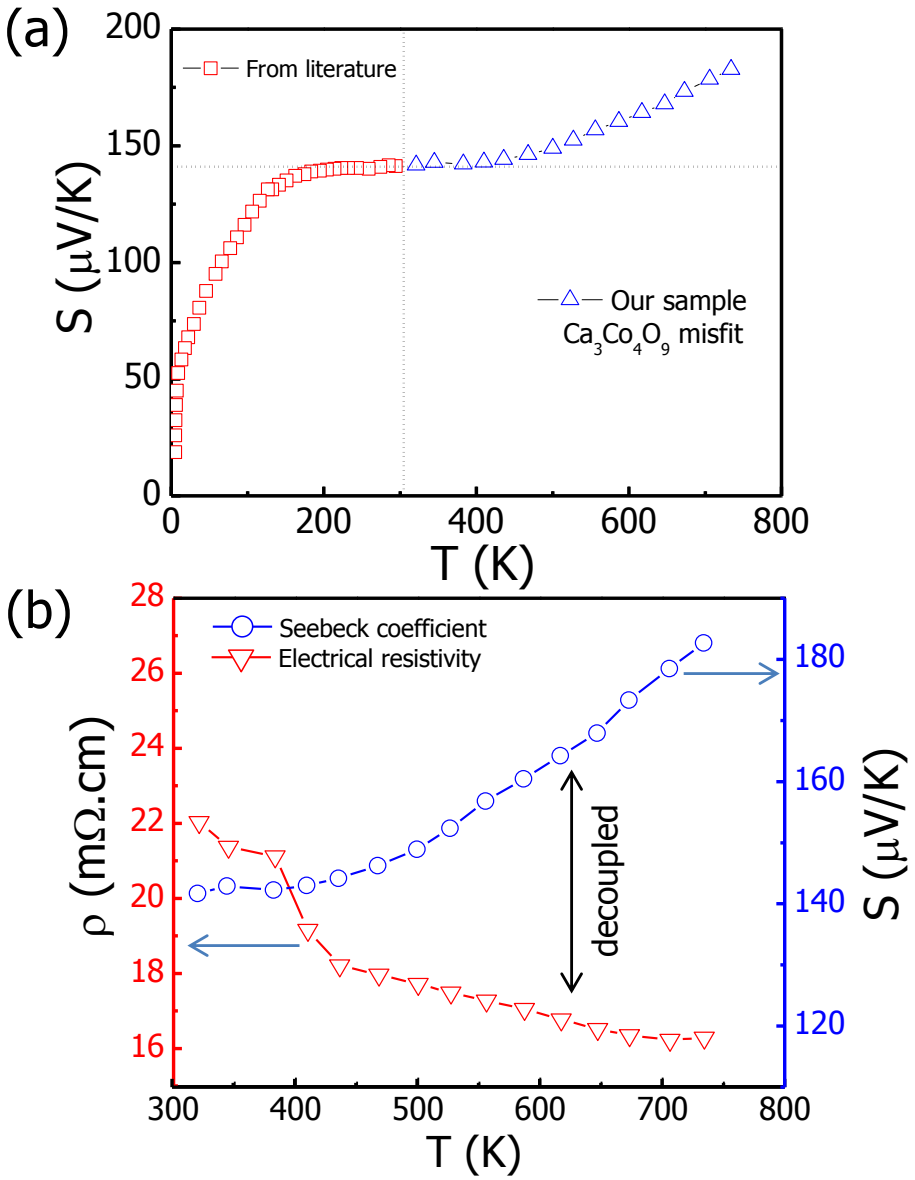

Figure A.5 Temperature dependent electrical resistivity and thermopower (adding data from reference)[19] of air annealed $Ca_3Co_4O_9$ is plotted together to highlight the decoupling and enhancement of Seebeck coefficient.

A.4 An important question to answer

Detailed studies of the ceramic samples of $Ca_3Co_4O_9$ polycrystalline pellets have already been performed by other authors with two interesting observations as follows:

- In general, the high temperature limit of thermopower of misfit cobaltates is at around 300 K where *S* is temperature independent. But, the high temperature study reveals that, *S* further increases with increasing temperature (shown in Figure A.5a). However, this increase of *S* is not due to the change in electrical resistance; rather, electrical resistivity drops at high temperatures (Figure A.5b). So, the question remains; why does *S* increase with increasing temperature from 380 K to a higher temperature?

Interestingly,

i. An unresolved structural phase transition has been detected where a sudden drop of a, b_1 and b_2 parameters was observed at ~400 K. Resistivity and specific heat showed a hysteresis behaviour with a magnetic field, which indicates the presence of magnetic ordering,[3], [11]

ii. Several magnetic phase transitions have been reported in $Ca_3Co_4O_9$ systems at different temperatures. At 400 K,[2], [20], [21] a spin state transition was said to occur from low spin (LS) to intermediate spin (IS). Another magnetic phase transition was reported at 500 K, [22] from paramagnetic LS to paramagnetic high spin (HS) state.

Therefore, the structural and magnetic transitions might influence the transport properties.

- The 2nd question to be addressed is 'how does the spin-state transition affect thermopower?'

In our case, the high temperature limit of thermopower is close to 300 K, which is highlighted in Figure A.5a. According to equation A.1, the only parameter which influences the thermopower is *x* which is defined as follows:

$$x = \frac{conc.\,of\ electrons\ per\ unit\ cell}{available\ crystal\ sites} = \frac{[n]}{N_v} \qquad (A.2)$$

The change in resistivity from 380 K to 700 K is subtle compared to the change of *S* within the same temperature range. The decrease in resistivity might be due to the increase in carrier density [n] or due to the increase in mobility. For simplicity, we assume that [n] does not change at higher temperatures. Therefore, an estimation of *x* can be done from the measured Seebeck

coefficient by using equation A.1. As the Seebeck coefficient increases with increasing temperature from 380 K to a certain value at 700 K, the estimated value of x is expected to decrease to a certain value within the same temperature range. Figure A.6 depicts the variation of x as thermopower varies.

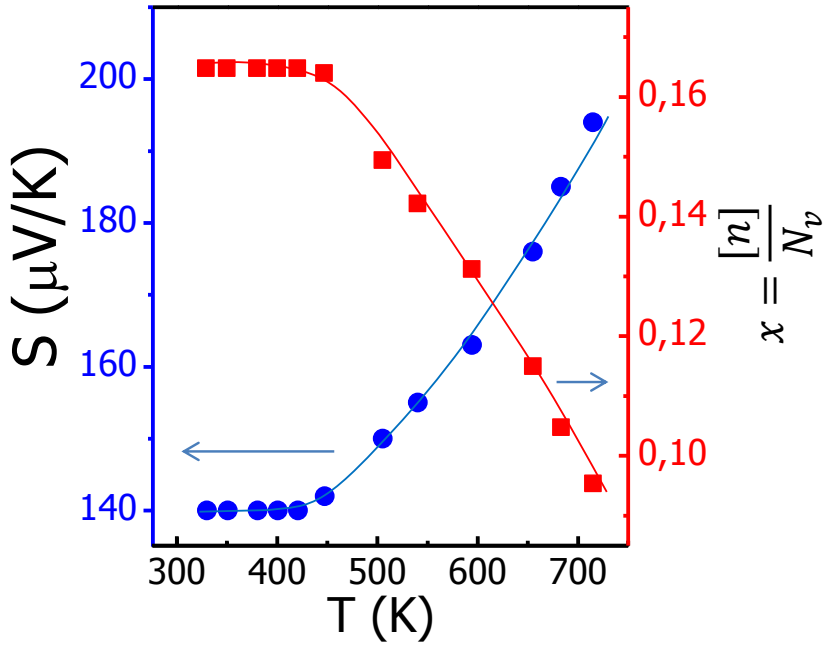

Figure A.6 The x is calculated from the measured S at different temperature by using equation A.1. The bold lines are the guide to the eyes.

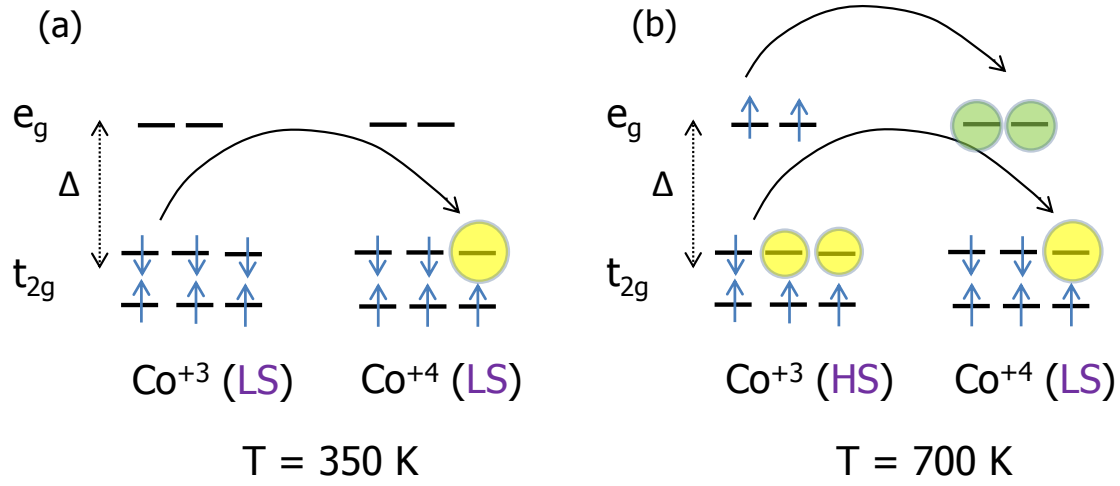

Figure A.7 Schematic illustration of the electronic structure of Co^{+3} and Co^{+4} ions in an octahedral coordination. (a) LS states of Co^{+3} and Co^{+4} ions at 350 K for CCO polycrystals and, (b) HS states of Co^{+3} and LS state of Co^{+4} ions at 700 K. α is the spin down and β is the spin up states. Spin up states have higher energy and different symmetry than spin down electrons.

As shown in Figure A.6, *x* decreases with increasing temperature. Interestingly, if the carrier density, [n], does not change with increasing temperature then, the available sites (N_v) must increase with increasing temperature. It will be interesting to compare the electronic structure of cobalt ions in CCO before and after the spin-state transition as depicted in FigureA.7 (a simple LS to HS state transition of Co^{+3} ions is considered in this case).

The available sites in the α-energy states in t_{2g} orbitals are highlighted by yellow filled circles while those in the e_g orbitals are highlighted by light green filled circles. The number of available states at 350 K is only one, while after spin state transition of Co^{+3} ions, the available sites become 5. It is noteworthy that the hopping of electrons among different energy states takes place, thereby maintaining symmetries, energy level and spin alignment. Therefore, electrons in e_g orbitals cannot hop in the t_{2g} levels (due to energy difference) and spin down electrons cannot hop in the spin up electronic states. Apparently, if the charge carrier density does not change with increasing temperature, the spin-state transition might increase the available sites. Therefore, variation of the available sites is physically possible due to spin state transition. At the same time, the drop in resistivity with increasing temperature can be explained in terms of an increase of the hopping probability, or in other words, of the charge carriers.

A.5 Summary

The above descriptions provide information about the distribution of charge carriers over available sizes due to spin state transition. In other words, it describes the variation of the size of polarons with increasing temperature. However, this is a hypothesis that the size of polarons influences the thermopower, which needs to be proven experimentally.

Bibliography

[1] M. Shikano, R. Funahashi, *Appl. Phys. Lett.* **2003**, *82*, 1851–1853.

[2] A. C. Masset, C. Michel, A. Maignan, M. Hervieu, O. Toulemonde, F. Studer, B. Raveau, J. Hejtmanek, *Phys. Rev. B* **2000**, *62*, 166–175.

[3] T. Wu, T. A. Tyson, H. Chen, J. Bai, H. Wang, C. Jaye, *J. Phys. Condens. Matter* **2012**, *24*, 455602.

[4] S. Lambert, H. Leligny, D. Grebille, *J. Solid State Chem.* **2001**, *160*, 322–331.

[5] A. Satake, H. Tanaka, T. Ohkawa, T. Fujii, I. Terasaki, A. Satake, H. Tanaka, T. Ohkawa, *J. Appl. Phys.* **2004**, *96*, 931.

[6] N. Van Nong, N. Pryds, S. Linderoth, M. Ohtaki, *Adv. Mater.* **2011**, *23*, 2484–2490.

[7] H. W. Eng, P. Limelette, W. Prellier, C. Simon, R. Frésard, *Phys. Rev. B* **2006**, *73*, 33403.

[8] and D. G. P. Limelette, J. C. Soret, H. Muguerra, *Phys. Rev. B* **2008**, *77*, 245123.

[9] P. Limelette, S. Hébert, H. Muguerra, R. Frésard, C. Simon, *Phys. Rev. B* **2008**, *77*, 235118.

[10] G. Yang, Q. Ramasse, R. F. Klie, *Phys. Rev. B* **2008**, *78*, 153109.

[11] and T. K. Wakisaka, Y, S. Hirata, T. Mizokawa, Y. Suzuki, Y. Miyazaki, *Phys. Rev. B* **2008**, *78*, 235107.

[12] J. Soret, M. B. Lepetit, *Phys. Rev. B - Condens. Matter Mater. Phys.* **2012**, *85*, 165145.

[13] W. Koshibae, K. Tsutsui, S. Maekawa, *Phys. Rev. B* **2000**, *62*, 6869–6872.

[14] P. M. Chaikin and G.Beni, *Phys. Rev. B* **1976**, *13*, 647.

[15] S. Kuno, T. Takeuchi, H. Ikuta, T. Kondo, A. Kaminski, Y. Saito, S. Fujimori, S. Radiation, E. Agency, *IEEE Int. Conf. Thermoelectr.* **2007**, *2*, 99.

[16] S. S. and T. Takeuchi, Tsunehiro, Takeshi Kondo, Tsuyoshi Takami, Hirofumi Takahashi, Hiroshi Ikuta, Uichiro Mizutani, Kazuo Soda, Ryoji Funahashi, Masahiro Shikano, Masashi Mikami, Syunsuke Tsuda, Takayoshi Yokoya, *Phys. Rev. B* **2004**, *69*, 125410.

[17] M. Schrade, H. Fjeld, T. G. Finstad, T. Norby, *J. Phys. Chem. C* **2014**, *118*, 2908–2918.

[18] J. Ravichandran, A. K. Yadav, W. Siemons, M. A. McGuire, V. Wu, A. Vailionis, A. Majumdar, R. Ramesh, *Phys. Rev. B - Condens. Matter Mater. Phys.* **2012**, *85*, 85112.

[19] Y. Wang, Y. Sui, J. Cheng, X. Wang, W. Su, *J. Phys. D. Appl. Phys.* **2008**, *41*, 45406.

[20] Y. Miyazaki, K. Kudo, M. Akoshima, Y. Ono, Y. Koike, T. Kajitani, *Jpn. J. Appl. Phys.* **2000**, *39*, L531–L533.

[21] J. Sugiyama, J. H. Brewer, E. J. Ansaldo, H. Itahara, K. Dohmae, Y. Seno, C. Xia, T. Tani, *Phys. Rev. B* **2003**, *68*, 134423.

[22] P. Limelette, V. Hardy, D. Jérome, D. Flahaut, S. Hébert, R. Frésard, C. Simon, *Phys. Rev. B* **2005**, *71*, 233108.

Appendix B: Fermi function and thermopower

The Fermi function can be defined mathematically as

$$f = \frac{1}{\exp\left(\frac{E-\mu}{\kappa_B T}\right)+1} = f(\mu, E, T) \qquad (B.2)$$

The current flow in a conductor under the influence of electric field $(V_1 - V_2)$ and temperature difference $(T_1 - T_2)$ can be written as,

$$I = \sigma(V_1 - V_2) + \sigma_S(T_1 - T_2) \qquad (B.2)$$

The current flow due to the difference in chemical potential and temperature difference can also be expressed from the difference in the Fermi function as follows:

$$I \sim \frac{1}{e}\int_{-\infty}^{+\infty}[f(\mu_1, T_1, E) - f(\mu_2, T_2, E)]dE \qquad (B.3)$$

The difference in Fermi energy can be written as the function of the derivative of the Fermi function (f) with respect to energy (E) as follows:

$$[f(\mu_1, T_1, E) - f(\mu_2, T_2, E)]$$

$$= \left(\frac{df}{d\mu}\right)[\mu_1 - \mu_2] + \left(\frac{df}{dT}\right)[T_1 - T_2]$$

$$= \left(-\frac{df}{dE}\right) \times \left(\Delta\mu + \frac{E-\mu_e}{T}\Delta T\right) \qquad (B.4)$$

As thermoelectric voltage is a temperature driven open circuit voltage, therefore, the current flow in the circuit is zero i.e., $I = 0$. Therefore, from equation B.2, we get,

$$0 = \sigma(V_1 - V_2) + \sigma_S(T_1 - T_2)$$

$$0 = \sigma\Delta V + \sigma_S\Delta T$$

For measurement of open circuit voltage, it will be convenient to write in terms of voltage,

$$\Delta V = -\frac{\sigma_S}{\sigma}\Delta T = S\Delta T \qquad (B.5)$$

So, the Seebeck coefficient (S) can be expressed as shown in the following equation:

$$S = -\frac{\sigma_S}{\sigma} \sim -\frac{1}{eT}\frac{\int_{-\infty}^{+\infty}[M]\left(-\frac{df}{dE}\right)[E-\mu_e]dE}{\int_{-\infty}^{+\infty}[M]\left(-\frac{df}{dE}\right)dE} \qquad (B.6)$$

where [M] contains microscopic information such as energy dependent density of states, energy dependent relation time and group velocity etc.

The actual expression of the Seebeck coefficient is presented as,

$$S_{diffusion} = \frac{\int_{-\infty}^{+\infty} N(E)v_x^2(E)\tau(E)\left(\frac{E-\mu}{\kappa_B T}\right)\left[-\frac{\partial f}{\partial E}\right]dE}{\int_{-\infty}^{+\infty} N(E)v_x^2(E)\tau(E)\left[-\frac{\partial f}{\partial E}\right]dE} \qquad (B.7)$$

or

$$S = \frac{1}{eT}\frac{\int_{-\infty}^{+\infty}\sigma(E)\left(-\frac{df}{dE}\right)[E-\mu_e]dE}{\int_{-\infty}^{+\infty}\sigma(E)\left(-\frac{df}{dE}\right)dE} \qquad (B.8)$$

Therefore, from equation B.6, B.7 and B.8, the Seebeck coefficient can be defined as the average conductance near Fermi energy.